

**ELECTRON-ELECTRON INTERACTIONS IN
COMPLEX-OXIDE NANODEVICES**

by

Michelle Tomczyk

B.S., University of Dayton, 2011

M.S., University of Pittsburgh, 2013

Submitted to the Graduate Faculty of
the Kenneth P. Dietrich School of Arts and Sciences in partial
fulfillment

of the requirements for the degree of

Doctor of Philosophy

University of Pittsburgh

2017

UNIVERSITY OF PITTSBURGH
DIETRICH SCHOOL OF ARTS AND SCIENCES

This dissertation was presented

by

Michelle Tomczyk

It was defended on

July 12th 2017

and approved by

Jeremy Levy, Dept. of Physics and Astronomy

David Pekker, Dept. of Physics and Astronomy

Brian D'Urso, Dept. of Physics and Astronomy

James Mueller, Dept. of Physics and Astronomy

David Waldeck, Dept. of Chemistry

Dissertation Director: Jeremy Levy, Dept. of Physics and Astronomy

ABSTRACT

ELECTRON-ELECTRON INTERACTIONS IN COMPLEX-OXIDE NANODEVICES

Michelle Tomczyk, PhD

University of Pittsburgh, 2017

Strontium titanate (SrTiO_3) is a superconducting semiconductor [1] possessing characteristics which suggest an unconventional pairing mechanism [2, 3]; however, direct experimental insight into the nature of electron pairing in SrTiO_3 has remained elusive. SrTiO_3 -based interfaces can provide new clues about electronic interactions leading to pairing. In particular, the electronic system at the interface of LaAlO_3 and SrTiO_3 hosts a broad array of emergent phenomena, including superconductivity [4], spin-orbit coupling [5, 6], and magnetism [7], providing a tantalizing platform to study electronic interactions.

In this dissertation, nanodevices with well-characterized quantum behavior are used as probes of the interfacial electronic system. These devices enable coherent single-electron and single-subband resolution of electronic states, which can elucidate the microscopic details of electronic interactions. Tunneling behavior through nanowire quantum dots reveals the existence of electron pairs far outside the superconducting regime [8]. While this suggests strong attractive interactions, Andreev transport at higher gate voltages indicates a gate-tunable sign change of electron-electron interactions [9]. Ballistic transport over micrometer distances produces quantum interference oscillations in nanowire cavities [10], and also leads to quantized conductance plateaus in electron waveguide devices [11]. Evolution of the plateaus in an applied magnetic field reveals details of the strength and variation of the electron pairing, and other related physical properties. These results provide guidance to theoretical predictions of the microscopic origins of the electron pairing interactions.

TABLE OF CONTENTS

PREFACE	xii
1.0 INTRODUCTION	1
1.1 Strontium Titanate	3
1.1.1 Ferroelastic Transition	3
1.1.2 Incipient Ferroelectric Transition	4
1.1.3 A Superconducting Semiconductor	4
1.2 Emergent Properties at the LaAlO ₃ /SrTiO ₃ Interface	6
1.2.1 Metal-Insulator Transition	6
1.2.2 Electronic Structure at the LaAlO ₃ /SrTiO ₃ Interface	8
1.2.3 Superconductivity	8
1.2.4 Rashba Spin-Orbit Coupling	9
1.2.5 Magnetism	9
1.3 Nanostructures and Dimensionality	10
2.0 EXPERIMENTAL METHODS	13
2.1 LaAlO ₃ /SrTiO ₃ Sample Preparation	13
2.1.1 Sample Growth	13
2.1.2 Canvas Fabrication	15
2.2 c-AFM Lithography	16
2.2.1 AFM Operation	18
2.2.2 c-AFM Lithography	19
2.2.3 Water-Cycle Mechanism	20
2.3 Low-Temperature Transport	23

2.3.1	Physical Property Measurement System Operation	23
2.3.2	Superconducting Magnet Operation	23
2.3.3	Dilution Refrigerator Operation	25
2.3.4	Software: LabVIEW	25
2.3.5	Hardware	27
2.3.5.1	Peripheral Component Interconnect Extension (PXI)	27
2.3.5.2	Pickering	29
3.0	ELECTRON PAIRING WITHOUT SUPERCONDUCTIVITY	30
3.1	Introduction	30
3.2	Device geometry and fabrication	31
3.2.1	Barrier Fabrication	31
3.2.2	Impact of Barrier Height on Transport	35
3.3	Experiments and Results	35
3.3.1	Transport at B=0 T	35
3.3.2	Transport at Finite Magnetic Field	36
3.3.2.1	Universal Shift with Magnetic Field	39
3.3.2.2	Analysis of B_p	39
3.3.3	Temperature Dependence	42
3.4	Discussion	42
3.4.1	Pair Tunneling and Resonant Superconductivity	42
3.4.1.1	Device Transport Parameters	44
3.4.1.2	Constant Interaction Model	45
3.4.2	Attractive Hubbard Model	46
3.4.3	Pairing Mechanisms	52
3.4.4	Alternative Explanations	52
3.5	Conclusion	54
4.0	TUNABLE ELECTRON-ELECTRON INTERACTIONS IN $\text{LaAlO}_3/\text{SrTiO}_3$ NANOSTRUCTURES	57
4.1	Introduction	57
4.2	Device Geometry and Fabrication	58

4.3 Experiments and Results	60
4.4 Discussion	63
4.4.1 Theoretical Model of Transport in the SSET	63
4.4.1.1 Weak Coupling Regime	64
4.4.1.2 Intermediate Coupling Regime	67
4.4.1.3 Spectral Functions	68
4.4.1.4 Numerical Calculation of the DOS	72
4.4.1.5 Strong Coupling Regime and RCSJ Model	74
4.4.2 Mechanisms for Density-Tuned Interactions	74
4.4.3 Signatures of Pre-Formed Pairs	77
4.5 Conclusions	77
5.0 MICROMETER-SCALE BALLISTIC TRANSPORT OF ELECTRON	
PAIRS	80
5.1 Introduction	80
5.1.1 Summary	80
5.1.2 Clean One-Dimensional Transport	81
5.2 Device Geometry and Fabrication	82
5.3 Experiments and Results	84
5.3.1 Equilibrium (zero-bias) Transport	84
5.3.1.1 Background Subtraction	85
5.3.1.2 Superconducting Phase and Modulation of Critical Current	85
5.3.2 Transconductance	87
5.3.2.1 Universal shift	89
5.3.3 Non-Equilibrium Transport	90
5.4 Discussion	92
5.4.1 Modeling of Fabry-Perot Interference	92
5.4.1.1 Coupling Factor	96
5.4.2 Finite-Bias Transport	97
5.4.3 Single-Barrier Devices	97
5.4.4 Transport through the Open Wire	98

5.5 Conclusion	98
6.0 QUANTIZED BALLISTIC TRANSPORT OF ELECTRONS AND ELECTRON PAIRS IN AN ELECTRON WAVEGUIDE	101
6.1 Introduction	101
6.2 Device Geometry and Fabrication	102
6.3 Experiments and Results	106
6.3.1 Finite Bias Spectroscopy	108
6.3.1.1 Lever Arm	109
6.3.1.2 g-Factor	111
6.4 Discussion	111
6.4.1 Non-Interacting Waveguide Model	111
6.4.2 Tight-Binding Hamiltonian for Electron Waveguide	113
6.4.3 Electron Pairs at Low Magnetic Fields	115
6.4.4 Re-Entrant Pairing	115
6.4.5 Avoided Crossings	119
6.4.6 Single vs Double Barriers	121
6.4.7 Comparison with Quantum Hall Effect	124
6.5 Conclusion	124
7.0 FUTURE DIRECTIONS AND CONCLUSIONS	127
7.1 Future Directions	127
7.1.1 Pascal-Liquid Phase in an Electron Waveguide	127
7.1.2 Frictional Drag as a Probe of Electronic Interactions	129
7.2 Conclusion	129
BIBLIOGRAPHY	131

LIST OF TABLES

1	Parameters of eight SSET devices.	45
2	Re-entrant pairing fitting parameters for device A and B.	120
3	Avoided crossing fitting parameters for device A and B.	122

LIST OF FIGURES

1	SrTiO ₃ crystal structure.	5
2	Emergent physics at the LaAlO ₃ /SrTiO ₃ interface.	7
3	LaAlO ₃ growth on SrTiO ₃ substrate.	14
4	LaAlO ₃ /SrTiO ₃ canvases.	15
5	Photolithography procedure.	17
6	AFM operation.	18
7	c-AFM procedure.	21
8	Water-cycle mechanism for c-AFM lithography.	22
9	PPMS schematic.	24
10	DR components.	26
11	DAQ setup.	28
12	Device schematic and transport characteristics.	32
13	Nanoscale potential barrier engineering.	33
14	Transport properties of different barrier heights.	34
15	Transport characteristics of device A.	37
16	Out-of-plane magnetic field dependence of device A.	38
17	Global shift correction of device A data.	40
18	Waterfall plot of Fig. 16(f).	41
19	Temperature dependence of B_p	43
20	Parity effect.	50
21	Phase diagram of the Hubbard model on a one-dimensional 16-site chain.	51
22	Comparison between experiment and attractive Hubbard model.	53

23	Transport characteristics of devices B, C, D and E.	55
24	Superconducting single electron transistor (SSET).	59
25	Transport characteristics of an SSET.	61
26	Simulation of pair conductance diamonds on varying gapped excitations in the leads.	65
27	Theoretical calculation of DOS spectra.	69
28	Comparison between data and calculation.	70
29	RCSJ model fitting.	75
30	Low-field dependence of ABS.	78
31	Device schematic and Fabry-Perot oscillations.	83
32	Differential conductance.	85
33	Background subtraction.	86
34	Critical Current Modulations.	87
35	Magnetic field dependence of conductance oscillations.	88
36	Non-repeatable global shift.	90
37	Global shift correction.	91
38	Fabry-Perot interference signatures at finite bias.	93
39	Semi-classical transmission model.	95
40	Single barrier device.	99
41	Waveguide writing schematic.	103
42	Expected transport characteristics of electron waveguides.	105
43	Transport of devices A and B at $T = 50$ mK, and comparison with theory. . .	107
44	Quantization of the $1 e^2/h$ plateau.	109
45	Finite bias analysis.	110
46	Non-interacting waveguide model.	114
47	Strongly paired electron waveguides.	116
48	Electron-electron interaction in device A.	117
49	Phase diagram of the Hartree-Bogoliubov model.	120
50	Single barrier vs double barriers.	123

51	Critical magnetic field for splitting the lowest two spin subbands for additional devices.	125
52	Pascal liquid phases in an electron waveguide.	128
53	Frictional drag device setup.	129

PREFACE

This dissertation represents the culmination of my Ph.D. journey, and would not have been possible without the guidance and support of many important people.

First, I'd like to thank my research advisor, Jeremy Levy, for the motivation and mentorship over the past 6 years. His mentorship is quite multifaceted: he exhibits a deep understanding and passion for research; he provides an excellent example of always engaging with the data and is constantly coming up with new experiments to try; he emphasizes the importance of communication, and gives public speaking advice and opportunities, as well as networking advice and opportunities; he is always looking ahead to implementing new ways to make such a large lab with such diverse projects operate smoothly and efficiently. Thank you for a wonderful and very educational graduate research experience!

Next, I need to thank Dr. Guanglei Cheng, for his invaluable assistance. When I first started in lab, he trained me on using the dilution refrigerator, the labview programs, how to perform experiments pretty much everything in the day-to-day lab operation. We certainly made a great team!

I'd also like to thank my labmates for the all the good times, the shared frustrations, the ups and downs of scientific research. In particular, Patrick Irvin, Joshua Veazey, Mengchen Huang, Megan Briggeman, Arthur Li, Yuhe Tang, Yun-Yi Pai, Lucy Chen, and Qing Guo, as well as the new batch of students, who are fantastic, and I'm excited to see what they accomplish in their own graduate research.

My own experiments couldn't have been done without samples- I'd like to thank Prof. Chang-Beom Eom's research group for providing us with great ones! Additionally, I want to express my gratitude to my dissertation committee members, David Pekker, Brian D'Urso, Jim Mueller, and David Waldeck. Their guidance and feedback have helped immensely.

Finally, I'd like to thank my family and friends for their love and support. My parents, Elaine and Mike Tomczyk, have always encouraged my love of math, science, and mystery-solving, from instilling in me a love of reading and learning to helping me build an electric motor for a 4-H summer project back in junior high. They've held a constant belief in me during my undergrad and graduate study. My significant other, Tom DeCarlo, has celebrated my achievements, provided encouragement during the frustrating times, and helped me stay grounded with shed-building and swing-dancing. I look forward to continuing this journey knowing that he's got my back. I'd also like to thank my siblings and Tom's parents for letting me know how much they believe in me!

1.0 INTRODUCTION

Understanding how electrons interact and the impact of their interactions is an overarching objective in solid state physics. Fermi liquid theory successfully describes the behavior of many electronic systems by redefining electrons, with their inherent Coulomb interactions, as weakly-interacting quasiparticles. However, Fermi liquid theory breaks down when electron correlations become more significant, for example in one-dimensional systems. While Fermi liquid theory explains why much of the basis of solid state physics is well-described by non-interacting models, many active research areas such as high-temperature superconductivity, Majorana quasiparticle statistics, and fractional quantum Hall effect now focus on phenomena that can only be explained by understanding the underlying electron-electron interactions.

In particular, superconductivity is a well-known phenomenon, first observed in 1911 when a sample of mercury was cooled with liquid helium, and the resistance suddenly vanished below 4.2 K. In the past century, significant advances in both experiment and theory have led to numerous Nobel prizes, as well as current and future applications in medicine, transportation, energy and quantum computation.

At the heart of superconductivity in electronic systems are attractive electron-electron interactions. The conventional Bardeen-Cooper-Schrieffer (BCS) microscopic description of electronic superconductivity [12] requires only a very weak attraction to bind electrons into pairs. The weakness of the attraction, combined with the high carrier density (of order $10^{22}cm^{-3}$), means that the average pair size is much larger than the inter-electron distance. The electrons bind into pairs and the pairs condense into a coherent superconducting state simultaneously.

By tuning the strength of the electron-electron interaction, a crossover occurs, with the pair size decreasing as the attraction increases. On the far side of this crossover sits the Bose-Einstein condensate (BEC), where electrons form tightly-bound pairs relative to the inter-electron distance. While most low-temperature superconductors are well described by conventional BCS theory, the electron pairing mechanism leading to superconductivity in high-temperature superconductors is highly debated. Understanding the pairing mechanism in unconventional classes of superconductors is therefore very important in developing a room-temperature superconductor for the realization of many future applications. About 50 years ago, there was theoretical speculation about the possibility of electron pairs on the unconventional BEC side of the crossover existing outside of the superconducting state, in low-carrier-density superconductors. In particular, this was predicted for doped bulk strontium titanate (SrTiO_3) [13]. At higher temperatures, electrons were postulated to form tightly bound pairs; below the BEC transition temperature, superconductivity could emerge. The unconventionally low carrier densities at which SrTiO_3 superconducts, along with the similarities to high-temperature superconductors, which weren't discovered until 1986, suggest that understanding electron-electron interactions in SrTiO_3 can provide insight into the pair formation mechanism for high-temperature superconductors.

In this dissertation, the hallmark of BEC-regime physics— electron pairing without superconductivity— is observed and studied at a conductive SrTiO_3 -based interface, consisting of a thin film of lanthanum aluminate (LaAlO_3) on bulk single-crystal SrTiO_3 [8, 9, 10, 11]. Specifically, it is found that electron pairs persist up to pairing temperatures of $T_P \sim 1 - 10$ K and magnetic fields of $B_p \sim 1 - 10$ T, far higher than the superconducting critical temperature $T_c \sim 0.3$ K and upper critical magnetic field $\mu_0 H_{c2} \sim 0.2$ T. The ratio of pairing temperature to Fermi temperature $T_P/T_F \sim 0.1 - 0.8$ is much larger than that of conventional BCS (Bardeen-Cooper-Schrieffer) superconductors [12], indicating that the pairing interactions in low density SrTiO_3 are indeed quite strong and attractive, and hence are in the BEC-BCS crossover regime. As carrier density is increased, a transition to repulsive interactions is observed, providing insight into the potential role of the Ti-orbitals on electron pairing. Finally, transport of electron pairs reveals their surprisingly ballistic nature, in contrast to localized pairs believed to exist at the superconductor-insulator transition.

Various reduced-dimension quantum devices are integral to observing and studying this fascinating new electronic phase. By combining the rich physics at the $\text{LaAlO}_3/\text{SrTiO}_3$ interface with the well-developed paradigm of semiconductor nanoelectronics, both fields benefit: correlated materials provide new functionalities to existing nanodevices, while nanodevices made out of interesting materials can probe the electronic behavior of the material with single-electron and single-subband resolution, revealing details about the underlying electron states. In this work, quasiparticle tunneling spectroscopy through superconducting single-electron transistors (SETs) reveals the existence of pair-tunneling over a much larger phase space than expected in a typical semiconducting or conventional superconducting SET; additionally, the evolution of the tunneling behavior suggests that the sign of the electron-electron interactions is gate-tunable. Quantum interference in a nanowire cavity device implies long coherence and elastic scattering lengths; these are confirmed by quantized ballistic transport through electron waveguides.

The next sections in Chapter 1 describe in more detail the current state of knowledge of the physics at the $\text{LaAlO}_3/\text{SrTiO}_3$ interface. Chapter 2 describes the methods used to grow and prepare the samples and perform the experiments presented in the rest of the thesis. Chapters 3 through 6 present my main research projects: tunneling experiments through superconducting single electron transistors, revealing electron pairing without superconductivity (Ch. 3) and tunable electron-electron interactions (Ch. 4); quantum interference in electron Fabry-Perot cavities (Ch. 5); and quantized ballistic transport in electron waveguides (Ch. 6). The final chapter (Ch. 7) discusses future experimental directions and conclusions.

1.1 STRONTIUM TITANATE

1.1.1 Ferroelastic Transition

Strontium titanate (SrTiO_3) is a complex oxide with a perovskite crystal structure, which is cubic at room temperature with a lattice constant of $a_{\text{STO}} = 3.905\text{\AA}$ (Fig. 1(a)). Like

many perovskites, SrTiO₃ undergoes symmetry-reducing structural transitions as a function of temperature. In particular, at 105 K SrTiO₃ undergoes an anti-ferrodistortive transition in which the oxygen octahedra rotate in opposite directions, causing two of the lattice vectors to contract, while the third lengthens along the axis of the rotations. This results in a tetragonal unit cell, with triply-degenerate domains along X, Y or Z, creating ferroelastic domain boundaries (Fig. 1(b)) throughout the bulk SrTiO₃. While much of the early work on the LaAlO₃/SrTiO₃ interface neglects considering any influence from these domain walls, recent work has highlighted their importance in both normal state [14, 15] and superconducting [16] transport at the interface. Further details of the LaAlO₃/SrTiO₃ interface will be discussed in § 1.2.

1.1.2 Incipient Ferroelectric Transition

At even lower temperatures $T < 38$ K [18], SrTiO₃ begins to approach a second transition to a ferroelectric state [19] (Fig. 1(c)). While it never actually reaches this transition due to quantum fluctuations, the incipient ferroelectric behavior results in an enormous static dielectric constant $\epsilon \approx 20,000$ at low temperature, which stabilizes in the quantum paraelectric regime $T < 4$ K [19]. The large dielectric constant makes SrTiO₃ a common choice of substrate for samples requiring effective backgating; it also results in unusually large gate capacitance for single-electron transistors, as discussed in Chapter 3.

1.1.3 A Superconducting Semiconductor

While bulk SrTiO₃ is a band insulator with a band gap of 3.2 eV, electrons can be introduced via doping (for example, Nb or La), oxygen vacancies [20], or electrolytic gating [21]. Doping bulk SrTiO₃ to carrier densities as low as 10^{17} cm⁻³ results in a superconductor with a small Fermi surface (Fermi temperature $T_F \sim 13$ K) [20], low superconducting critical temperature ($T_c \approx 0.3$ K) [20], and low upper critical field $B_c \approx 0.2$ T [1]. The superconducting properties of SrTiO₃ have been previously investigated by electrical transport [1], tunneling spectroscopy [22], and the Nernst effect [20]. The superconducting critical temperature is non-monotonic as a function of carrier density, leading to a dome-shaped phase diagram in

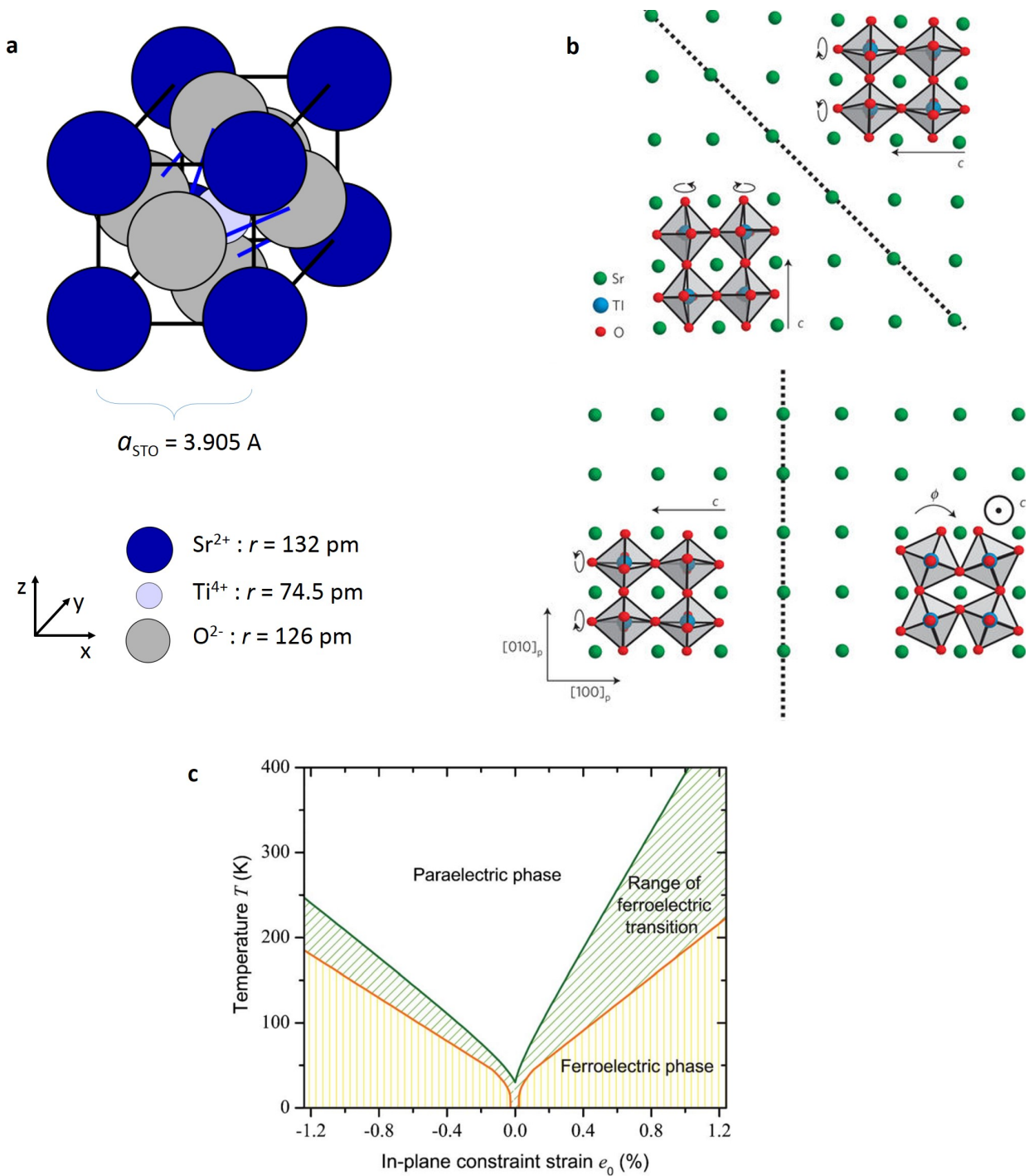


Figure 1: SrTiO_3 crystal structure. **a**, The perovskite structure of SrTiO_3 is cubic at room temperature. **b**, Below 105 K, a structural transition to a tetragonal state leads to the formation of structural domain walls. From ref. [14]. **c**, As-grown SrTiO_3 approaches a ferroelectric phase transition below 37 K, but only reaches a ferroelectric phase when strained. From ref. [17].

which T_c is suppressed at high carrier density; on the other side of the dome, the superconducting state extends to carrier densities much lower than expected for a conventional superconductor with weak, phonon-mediated electron interactions. In a 1969 paper, Eagles argued that the superconductivity in low-density Zr-doped SrTiO₃ involves Bose-Einstein Condensation (BEC) of strongly paired electrons [13], in contrast to conventional Bardeen-Cooper-Schrieffer (BCS) superconductivity in which electron pairing is weak and electron pair size is much larger than the inter-electron spacing [12]. A direct consequence of the strong pairing theory is that above T_c the electrons no longer condense into a superconducting state, but remain in bound pairs. The general phenomenology of transitioning from strong to weak pairing interactions, known as the BEC-BCS crossover, has been thoroughly investigated both theoretically and experimentally in ultracold atoms [13, 23, 24]. However, for 50 years after the prediction of strong pairing in SrTiO₃, the BEC-BCS crossover remained unrealized in solid state systems.

1.2 EMERGENT PROPERTIES AT THE LaAlO₃/SrTiO₃ INTERFACE

New insights into the properties of electronic interactions in SrTiO₃ come from heterointerfaces [25] that enable transport in reduced dimensions. Lanthanum aluminate (LaAlO₃) is closely lattice-matched to SrTiO₃ with a cubic lattice constant $a_{LAO} = 3.789 \text{ \AA}$, permitting clean, epitaxial heterostructure growth. The interface between TiO₂-terminated (001)SrTiO₃ and a thin layer of LaAlO₃ supports a conducting system [25] that exhibits a variety of gate-tunable behavior, derived from the parent SrTiO₃ substrate. This conducting system can be considered a two-dimensional electron liquid, as compared to an electron gas, due to the importance of electron-electron interactions.

1.2.1 Metal-Insulator Transition

A metal-insulator transition occurs at the interface of LaAlO₃ and SrTiO₃ as a function of the LaAlO₃ thickness. When LaAlO₃ is grown at a thickness of three or fewer unit cells

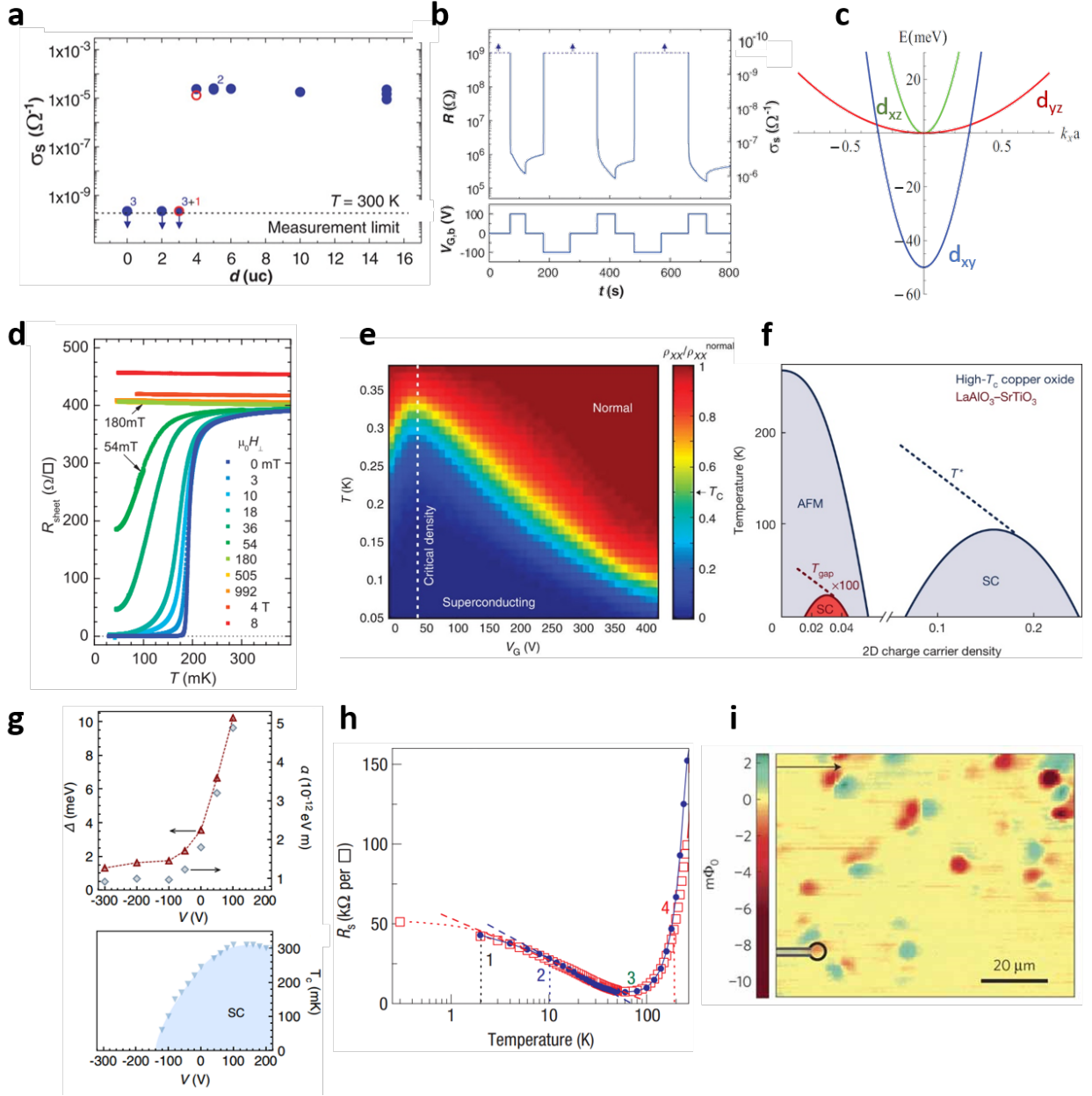


Figure 2: Emergent physics at the $\text{LaAlO}_3/\text{SrTiO}_3$ interface. **a**, Thickness-dependence of the metal-insulator transition. **b**, Electrostatic gating of the metal-insulator transition. (a and b from ref. [26]). **c**, Simplified $3d t_{2g}$ orbital structure at the interface. From ref. [27]. **d**, Superconducting transition. From ref. [4]. **e**, Superconductivity peaks at the Lifshitz transition. From ref. [28]. **f**, Phase diagram similar to high- T_c superconductors. From ref. [3]. **g**, Electrostatic gating of spin-orbit coupling. From ref. [6]. **h**, Kondo minimum. From ref. [7]. **i**, Ferromagnetic domains imaged by SQUID. From ref. [29].

on bulk, TiO_2 -terminated (001) SrTiO_3 , the interface is insulating. At a thickness of four or more unit cells, as shown in Fig. 2(a), a two-dimensional conducting system forms at the interface and extends into the SrTiO_3 [25]. While this critical-thickness dependence of the interface metal-insulator transition was originally observed for (001)-oriented SrTiO_3 , (111) and (110)-oriented SrTiO_3 substrates have also exhibited conducting interfaces with LaAlO_3 above critical thicknesses of 9 and 7 unit cells, respectively [30].

When LaAlO_3 is grown just below the critical thickness, the interface is insulating but can be hysteretically and reversibly tuned through the metal-insulator transition [26]. A positive voltage applied to the backgate induces the metal-insulator transition, and the interface becomes conducting; when the voltage is removed, the interface remains conducting. When a negative voltage is subsequently applied to the backgate, the insulating state is restored at the interface, as shown in Fig. 2(b). This cycle can be repeated multiple times with no degradation of the electronic system [26].

This work studies (001)-oriented SrTiO_3 with sub-critical thickness LaAlO_3 (3.4 unit cells), so that the interface is insulating but highly tunable.

1.2.2 Electronic Structure at the $\text{LaAlO}_3/\text{SrTiO}_3$ Interface

The relevant orbitals contributing to electronic behavior at the $\text{LaAlO}_3/\text{SrTiO}_3$ interface are the $3d t_{2g}$ orbitals derived from the Ti-ions near the interface [31]. Due to confinement in the z -direction at the interface, the d_{xz} and d_{yz} orbitals are raised in energy compared to the d_{xy} orbital [32, 33] (Fig. 2(c)). The Fermi level determines which orbitals participate in transport, and the point where the Fermi level crosses the bottom of the $d_{xz,yz}$ orbitals is called the “Lifshitz transition”. This transition is expected to significantly impact electronic properties [28]. Additional confinement in nanowires at the interface can further split these orbitals into subbands.

1.2.3 Superconductivity

Superconductivity at the $\text{LaAlO}_3/\text{SrTiO}_3$ interface (Fig. 2(d)) behaves like the superconducting phase in the parent SrTiO_3 : it shares a similar critical temperature $T_c \approx 200$ mK [4]

and a phase diagram like that of high-temperature superconductors [3]. The superconducting transition is tunable with electrostatic gating [2], and in particular, T_c peaks at the Lifshitz transition (see Fig. 2(e)), suggesting a close relationship between the relevant orbitals and the pairing mechanism [28]. Additionally, a pseudogap phase observed in tunneling spectroscopy [3] hints at the existence of pre-formed electron pairs outside the superconducting regime (Fig. 2(f)).

1.2.4 Rashba Spin-Orbit Coupling

Atomic spin-orbit interaction, combined with inversion-symmetry breaking, like that at a surface or interface, can lead to a Rashba-type spin-orbit coupling with a momentum-dependent spin splitting [34]. This was observed in magnetotransport measurements at the LaAlO₃ interface [6, 5]. Similar to the superconducting transition temperature, the magnitudes of the Rashba spin splitting and coupling constant can be gated electrostatically [5], exhibiting a very small Rashba effect at low gate voltages, and a sharp increase that coincides with the onset of superconductivity as the gate voltage increases (see Fig. 2(g)) [6].

1.2.5 Magnetism

The observation of magnetic signatures at the LaAlO₃/SrTiO₃ interface is surprising, not only due to the non-magnetic nature of the parent compounds, but also because ferromagnetism is inimical to any spin-singlet superconductivity. The first signature of magnetism was a hysteresis loop in magnetotransport and Kondo-like temperature-dependence (Fig. 2(h)), reported in 2007 [7]. Since then, other transport signatures such as an anomalous Hall effect [35] have been observed, as well as real-space imaging of ferromagnetic patches like in Fig. 2(i), with various techniques such as scanning SQUID magnetometry [29], magnetic force microscopy [36, 37], and x-ray magnetic circular dichroism [38, 39].

1.3 NANOSTRUCTURES AND DIMENSIONALITY

Dimensionality has a profound effect on electron transport. When electrons are confined in two dimensions (2D), new behaviors such as the integer [40] and fractional [41] quantum Hall effect emerge. Electrons confined in one dimension (1D) lose nearly all of their recognizable features [42, 43]. For example, the electron spin and charge can separate and move independently of one another [44], and the charge itself can fractionalize [45].

When discussing dimensionality, it is useful to define a few relevant length scales. Three common length scales related to scattering effects include the elastic scattering length, also known as the mean free path (l_e or l_{mfp}), the inelastic scattering length l_{in} , and the phase coherence length l_ϕ . The mean free path is the distance electrons travel ballistically between elastic scattering events. When the length of a device is much shorter than l_{mfp} , the device can be considered ballistic; that is, most electrons travel through the device without scattering. When the length of the device is much longer than l_{mfp} , the device is diffusive; that is, the electron paths are randomized. However, since elastic collisions preserve phase, electron wavefunctions can still interfere, resulting in phenomena such as weak localization and universal conductance fluctuations, which are hallmarks of diffusive two-dimensional quantum transport [46].

Similarly, the inelastic scattering length l_{in} is the distance electrons travel ballistically between inelastic, phase-randomizing scattering events. Typically, $l_{\text{in}} \gg l_{\text{mfp}}$ at the low temperatures ($T \sim 50$ mK) used in experiments throughout this dissertation. Therefore, in a device large enough to be in a diffusive regime, many elastic collisions will occur between each phase-breaking collision, and the effective device length over which the phase remains coherent is reduced due to diffusion. Thus, a more experimentally-relevant quantity is the effective phase coherence length, which is related to the elastic and inelastic scattering lengths by $l_\phi^2 = l_{\text{mfp}}l_{\text{in}}/d$, where d is the dimensionality. Whether a specific device is ballistic or diffusive depends on the relationship between the mean free path and the size of the device length and width; whether a device behaves classically or quantum mechanically, with the phase of the electron wavefunction affecting transport, depends on the relationship between phase coherence length and the device length and width.

For example, if a nanowire-based quantum dot has dimensions smaller than the phase coherence length, quantum tunneling can occur through the dot. As the transparency of the tunneling barriers is increased, the dot becomes conducting, and the barriers act as large scattering centers. If the elastic scattering length is smaller than the length between the barriers, the barriers will just be two among many scattering centers contributing to coherent but diffusive transport; application of a magnetic field would likely produce universal conductance fluctuations expected for diffusive quantum transport. However, if the length between the barriers is smaller than the elastic scattering length, scattered electrons will interfere in a way identical to an optical Fabry-Perot cavity, creating a quasi-periodic pattern of quantum oscillations in the conductance.

Another important length scale is the inter-electron distance, which can be estimated from the carrier density as $l_{e-e} = n^{-1/d}$. When an electron system is confined, e.g. at an interface, in a plane with a height close to l_{e-e} , the system is quasi-two-dimensional. Similarly, if a channel has both height and width near l_{e-e} , the channel can be called quasi-one-dimensional. At the LaAlO₃/SrTiO₃ interface, a typical two-dimensional carrier density of $1 \times 10^{13} \text{ cm}^{-2}$ gives an average inter-electron distance $l_{e-e} \approx 3 \text{ nm}$. This means that nanowires created with c-AFM lithography (described in § 2.2), which have a width around 10 nm, operate near the one-dimensional regime.

For 1D systems in the quasi-ballistic or ballistic regime (channel length is close to or much smaller than the mean free path), the conductance becomes quantized in units of e^2/h [47]. Quasi-1D transport was first reported in narrow constrictions, also known as “quantum point contacts” [48, 49]. The conductance through these narrow channels is given by the number of allowed transverse modes, which is tunable by an external gate. The confined ballistic regions are generally short, of the order 100 – 200 nm, with a channel length set by the distance between the top gate electrodes and the high-mobility buried layer. There have been many attempts to engineer more extended 1D quantum wires using other growth techniques and different materials. For example, cleaved-edge overgrown III-V quantum wires exhibit quantized transport in devices as long as 2 μm [50]. Other one-dimensional systems include carbon nanotubes [51], graphene nanoribbons [52], and compound semiconductor nanowires [50, 53]. In all of these systems, electron transport is sensitive to minute amounts of disor-

der. For example, when 2D semiconductor heterostructures are patterned into 1D channels, the mobility drops tremendously [54]. Theoretically, this sensitivity to disorder can be understood within the framework of Tomonaga-Luttinger liquid theory, which predicts that repulsive interactions promote full backscattering from even a single weak impurity [55, 56]. Conversely, attractive interactions are predicted to strongly suppress impurity scattering [56, 57].

The 2D electron mobility in LaAlO₃/SrTiO₃ interfaces is relatively low ($\mu \sim 10^3$ cm²/Vs) compared with high-mobility GaAs/AlGaAs heterointerfaces ($\mu \sim 10^7$ cm²/Vs). However, despite the modest mobility of the LaAlO₃/SrTiO₃ 2D interface, there is an increasing body of evidence suggesting that 1D geometries are able to support ballistic transport [58, 59, 60, 10]. This will be explored in Chapters 5 and 6.

Additionally, since the LaAlO₃/SrTiO₃ interface is superconducting, it is useful to keep in mind the relevant superconducting length scales: the superconducting coherence length ξ and the London penetration depth λ . In optimally-doped bulk SrTiO₃, λ is close to a micron due to the very low carrier density [29]. At the LaAlO₃/SrTiO₃ interface, the conducting system extends about 10 nm into the SrTiO₃, so the thickness of the superconducting system is much less than the penetration depth. In the case of two-dimensional superconductivity, where $d \ll \lambda$, a more useful parameter is the Pearl length, $\Lambda = 2\lambda^2/d$. In LaAlO₃/SrTiO₃, this is estimated to be nearly 10 μ m [29]. The superconducting coherence length is around 50-100 nm for both bulk SrTiO₃ [20] and the LaAlO₃/SrTiO₃ interface [4].

2.0 EXPERIMENTAL METHODS

This chapter describes in detail the experimental methods used in the following work. In particular, it presents sample growth methods, the canvas fabrication photolithography process, c-AFM lithography methods, and low-temperature transport methods.

2.1 $\text{LaAlO}_3/\text{SrTiO}_3$ SAMPLE PREPARATION

2.1.1 Sample Growth

$\text{LaAlO}_3/\text{SrTiO}_3$ samples are grown using pulsed laser deposition by Sangwoo Ryu, Hyungwoo Lee and Jung-Woo Lee in Prof. Chang-Beom Eom's research group in the Department of Materials Science and Engineering at the University of Wisconsin-Madison [61, 62, 63]. The commercially-purchased single-crystal SrTiO_3 substrates are cut in the (001) orientation, resulting in alternating layers of SrO and TiO_2 . Before LaAlO_3 is grown on these substrates, the (001) crystals are TiO_2 -terminated by etching in buffered HF for 60 seconds either once or twice to improve substrate quality, and annealed at 1000°C for 2 – 12 hours to achieve an atomically smooth surface with single unit cell height steps. A thin (3.4 unit cell) LaAlO_3 film is epitaxially grown on top of SrTiO_3 by pulsed laser deposition at a temperature of 550°C and 1×10^{-3} mbar oxygen pressure, and gradually cooled to room temperature. Precise layer-by-layer film growth is monitored in-situ by high-pressure reflection high-energy electron diffraction (RHEED). Peaks marked by vertical lines in Fig. 3(a) indicate the deposition of each complete LaAlO_3 unit cell. Atomic force microscopy image and profile of LaAlO_3 surface topography (Fig. 3(b,c)) show the single unit cell height steps.

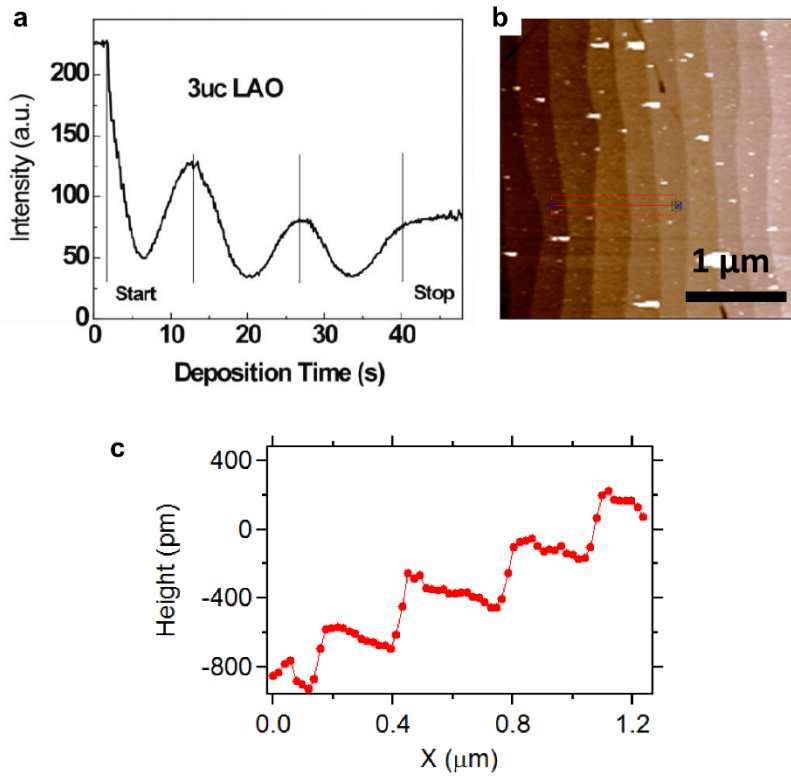


Figure 3: LaAlO_3 growth on SrTiO_3 substrate. **a**, RHEED intensity oscillations during film growth. **b**, AFM height image of LaAlO_3 surface. **c**, Height profile along red linecut in (b).

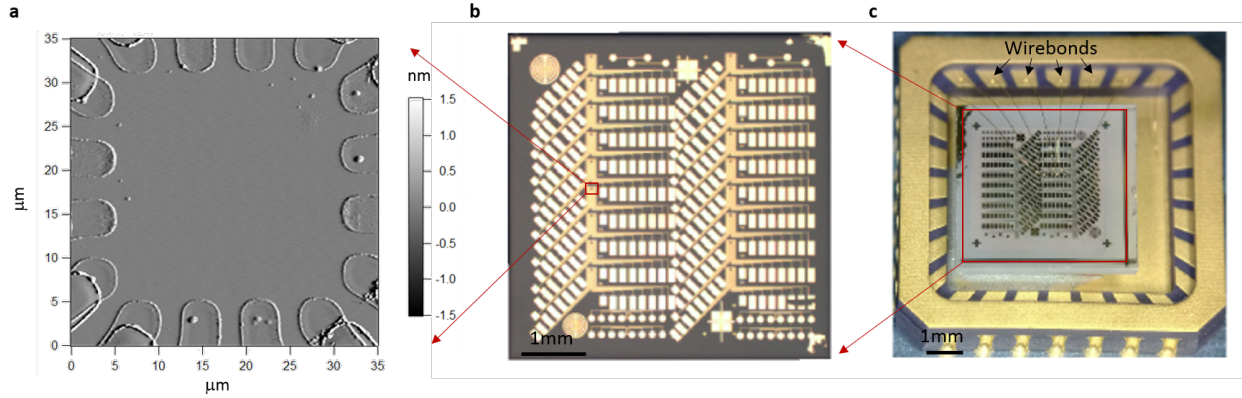


Figure 4: $\text{LaAlO}_3/\text{SrTiO}_3$ canvases. **a**, AFM deflection image of a canvas surrounded by 16 interface electrodes. **b**, Optical image ($5 \text{ mm} \times 5 \text{ mm}$) of a sample with 18 canvases, each with an associated 16 bonding pads. **c**, Optical image of sample on chip carrier with wirebonds.

2.1.2 Canvas Fabrication

Once the samples are delivered to our lab in Pittsburgh, conventional photolithography, ion etching, and sputtering techniques are used by lab members Mengchen Huang and Jianan Li to pattern electrical contacts to the $\text{LaAlO}_3/\text{SrTiO}_3$ interface, forming “canvases” on which we can “draw” interface nanowires (See §2.2 for details on creation of nanowires). A typical $5 \text{ mm} \times 5 \text{ mm}$ sample contains 18 canvases (Fig. 4(b)). Each canvas is defined by 16 interface contacts forming a $30 \mu\text{m} \times 30 \mu\text{m}$ square (Fig. 4(a)). Gold electrodes deposited on the surface extend from each of the interface contacts to a macroscopic bonding pad. A wirebond machine is used to form gold wirebonds from the bonding pads to the ceramic chip carrier (Fig. 4(c)) to obtain electrical connection with various laboratory instruments. The samples are glued to the chip carrier using conductive silver epoxy, which allows backgating (notice the wirebond to the far left in Fig. 4(c)).

To create the canvases, photolithography is used to pattern the structures. Photoresist AZ4210 is uniformly spin-coated to $2.1 \mu\text{m}$ thickness on the LaAlO_3 surface and soft-baked at 95°C for 1 minute (Fig. 5(b)). The photoresist is then exposed to $\lambda = 320 \text{ nm}$ UV light, using a photomask with a mask-alignment system to selectively let through UV light, thereby transferring the predefined pattern onto the photoresist layer. After UV exposure, the sample is soaked in developer (AZ400K), which dissolves the exposed photoresist (Fig. 5(c)).

The sample is then put in a vacuum chamber and electrical contact to the interface is made by using a high energy (500eV) Ar^+ beam to etch 25 nm, through the exposed LaAlO_3 and deep into the SrTiO_3 (Fig. 5(d)). Areas still covered with photoresist are protected from the ion milling. Sputter deposition is performed to deposit interface contacts (Fig. 5(e)). First 4 nm of Ti are deposited to serve as an adhesion layer, followed by 20 – 25 nm of Au, which makes an ohmic contact to the $\text{LaAlO}_3/\text{SrTiO}_3$ interface. Finally, the photoresist is removed by the lift-off process, in which the sample is soaked in 1165 photoposit remover for several hours and then ultrasonically cleaned for 2 minutes while submerged in acetone and isopropanol alcohol (Fig. 5(f)). The photoresist dissolves and any metal on the photoresist washes away, leaving only the patterned interface electrodes. The photolithography and sputtering steps are repeated a second time to form the surface electrodes (Fig. 5(g–j)). Any photoresist residue left on the sample surface is removed by oxygen plasma cleaner at 100 W for 24 seconds (Fig. 5(k)).

2.2 c-AFM LITHOGRAPHY

The interface between the two complex oxides LaAlO_3 and SrTiO_3 has remarkable properties that can be locally reconfigured between conducting and insulating states using a conductive atomic force microscope (c-AFM). The c-AFM fabrication technique [64] provides great versatility in the creation of nanoscale devices, including nanowire junctions [64], sketched field-effect transistors (SketchFETs) [64], photodiodes [65], THz emitters and detectors [66], and sketched single-electron transistors (SketchSETs) [67].

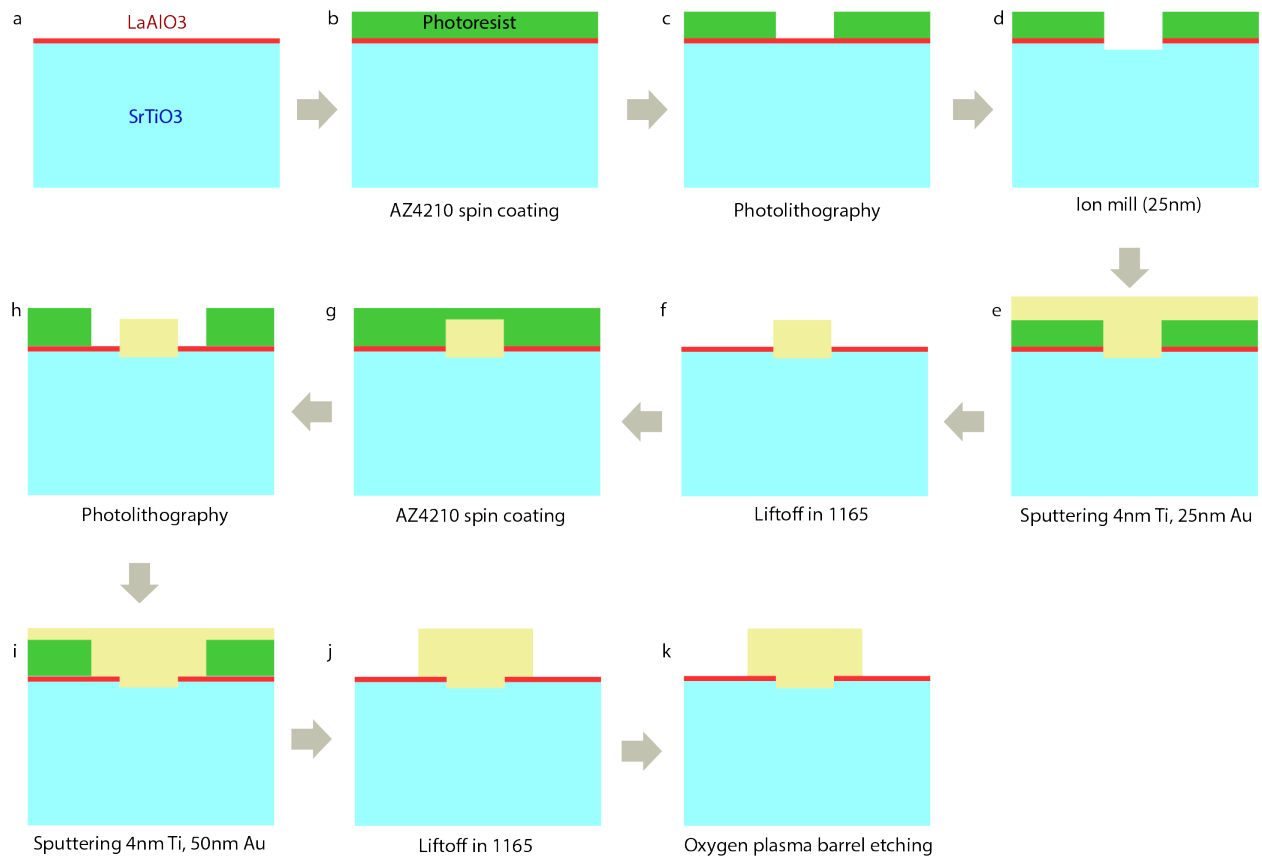


Figure 5: Photolithography procedure. **a**, Unpatterned sample. **b—f**, Photolithography, ion milling and sputtering steps to deposit interface electrodes. **g—j**, Photolithography and sputtering steps to deposit surface electrodes. **k**, Final oxygen plasma cleaning step.

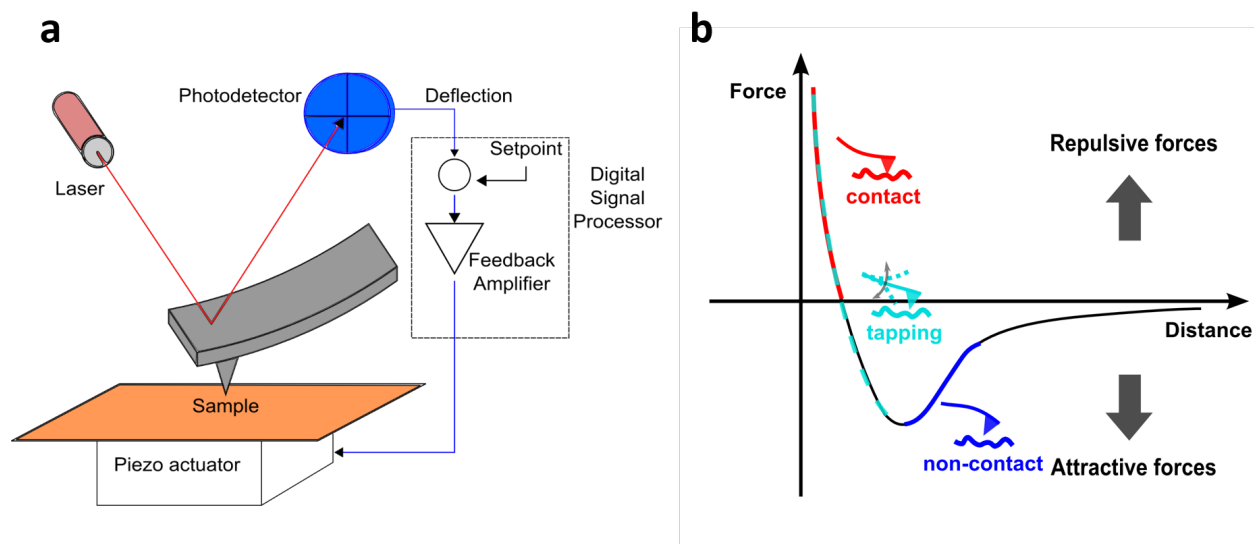


Figure 6: AFM operation. **a**, Schematic of the essential components for contact mode AFM. **b**, Illustration of force-distance curves and corresponding AFM modes. Adapted from <http://www.teachnano.com/education/AFM.html>.

2.2.1 AFM Operation

Atomic force microscopy (AFM) is a member of a family of scanning probe techniques that originated with scanning tunneling microscopy (STM) in 1981 [68]. When it was found that significant forces between the tip and the substrate surface atoms had to be accounted for in STM experiments, it was speculated that those same atomic forces could provide the basis for a second type of scanning probe microscopy [69]. With the realization of atomic force microscopy [70], it was expected that near-atomic resolution could be achieved for insulators as well as metals, and without the need for high-vacuum conditions or special surface preparation [69]. In the three decades since its birth, AFM has matured into a widely-used technique with many variations, including force sensing, lithography, nanomanipulation, and nanoindentation, to characterize and manipulate materials at the nanoscale.

AFM uses a very sharp tip with a radius of curvature on the order of 10 nm to obtain high-resolution topography of a sample surface (see Fig. 6(a)). As the tip, which is mounted

under a cantilever, scans across the surface, the atomic forces between the atoms at the end of the tip and the atoms of the sample surface cause the cantilever to bend. This bending of the cantilever is detected and converted into height information. Cantilever movement is typically detected by shining a laser onto the top of cantilever, which has a highly-reflective coating. The laser spot reflects onto a quad-segmented photodetector; vertical bending or lateral twisting of the cantilever is revealed in the position of the laser spot on the photodetector, and the analog output of the photodiodes is called deflection.

There are three distinct modes in which AFM can be performed: contact, tapping and non-contact. In contact mode, the tip is pressed into direct contact with the sample surface so that the atomic forces are repulsive, as opposed to non-contact, where the tip is oscillated above the sample surface and atomic forces are attractive. Tapping mode exists between these two, as shown in Fig. 6(b).

Here we use contact mode in an Asylum MFP3D AFM to image the canvases and perform conducting AFM (c-AFM) lithography. In contact mode, the force exerted on the sample by the tip, given by $F = -k \times D$, where k is the cantilever’s spring constant and D is the deflection distance, is kept constant. This is achieved using a feedback loop where the deflection signal from the photodetector serves as the error signal, and the feedback output adjusts the height of the cantilever by controlling the Z-piezo. Mapping the Z-piezo height change as a function of position results in a surface topography image.

2.2.2 c-AFM Lithography

For $\text{LaAlO}_3/\text{SrTiO}_3$ samples grown with an LaAlO_3 thickness just below the critical thickness of 4 u.c. at which the two-dimensional electron liquid forms, the interface is insulating, but reversibly and hysteretically tunable through the metal-insulator transition (MIT) by use of a back gate, or a top gate [26]. A voltage-biased c-AFM tip placed in contact with the LaAlO_3 surface can locally induce the MIT at the interface. Positive voltages ($V \sim +10$ V) applied to the tip locally switch the $\text{LaAlO}_3/\text{SrTiO}_3$ interface to a conductive state (“write”), while negative voltages ($V \sim -10$ V) applied to the tip locally restore the $\text{LaAlO}_3/\text{SrTiO}_3$ interface to an insulating state (“erase”). Moving the positively-biased tip across the surface creates

conducting structures less than 10 nm wide [71] at the interface. Moving the negatively-biased tip perpendicularly across an existing nanowire “cuts” the nanowire (see Fig. 7(b)). The width profile of the current drop (blue line in Fig. 7(b)) allows an estimation of the nanowire width at room temperature; typical widths are between 2-20 nm.

When a very small negative voltage ($-0.05 \text{ V} < V_{tip} < -0.5 \text{ V}$) is used to cut a nanowire, the nanowire will remain conducting; however, a nanoscale potential barrier is created in the wire. The size of the barrier is characterized by monitoring the change in resistance during the cutting process at room temperature. Using these “write” and “erase” c-AFM procedures, a number of reconfigurable nanostructures can be created with nanoscale precision ($\sim 2 \text{ nm}$).

2.2.3 Water-Cycle Mechanism

The mechanism for writing (erasing) is attributed to protonation (de-protonation) of the LaAlO_3 surface [72, 73]. Water molecules in the atmosphere dissociate into H^+ and OH^- , which adsorb on the LaAlO_3 surface (Fig. 8(a)). A positively-biased c-AFM tip removes some of the OH^- ions, leaving a path of excess H^+ on the surface (Fig. 8(b)). The protonated LaAlO_3 surface in critical-thickness $\text{LaAlO}_3/\text{SrTiO}_3$ heterostructures creates an attractive confining potential that defines the nanowire. A negatively-biased c-AFM tip removes H^+ ions from the surface, restoring a balanced surface charge density so that the net attractive potential disappears and the insulating state is restored at the interface (Fig. 8(c)). This water-cycle mechanism allows for multiple write-erase cycles without physically modifying the heterostructure [73].

Because the protons are physically separated from the conducting region by a highly insulating LaAlO_3 barrier, this nanofabrication method can be viewed as analogous to the modulation doping technique [74] commonly used in III-V semiconductor heterostructures. The separation of dopants from the conducting region minimizes scattering from imperfections; this suggests that c-AFM lithography may be a very useful technique to reduce dimensionality while not disturbing transport by introducing disorder in the way more conventional lithography techniques tend to do. A key difference from III-V nanostructures is the relative proximity between the dopant layer and conducting channel, here only 1.2 nm.

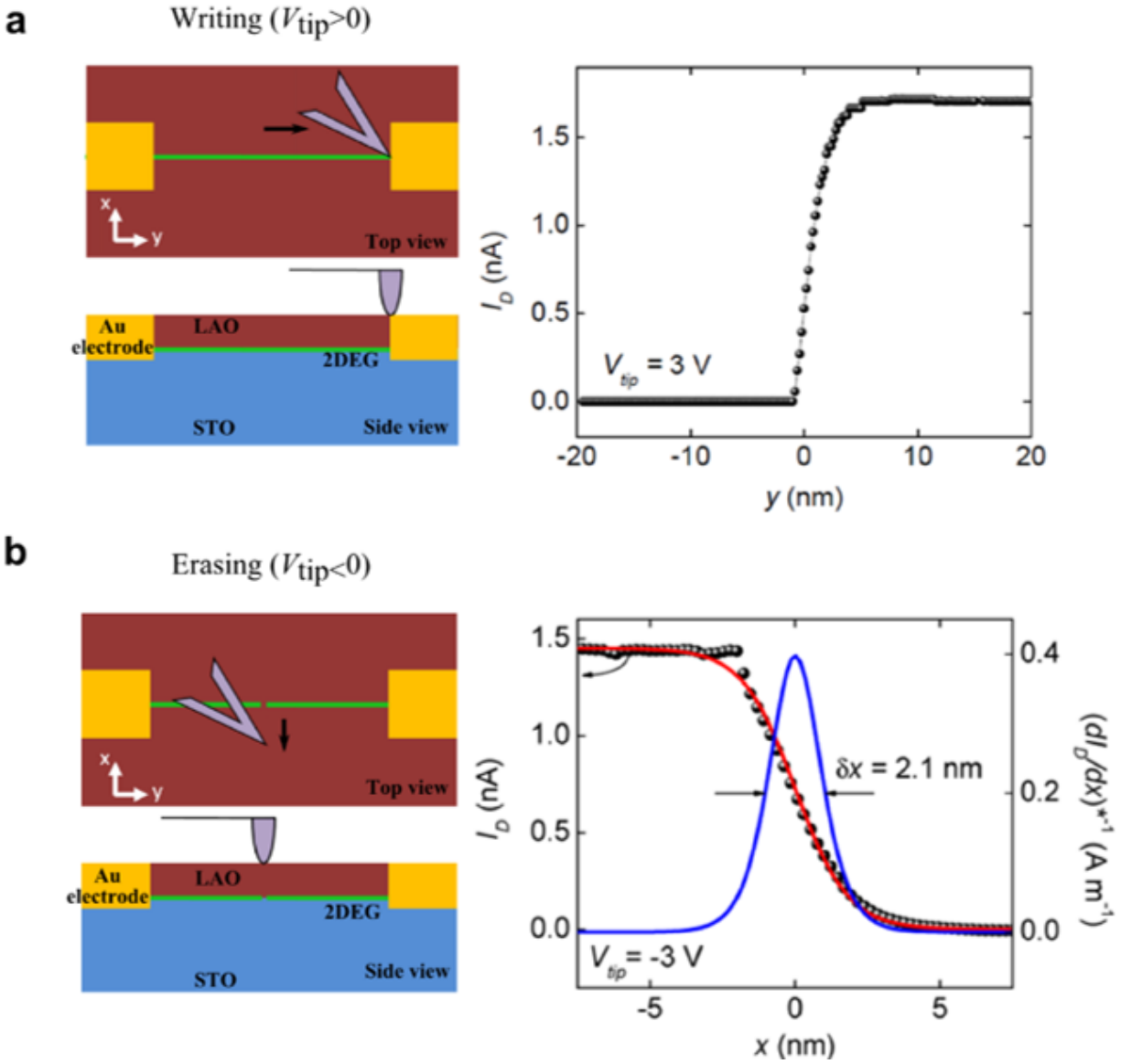


Figure 7: c-AFM procedure. **a**, As a positively-biased c-AFM tip moves across the green path, a conducting nanowire is formed at the interface (left panel). This allows a current (right panel) to be measured between the gold electrodes. **b**, A negatively-biased tip, moved across the wire (left panel), locally restores the insulating state at the interface. “Cutting” the nanowire results in the current dropping to zero (right panel). Data is adapted from Ref. [71].

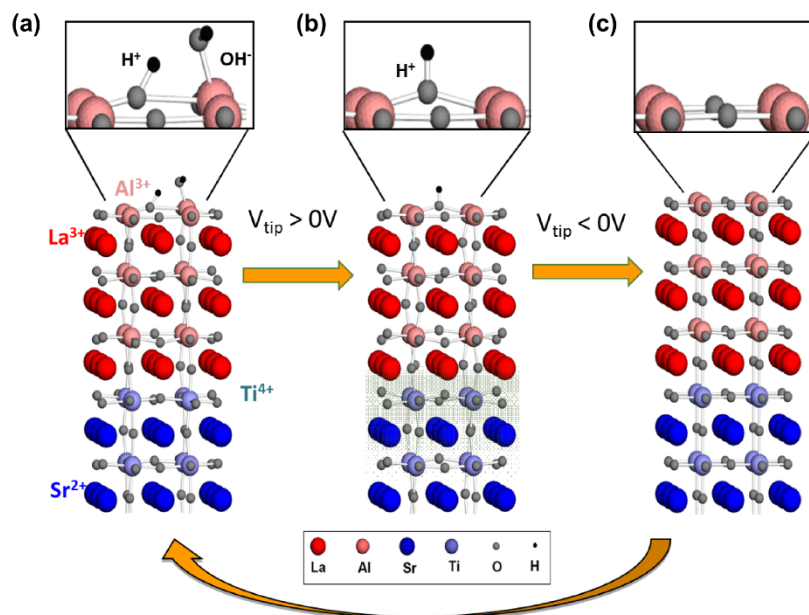


Figure 8: Water-cycle mechanism for c-AFM lithography. **a**, In atmosphere, water dissociates and is adsorbed on the LaAlO₃ surface. **b**, Writing removes OH⁻, leaving H⁺ ions to effectively modulation-dope the interface. **c**, Erasing restores ionic balance at the surface, and the insulating state at the interface. (Adapted from C. S. Hellberg, APS talk)

2.3 LOW-TEMPERATURE TRANSPORT

This section describes the hardware, software, and experimental techniques used to perform the low-temperature transport measurements reported in later chapters.

2.3.1 Physical Property Measurement System Operation

A Quantum Design Physical Property Measurement System (PPMS) is used to bring the samples to low temperatures and apply magnetic fields up to ± 9 T. Immediately after creating a device with c-AFM lithography in an Asylum Research AFM, the sample is transferred to the PPMS and put under vacuum within 5 minutes, and the temperature reaches below the freezing point of water within 10 minutes.

The innermost part of the PPMS consists of a sample probe surrounded by a superconducting magnet (Fig. 9(a)). The probe and magnet are submerged in a liquid helium bath (inner part pictured in Fig. 9(b)), which is surrounded by vacuum jackets (colored blue) and an outer liquid nitrogen jacket (colored green) to reduce the helium boil-off rate. At atmospheric pressures, the boiling temperature of helium is 4 K; however, a base temperature of 1.8 K is achieved by pumping on the helium bath.

2.3.2 Superconducting Magnet Operation

Magnetic fields of up to ± 9 T are applied using a superconducting magnet, labeled in Fig. 9(a). Superconducting wire is wrapped around the sample space; a magnetic field is created inside the sample space, where the sample is located, by running current through the coil. The wire is made out of superconducting material with a large critical current, which allows large currents to be carried, achieving large magnetic fields. The magnet circuit is shown in Fig. 9(c), with the superconducting wire in blue. The magnet operates in two modes: “driven” and “persistent”. In driven mode, pictured in Fig. 9(c), a small heater circuit is closed, which opens the persistent switch. The current is forced to run through the magnet power supply, so the power supply can be used to change the current (and therefore the magnetic field). The current measured through the driven circuit is calibrated to the

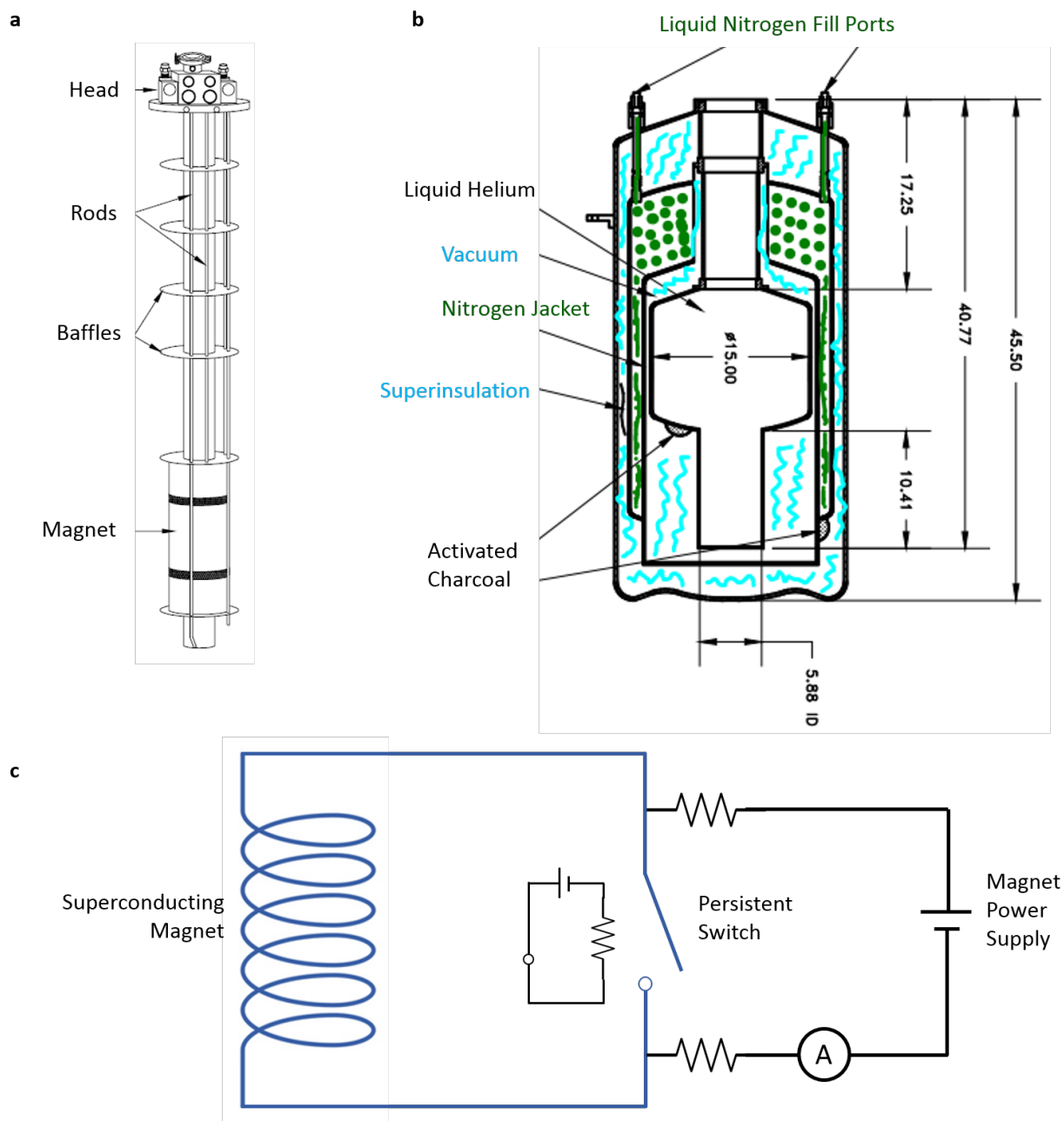


Figure 9: PPMS schematic. **a**, Sample probe and magnet. **b**, PPMS dewar components. Sample probe in (a) is inserted into the liquid helium bath space during installation. (adopted from PPMS hardware manual) **c**, Superconducting magnet circuit.

strength of the magnetic field at the sample position by the manufacturer, and afterward is used to determine the magnetic field strength. When the persistent switch is closed, the magnet is in persistent mode, with a fully superconducting circuit and no dissipation. The magnetic field strength at the sample is then constant, and the magnet power supply can be turned off; this mode conserves helium.

2.3.3 Dilution Refrigerator Operation

For the results presented in this thesis, a Quantum Design dilution refrigerator (DR) insert is used in conjunction with the PPMS to achieve a base temperature of 50 mK. The DR is inserted in the PPMS sample space, and utilizes a turbopump and diaphragm pump to circulate the 33% ^3He /66% ^4He mixture. As shown in Fig. 10(a), the mixture phase-separates in the mixing chamber into a concentrated (dark blue), mostly- ^3He phase and a dilute ($\sim 6\%$ ^3He , light blue) phase. Pumping on the still with the turbopump decreases the still temperature to around 600 mK, and reduces the ^3He concentration in the still. This draws ^3He from the concentrated phase into the dilute phase in the mixing chamber, which absorbs heat, providing cooling power to the sample stage. The turbopump is backed by a diaphragm pump which then sends the ^3He gas through the condenser. The liquid ^3He then flows through the impedance, into the still heat exchanger and through the continuous heat exchanger, where the liquid ^3He is further cooled before returning back into the concentrated side of the mixing chamber.

2.3.4 Software: LabVIEW

LabVIEW is utilized to interface with the data acquisition (DAQ) hardware in both the MFP3D AFM and PPMS setups. A crucial aspect is the software-based lock-in amplifier, which is used to apply voltage signals to the device. This same software program measures voltage and current signals from the device, and is able to perform lock-in demodulation of those measured signals.

There are two typical types of measurements performed, direct current (dc) and alternating current (ac), colloquially termed “I-V” and “lock-in”. I-V measurements use a low

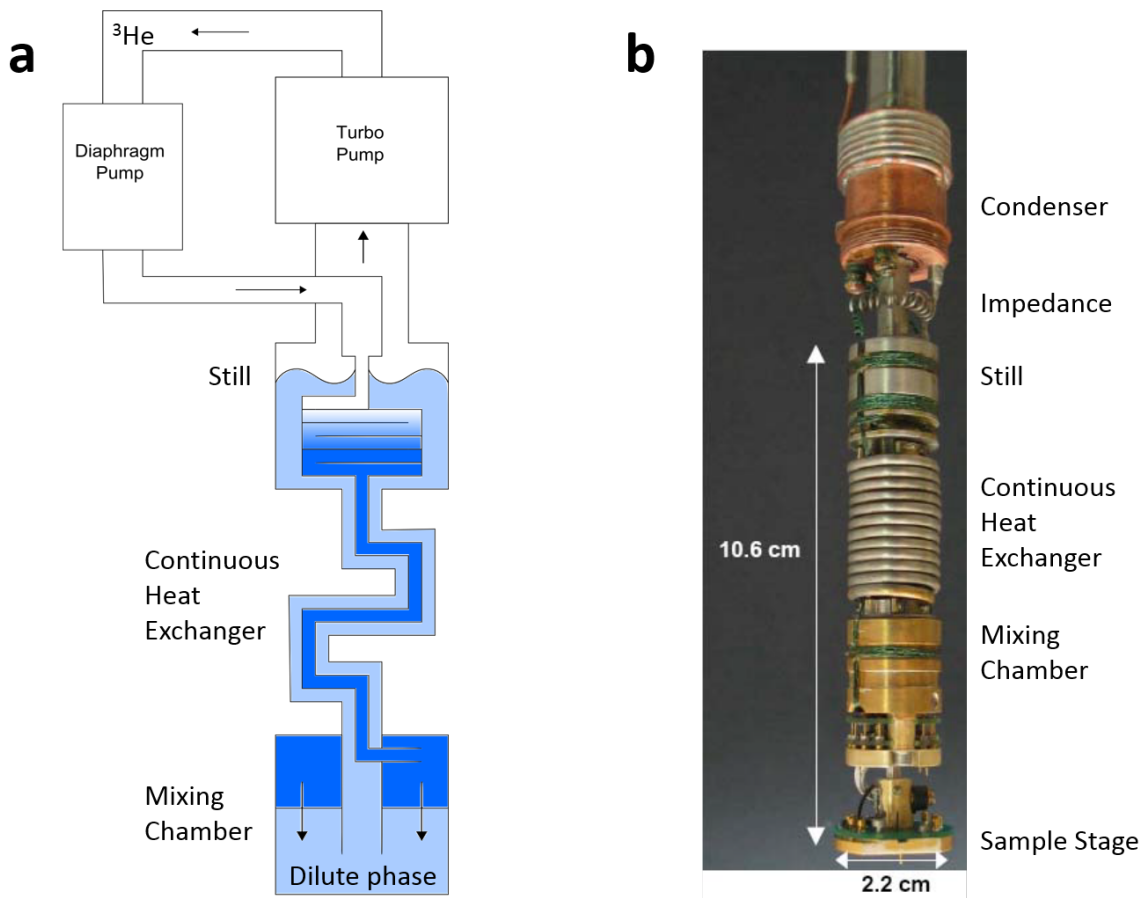


Figure 10: DR components.

ac oscillation frequency ($0.2 - 1$ Hz), large ac oscillation amplitude ($1 - 3$ mV), and typically a sawtooth or triangle waveform, shifted in phase by 180 degrees. While the lock-in program is used to source this voltage signal, no demodulation of the measured signal is performed; instead, the full waveform of the sourcing voltage and the measured current and voltage signals are used to achieve 2-terminal (measured current versus sourcing voltage) and 4-terminal (measured current versus measured differential voltage) $I - V$ curves, revealing details of zero- and finite-bias transport behavior. On the other hand, lock-in measurements use a fast ac oscillation frequency (in this work, typical frequencies are $1.346 - 13.46$ Hz), small ac oscillation amplitude (~ 100 μ V to obtain an effectively zero-bias measurement), and sine waveform. The lock-in program demodulates the measured current and voltage signals with respect to the fast sourcing frequency to obtain a single current or voltage value for each cycle. This type of measurement can be used to perform fast, sensitive experiments; for example, to examine the zero-bias conductance while sweeping a side-gate and magnetic field.

2.3.5 Hardware

2.3.5.1 Peripheral Component Interconnect Extension (PXI) The PXI chassis (Fig. 11(a)) holds several PXI cards with DAQ analog inputs (AI) and analog outputs (AO) (Fig. 11(b); red box in (a)). AO channels are used as voltage sources. If the AO channel is to be used as a gate voltage, a large series resistor (~ 100 M $\Omega - 1$ G Ω) is used to limit any potential current flow. Gate voltages are typically much larger than source-drain voltages ($V_{gate} \sim 100$ mV; $V_{sd} \sim 1$ mV), and could result in hundreds of nanoamperes of current running through the nanowire. Large currents are likely to damage the nanowires; the transport properties would irreversibly and drastically change, likely becoming completely insulating, or more colloquially, being “fried”. AI channels receive the signals from the sample, after passing through transimpedance or differential voltage amplifiers (Femto models DDPCA-300 and DLPVA, Fig. 11(c, d); green box in (a)). The signals from the AO channels are then demodulated by the lock-in program to give the measured voltage or current reading.

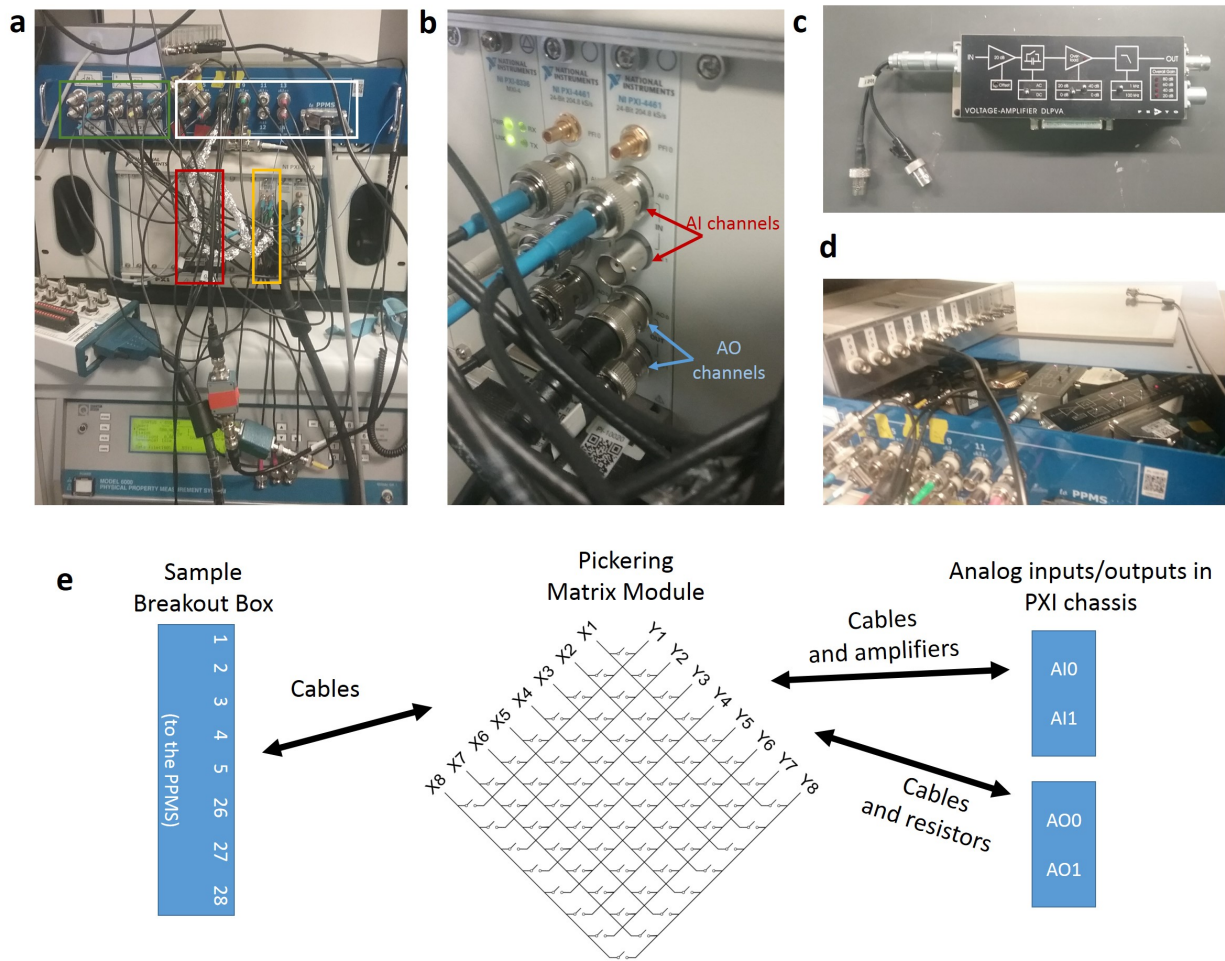


Figure 11: DAQ setup.

2.3.5.2 Pickering At low temperatures, it is desirable to switch the measurement configuration without physically touching the cable connections. Small static discharge, which is unnoticeable at room temperature, can damage the nanowires at low temperatures. Therefore, a Pickering Matrix Module (yellow box, Fig. 11(a)) is used. The eight electrodes coming from the sample breakout box (white box, Fig. 11(a)) are electrically connected to the X-channels in the Pickering Matrix (Fig. 11(e)). The AO and AI channels are connected (sometimes with resistors or amplifiers in between, as described above) to the Y-channels. Inside the Pickering, any crosspoint matrix can be achieved between the X and Y channels, and they all share a common ground. A LabVIEW program interfaces with the Pickering Matrix Module to set the desired measurement configurations.

3.0 ELECTRON PAIRING WITHOUT SUPERCONDUCTIVITY

3.1 INTRODUCTION

The contents of this chapter represent a collaborative work published in Cheng, Tomczyk, Lu, Veasey, Huang, Irvin, Ryu, Lee, Eom, Hellberg and Levy, *Nature* **521** 196, 2015 May 14. The attractive Hubbard model calculation in § 3.4.2 was performed by C. S. Hellberg.

The superconducting single-electron transistor (SSET), consisting of an electrically gated superconducting quantum dot (QD) coupled to superconducting leads by tunneling barriers, presents a particularly powerful tool for probing fundamental properties of superconductors [75]. Generally, transport characteristics depend on the relative magnitudes of the charging energy E_c , superconducting gap energy Δ , and orbital level spacing δE in the QD. Transport signatures of metallic superconducting islands include even—odd parity effects, Cooper pair tunneling, and parity-affected superconductivity [76].

Here we perform transport experiments with nanowire-based single-electron transistors at the interface between SrTiO₃ and a thin layer of lanthanum aluminate, LaAlO₃. Electrostatic gating reveals a series of two-electron conductance resonances—paired electron states—that bifurcate above a critical magnetic field B_p of about 1–4 tesla, an order of magnitude larger than the superconducting critical magnetic field. For magnetic fields below B_p , these resonances are insensitive to the applied magnetic field; for fields in excess of B_p , the resonances exhibit a linear Zeeman-like energy splitting. Electron pairing is stable at temperatures as high as 900 mK, well above the superconducting transition temperature (~ 300 mK). These experiments demonstrate the existence of a robust electronic phase in which electrons pair without forming a superconducting state. Key experimental signatures are captured by a

model involving an attractive Hubbard interaction that describes real-space electron pairing as a precursor to superconductivity.

3.2 DEVICE GEOMETRY AND FABRICATION

Quantum transport measurements are performed on $\text{LaAlO}_3/\text{SrTiO}_3$ SSETs fabricated by conductive atomic force microscope (c-AFM) lithography [71, 64]. The devices are constructed from three basic elements: superconducting nanowires [77], nanoscale potential barriers created by c-AFM erasure [67] and electrical side gates. Figure 12(a) shows a schematic of a typical structure, consisting of a nanowire (between leads 1 and 5) of width $w \approx 5$ nm, three voltage probes (leads 2-4) and a side gate. Voltage leads are located a distance $L = 2.5 \mu\text{m}$ apart, separating the main channel into two segments. The upper segment (between leads 2 and 3) is open, that is, without barriers, while the lower nanowire segment forms an $L_{QD} = 1 \mu\text{m}$ QD bounded by two barriers. A side gate tunes the chemical potential of both the upper wire and the QD, and modulates the tunnel coupling between the QD and the external leads.

In this work, c-AFM lithography is used to create 58 QD devices with varying dimensions (for example, $250 \text{ nm} < L_b < 1 \mu\text{m}$) and barrier heights R (see section § 3.2.2 below) and on multiple SrTiO_3 substrates. We show data from eight representative devices named A through H; device parameters for all eight devices are summarized later in Table 1 in § 3.4.1.1. We primarily focus on data from device A (Figs. 12,15,16), which exhibits features qualitatively similar to the whole set of devices.

3.2.1 Barrier Fabrication

In Fig. 13(a), a single barrier device, which has a similar design to device A but contains only one barrier instead of two, is shown in order to demonstrate the barrier fabrication technique. During barrier fabrication, the four-terminal resistance difference $\Delta R = R_{QD} - R_o$ is monitored in real time and serves as a figure of merit for low-temperature barrier

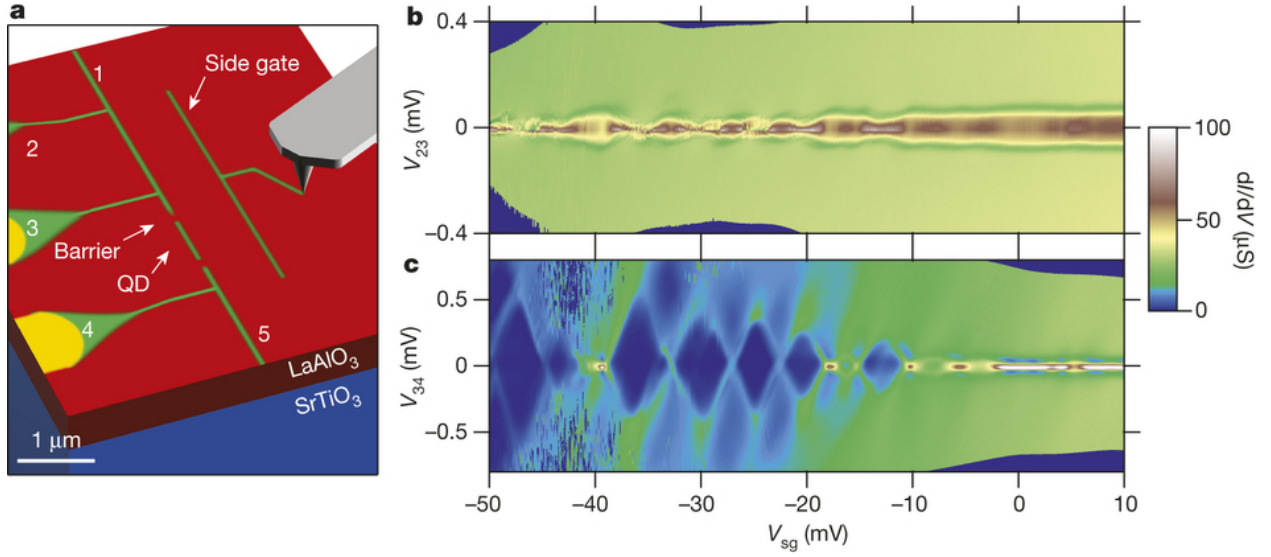


Figure 12: Device schematic and transport characteristics. **a**, Device schematic. The nanowire width $w = 5$ nm, the nanowire QD length is $1 \mu\text{m}$, and barriers are $0.75 \mu\text{m}$ away from the sense leads 3 and 4. The length of the open wire is $2.5 \mu\text{m}$, equal to the nanowire QD length plus total distances from barrier to sense leads. **b**, dI/dV characteristics (color coded) as a function of four-terminal voltage V_{23} and side gate voltage V_{sg} in the open wire in device A. **c**, dI/dV characteristics of the nanowire QD in device A measured simultaneously with data shown in (b).

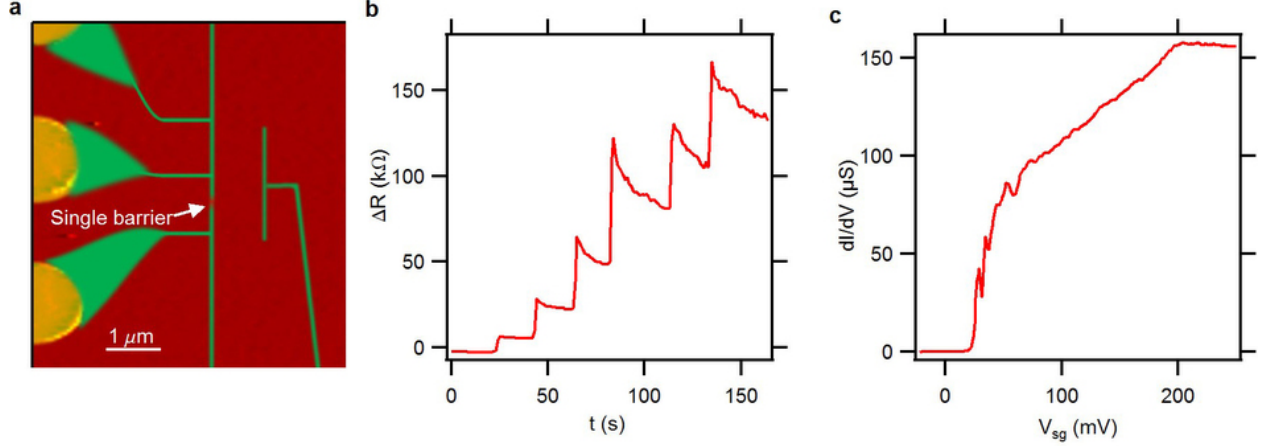


Figure 13: Nanoscale potential barrier engineering and low-temperature transport characteristics. **a**, Single-barrier device schematic. It has the same structure as device A except that only one barrier is integrated in the design. **b**, Resistance change during barrier cutting (Methods); t is time. **c**, The differential conductance dI/dV as a function of V_{sg} at $T = 75$ mK. The wire can be pinched off by V_{sg} at the barrier site.

performance, where R_{QD} and R_o are the resistances of the QD wire and the open wire. R_{QD} and R_o are obtained simultaneously by two four-terminal measurements using two hardware-simulated lock-in amplifiers, such that wire decay is eliminated from the measurement and ΔR is very precise. Prior to barrier cutting, R_{QD} and R_o are nominally the same with $\Delta R < |5|$ k Ω (within 1% difference). A sharp AFM tip (nominal radius of curvature ~ 8 nm) moves perpendicularly across the wire at 200 nm s^{-1} speed with small negative voltages (-0.1 V to -0.5 V) multiple times, which causes ΔR to increase discretely, as shown in Fig 13(b). Low-temperature transport study ($T = 75$ mK) shows the wire conductance can be pinched off by V_{sg} for a single barrier device with $\Delta R \approx 120$ k Ω . The conductance oscillations (30 mV $< V_{sg} < 50$ mV) indicate quantum mechanical tunneling through the barrier (Fig. 13(c)).

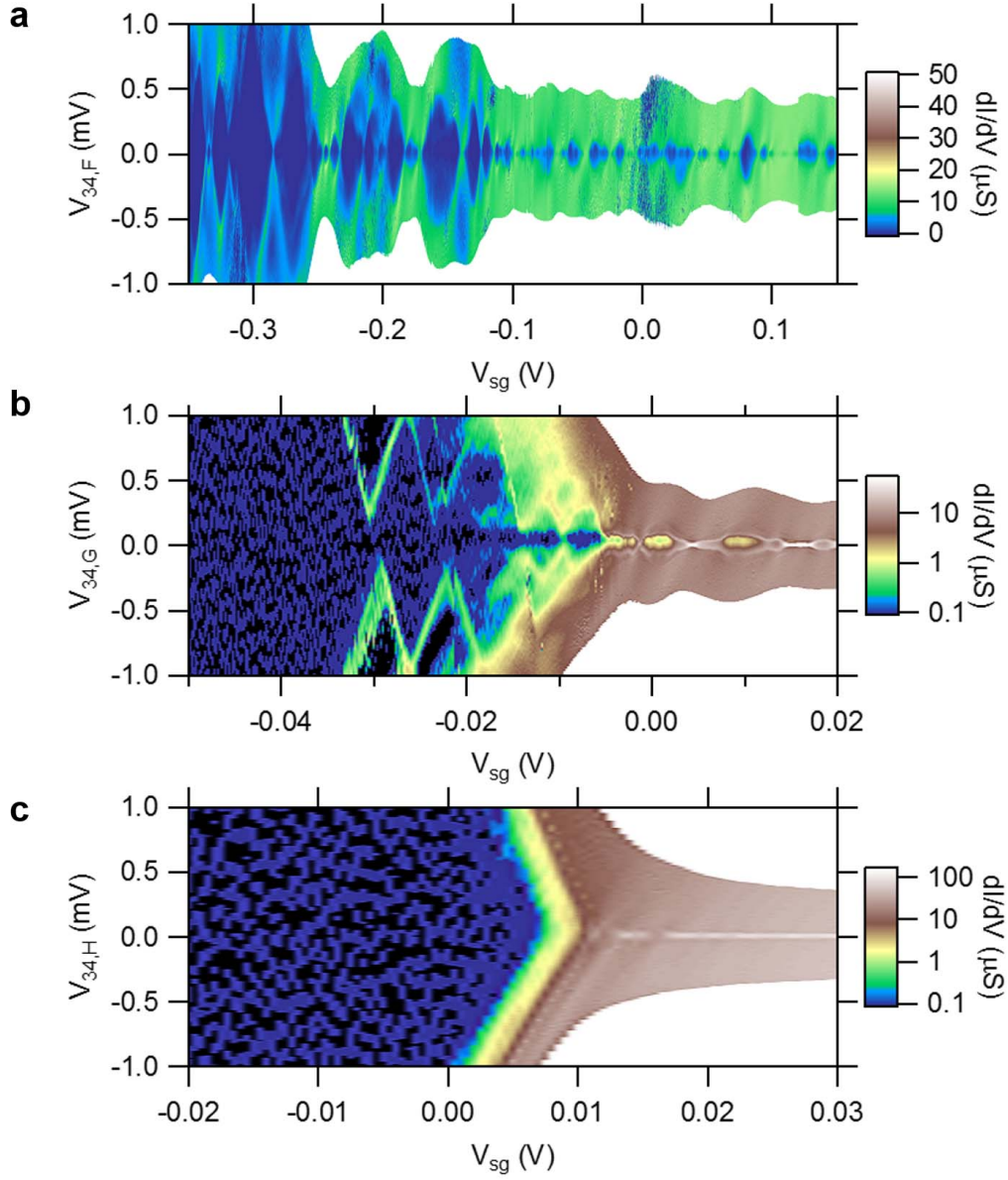


Figure 14: Transport properties of three 500 nm confined nanowire devices of different single barrier heights at $T = 50$ mK. Plots show color-coded dI/dV as a function of V_{sg} and source-drain voltage V_{34} . **a**, Device F ($\Delta R/2 = 20$ k Ω) requires a back gate voltage $V_{bg} = -5.6$ V to pinch off the device since V_{sg} has limited tunability due to leakage at high absolute values. **b**, Device G ($\Delta R/2 = 110$ k Ω) shows similar properties to device A. **c**, Device H ($\Delta R/2 = 305$ k Ω) shows no conductance diamonds.

3.2.2 Impact of Barrier Height on Transport

The barrier resistance ΔR is a good indicator of the tunnel barrier width and strongly influences the low-temperature transport properties. Figure 14 shows transport characteristics of three 500 nm QD devices (devices F, G and H). The device designs are similar to that of device A, but with a shorter distance of 500 nm between the two barriers. The only difference among devices F, G and H is the single barrier resistance $\Delta R/2$, with $\Delta R/2 = 20, 110$ and 305 k Ω respectively. The resulting difference in transport is clear. Device F shows the most conductance diamonds for the smallest barrier resistance (superconductivity is suppressed in this device after applying a $V_{bg} = -5.6$ V), while device H, with the largest barrier resistance, is virtually featureless. Conductance diamonds and superconductivity-related phenomena in dI/dV of device G have V_{sg} -dependence that is very similar to that of device A. Since the single barrier tunneling rate decays exponentially with the barrier width, the differences in transport of devices F, G and H can be understood as a result of suppressed quantum tunneling rates under the assumption that the two barriers are slightly asymmetric.

3.3 EXPERIMENTS AND RESULTS

3.3.1 Transport at B=0 T

The low-temperature ($T = 50$ mK) differential conductance (dI/dV) versus side-gate voltage (V_{sg}) measurements for the nanowire QD and open wire show contrasting transport characteristics (device A, Fig. 12(b), (c)). While the open wire (Fig. 12(b)) exhibits superconductivity [77] at all V_{sg} values shown, the QD (Fig. 12(c)) exhibits a sequence of diamond-shaped insulating regions for $V_{sg} < -10$ mV. Figure 15 explores the transport behavior of the QD in more detail. The conductance increases by several orders of magnitude only when an available state in the QD is aligned within $k_B T$ of either the source or the drain chemical potential; this condition defines the diamond-shaped insulating regions in Fig. 15(b). Within the diamonds, conductance through the QD is highly suppressed ($dI/dV < 10^{-2} e^2/h$), as

observed between the conductance peaks in the zero-bias ($V_{34} = 0$ V) line cut in Fig. 15(a) at low V_{sg} , and at $V_{34} = 0$ V in Fig. 15(c). Resonant supercurrent is occasionally observed between insulating regions, e.g. at $V_{sg} = -25$ mV (Fig. 15(d)). In the regime $V_{sg} > 0$ mV, where the barriers are highly transparent, supercurrent recovers through the QD (Fig. 15(e)).

3.3.2 Transport at Finite Magnetic Field

Figure 16(a)-(e) shows how the conductance diamonds evolve as a function of an applied out-of-plane magnetic field B . At $B = 0$ T, two zero-bias peaks (ZBPs) are visible, with some narrowing of the lineshape taking place at $B = 1$ T. The diamond pattern remains relatively unchanged at $B = 2$ T, though the size of the diamond is slightly reduced. At $B = 3$ T, new diamonds emerge and separate as the magnetic field is increased further to $B = 4$ T. A high-resolution scan of the conductance versus gate voltage at zero bias (Fig. 16(f)) enables the ZBP to be fitted and tracked versus magnetic field. A global shear of all of the ZBP splittings above B_p is observed and offset in Fig. 16(f) (see Fig. 17 and § 3.3.2.1). This shear, which appears in 60% of the total devices and is possibly attributable to orbital effects [76], does not influence the analysis of B_p (§ 3.3.2.2).

The ZBP at $V_{sg} = -27$ mV splits above a critical magnetic field $B_p = 1.8 \pm 0.1$ T (Fig. 16(f)), corresponding to the emergence of new diamonds (Fig. 16(a-e)). The critical magnetic field at which this occurs is one order of magnitude larger than the upper critical field for superconductivity $\mu_0 H_{c2} \approx 0.2$ T. The ZBPs at $V_{sg} = -19$ mV and $V_{sg} = -17$ mV have successively smaller values for B_p and show pronounced superconducting resonances below $|B| < 0.2$ T (indicated by the red arrow in Fig. 16(f)). For $|B| > B_p$, the energy difference between the split peaks increases Zeeman-like with magnetic field: $E_Z = g\mu_B(B - B_p)$. The Landé g-factor $g = 1.2 \pm 0.1$ (Fig. 16(g)) is calculated from the slope by taking into account the experimentally determined coupling factor $\alpha = 0.10 \pm 0.01$ eV V⁻¹ (§ 3.4.1.1). At much larger magnetic fields the Zeeman-split ZBPs occasionally intersect and lock together (re-entrant pairing) before separating again (for example, at $V_{sg} = -25$ mV). The energy associated with B_p , $E_p = g\mu_B B_p$, ranges between 100 μ eV and 900 μ eV for the four devices shown here (Fig. 16(h)) and decreases non-monotonically with increasing V_{sg} for each device.

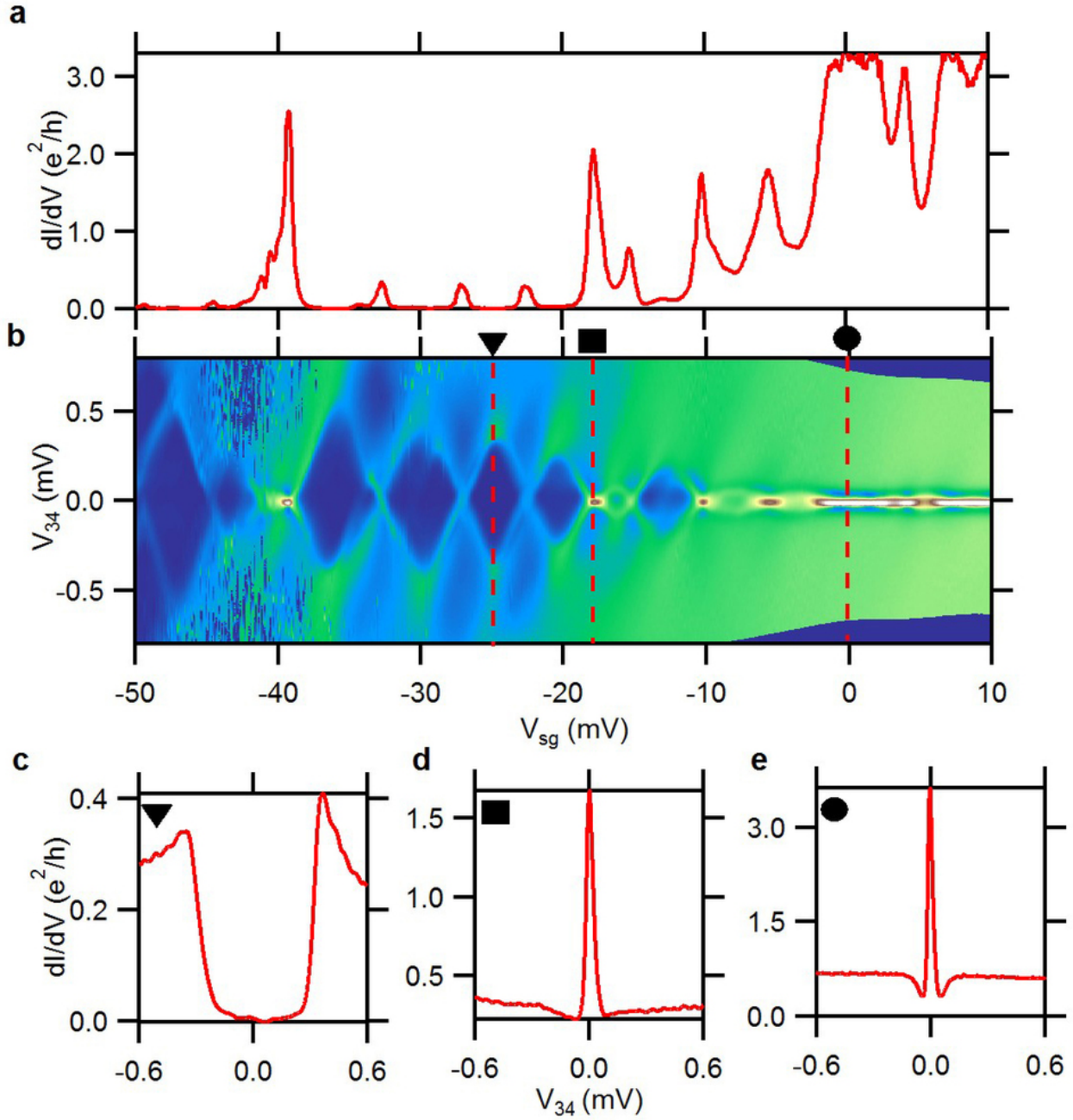


Figure 15: Transport characteristics of device A. **a**, Zero-bias line cut of the dI/dV map in **b**; filled black symbols show positions of line cuts displayed in **c-e**. **b**, dI/dV versus V_{34} and V_{sg} . **c—e**, Full suppression of transport in device A at $V_{sg} = -25$ mV (**c**), resonant tunneling transport at $V_{sg} = -19$ mV (**d**), and fully superconducting transport at $V_{sg} = 0$ mV (**e**).

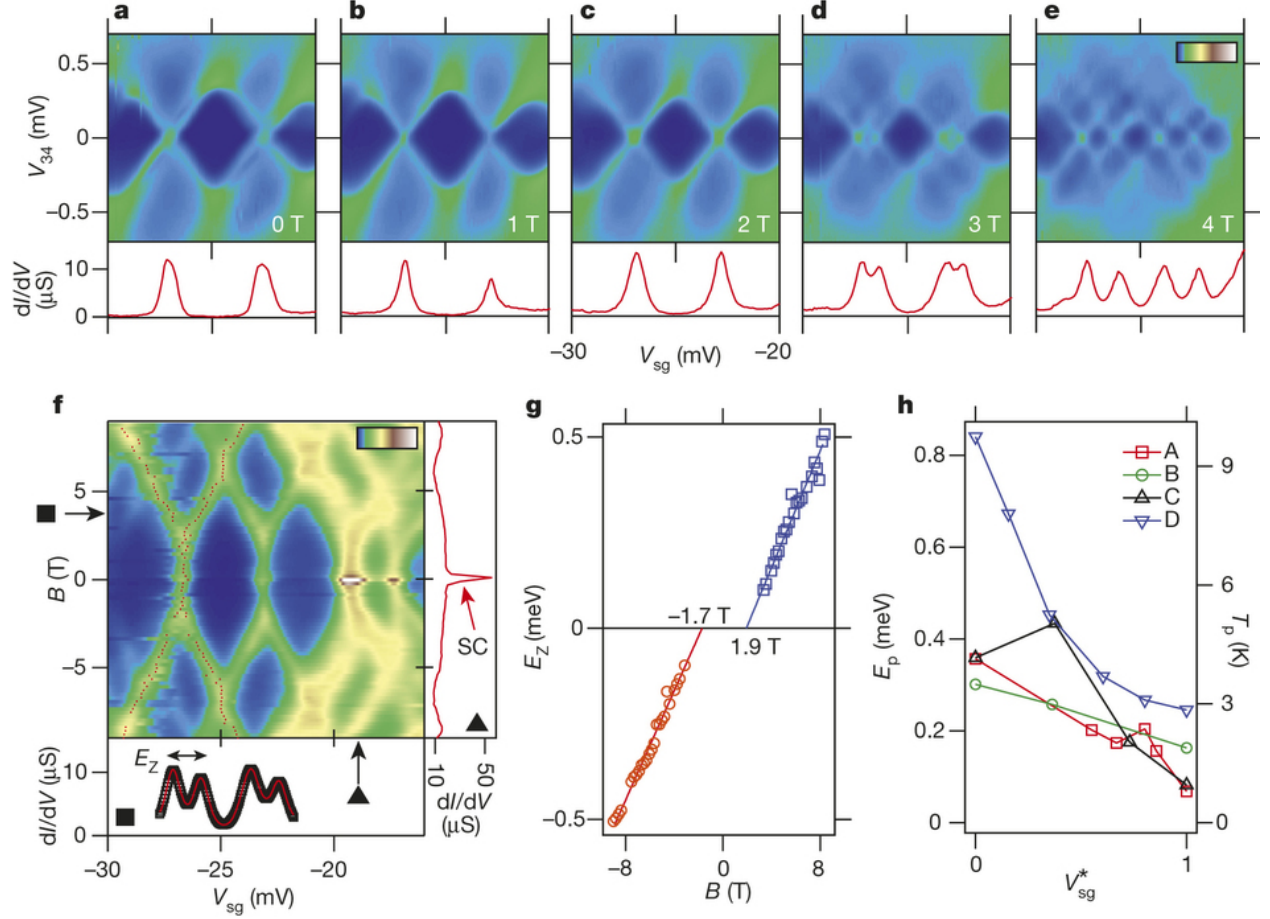


Figure 16: Out-of-plane magnetic field dependence of device A at $T = 50$ mK. **a—e**, Top panels, dI/dV dependence on V_{34} and V_{sg} at $B = 0 - 4$ T. New diamonds emerge at $B = 3$ T in **d**. Color scale (top right), $0 - 80 \mu\text{S}$. Bottom panels, zero-bias line profiles in **a—e**. **f**, Top panel, magnetic field dependence of ZBPs. All the ZBPs split above some critical fields, B_p . Color scale, $0 - 40 \mu\text{S}$. Bottom panel, line profile (black markers) of ZBP at $B = 3.8$ T in the top panel, indicated by the horizontal black arrow. Red line is the fit to extract peak locations (see Methods). Right panel, line profile at $V_{sg} = -19$ mV indicated by the vertical black arrow. The sharp peak at $B = 0$ T is due to superconductivity (SC). **g**, Energy difference E_Z of two Zeeman splitting branches of the ZBP at $V_{sg} = -27$ mV. B_p and g factor can be extracted from the intercepts and slopes in the linear fits. **h**, E_p dependence on rescaled V_{sg}^* for all available ZBP splittings in four devices A, B, C and D, where $V_{sg}^* = (V_{sg} - V_{sg}^{min}) / (V_{sg}^{max} - V_{sg}^{min})$, and V_{sg}^{max} and V_{sg}^{min} are maximum and minimum ZBP locations of each device. E_p roughly decreases with increasing V_{sg} .

3.3.2.1 Universal Shift with Magnetic Field Below B_p , the ZBPs are generally insensitive to magnetic fields. Above B_p , the centers of the ZBP splittings move nonlinearly with magnetic fields, as shown in the red trace $V_{sg}(B)$ in Fig. 17(a). This movement, possibly arising from the orbital effect, is only observed in a fraction of devices. A similar effect has been reported in ref. [78]. This is corrected (Fig 17(b)) by offsetting the magnetically induced global shift to keep the centers of ZBP splittings relatively constant, that is, $V_{sg}(B) = V_{sg0}(B) - \delta V_{sg}(B)$. This shift procedure does not influence the analysis of B_p , nor does it change the relative spacing between splittings. A waterfall plot (Fig. 18) of Fig. 16(f) is included to provide clear line cuts of the ZBPs at all fields.

3.3.2.2 Analysis of B_p Above the pairing field B_p , single electron tunneling occurs and standard Coulomb blockade physics analysis applies. Closely spaced Coulomb blockade ZBPs can be fitted to a multi-peak hyperbolic cosine expression [79]

$$dI/dV = G_0 + \sum_i A_i \cosh^{-2}[B_i(V_{sg} - V_{sg}^i)] \quad (3.1)$$

where G_0 , A_i and B_i are constants. Equation 3.1 is used to examine two peaks that have split from a single ZBP at low magnetic fields in order to extract the i th peak location as a function of field ($V_{sg}^i(B)$ indicated in the red trace in the main panel of Fig. 16(f)). This fit was performed for multiple pairs of split peaks in many devices. The energy difference of the split peaks, $E_Z(B) = \alpha(V_{sg}^2(B) - V_{sg}^1(B))$, where α is the coupling factor as described in § 3.4.1.1, can be fitted to a straight line as in Fig. 16(g). The slope of this fit gives the Landé g-factor according to $E_Z = g\mu_B(B - B_p)$, where the Zeeman energy difference is offset by the pairing energy $E_p = g\mu_B B_p$. As mentioned in § 3.3.2.1, ‘straightening’ the magnetically induced global shift to keep the centers of ZBP splittings relatively constant does not disturb this analysis. Both peak positions $V_{sg}^1(B)$ and $V_{sg}^2(B)$ have the same offset at each field, so $E_Z(B)$, from which g and B_p are calculated, remains unaffected.

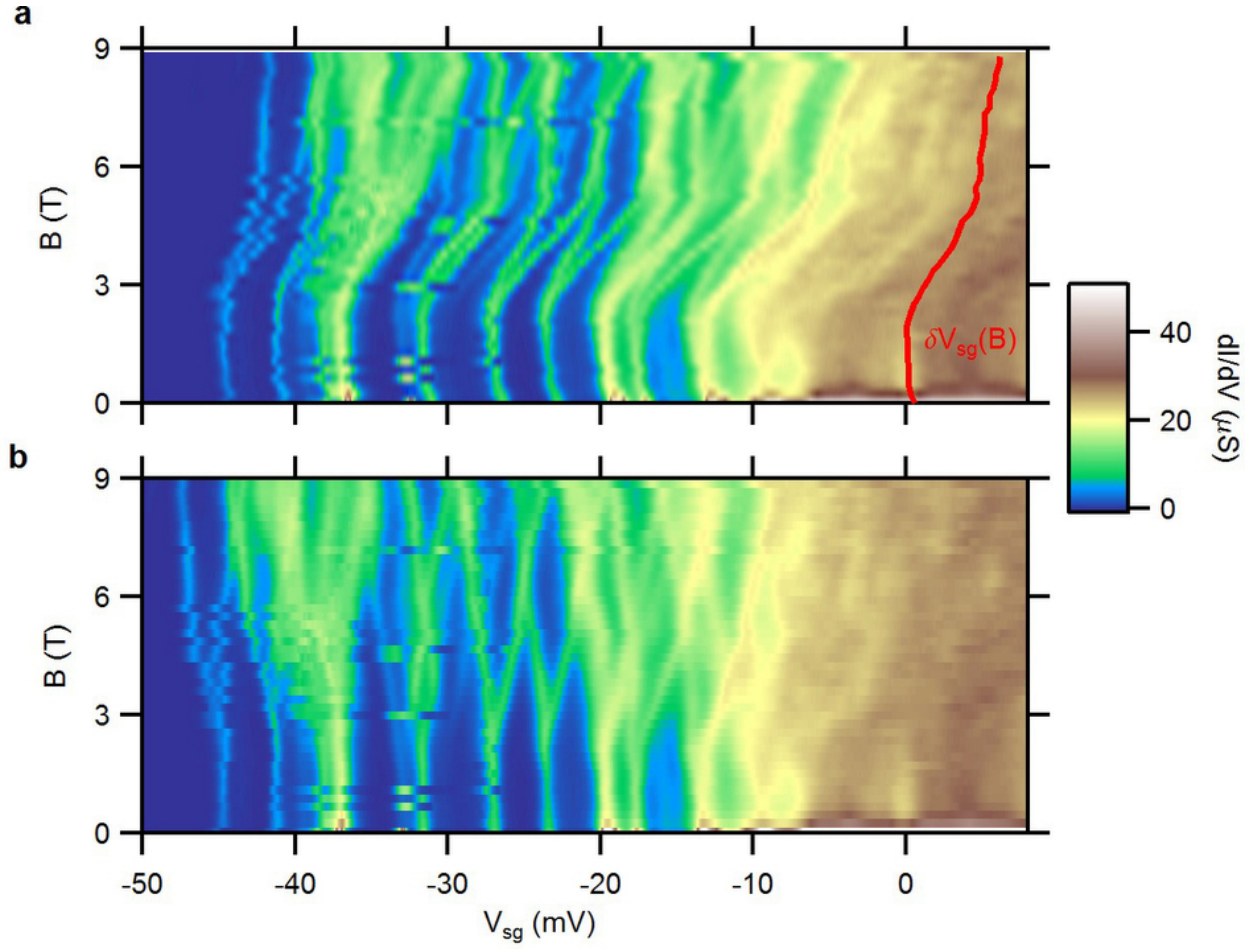


Figure 17: Global shift correction of data from device A. **a**, Original data for Figs 16(f) and 22(a). The global shift is illustrated by the red trace, $V_{sg}(B)$. **b**, Data shown in Figs 16(f) and 22(a) are corrected by $V_{sg}(B) = V_{sg0}(B) - \delta V_{sg}(B)$.

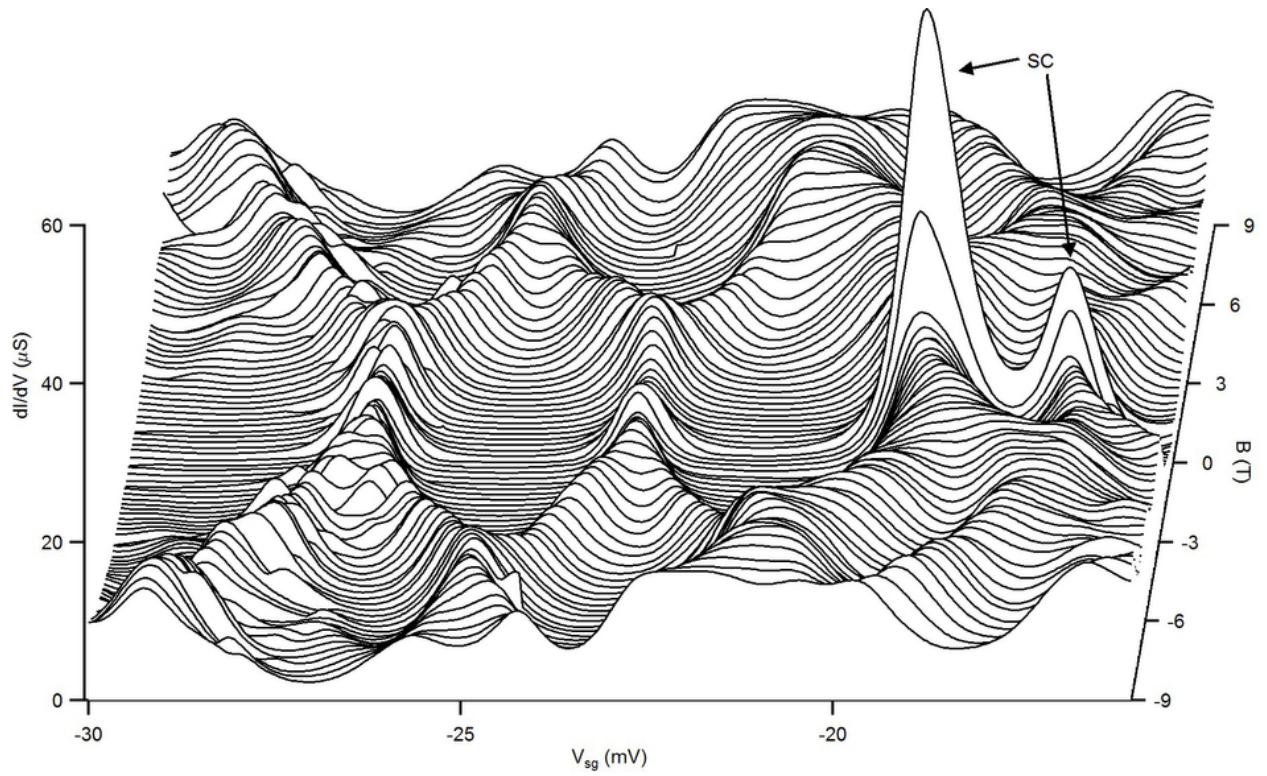


Figure 18: Waterfall plot of Fig. 16(f). Plot shows lock-in dI/dV data at small ($100 \mu\text{V}$) bias as a function of V_{sg} , taken as the magnetic field is slowly swept from -9 T to 9 T.

3.3.3 Temperature Dependence

Temperature-dependent transport measurements (Fig. 19) show B_p to be nearly independent of temperature up to the highest value measured ($T = 900$ mK). Of four devices, only device B, which shows the lowest B_p , exhibits a threefold suppression at $T = 900$ mK. Figure 19(a) shows a representative conductance map versus V_{sg} and B acquired at $T = 100$ mK. The conductance at $B = 6$ T shows two well-resolved split peaks at $T = 100$ mK. As the temperature is increased while the magnetic field is held constant at $B = 6$ T, the side-gate splitting between the two peaks ΔV_{sg} increases, shown in Fig. 19(c). Assuming that the g-factor is constant over this temperature range, this result implies that $dB_p/dT < 0$, which is also consistent with the fitting result summarized in Fig. 19(d).

3.4 DISCUSSION

3.4.1 Pair Tunneling and Resonant Superconductivity

The quantum transport behavior of LaAlO₃/SrTiO₃ nanowire QDs contrasts sharply with conventional Coulomb blockade behavior in other semiconductor nanostructures [80]. Generally, the ‘addition energy’ (the difference of chemical potentials μ_N and μ_{N+1}) required to change the charge state of a QD from N to $N + 1$ electrons is the sum of both the classical charging energy E_c and the orbital energy δE of the device: $E_{add}(N) = E_c(N) + \delta E(N)$. For QD systems involving semiconductors, carbon nanotubes or superconductors [80], E_{add} is usually dominated by E_c , resulting in regularly spaced Coulomb diamonds. In device A, E_{add} decreases (non-monotonically) from 640 μeV (at $V_{sg} = -47$ mV) to 210 μeV (at $V_{sg} = -13$ mV). The level spacing is non-uniform, signifying that orbital contributions dominate the addition energy. Resonant supercurrent flowing through the QD is observed when the addition energy E_{add} falls below the superconducting gap [3] $\Delta \approx 40 \mu\text{eV}$ (for example, at $V_{sg} = -39$ mV and -19 mV), consistent with Andersons criterion for nanoscale superconductivity ($\delta E < \Delta$) [81].

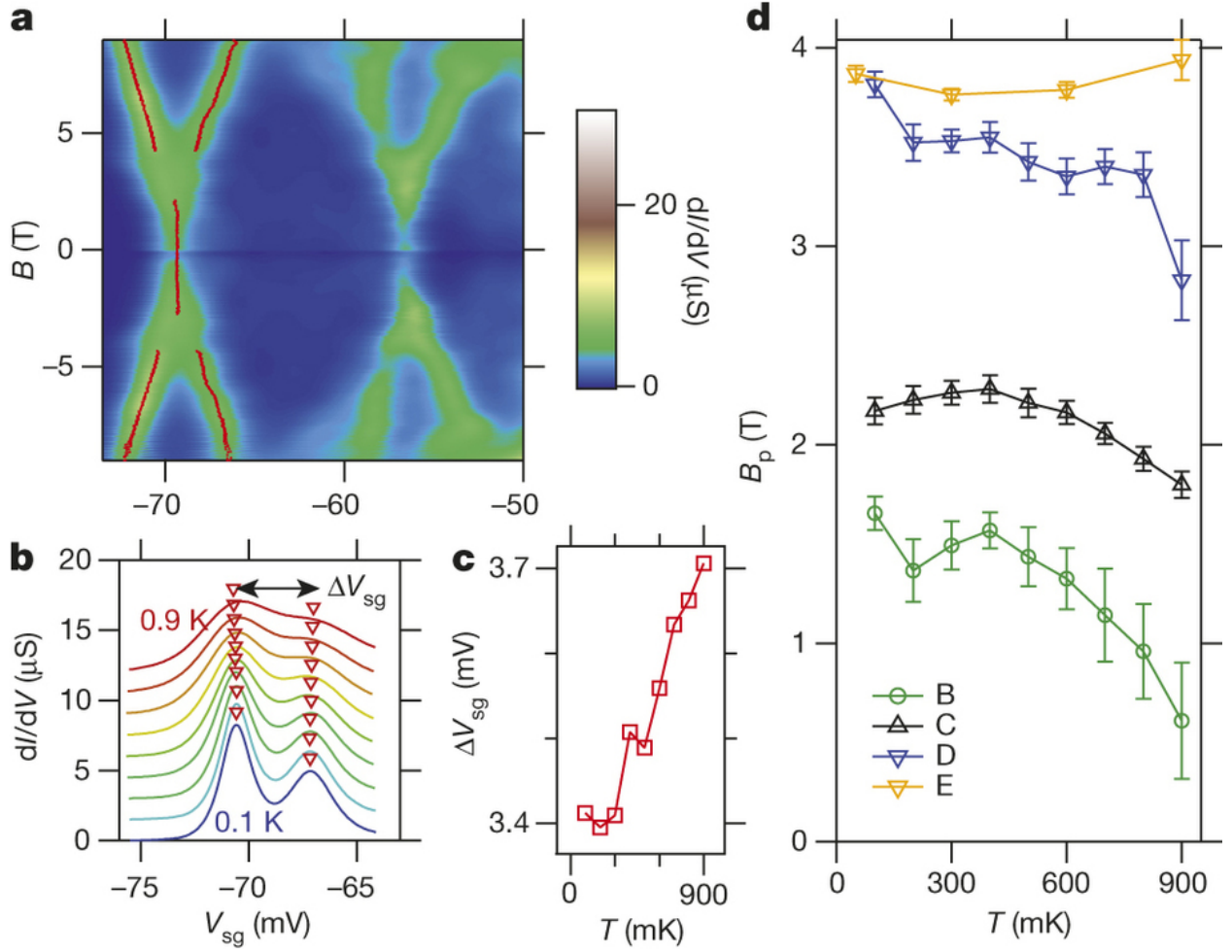


Figure 19: Temperature dependence of B_p . **a**, Out-of-plane field dependence of ZBPs from device B at $T = 100$ mK. Trace of red dots reveals the actual peak locations extracted by fitting. **b**, Line profiles at $B = 6$ T of different temperatures from 100 mK (blue) to 900 mK (red) with 100 mK spacing. Red triangles mark actual peak positions. Curves are offset for clarity. **c**, V_{sg} difference ΔV_{sg} between two splitting branches in (b) as a function of temperature. A larger ΔV_{sg} at higher temperatures indicates lower B_p . **d**, Temperature dependence of B_p for the most isolated ZBP splittings in four devices B, C, D and E. B_p in device B, which is the lowest among the four devices, decreases non-monotonically with increasing temperature. Error bars, s.e.m. from the linear fitting errors of the positive and negative critical magnetic fields.

Experiments in Al-based superconducting SETs report pair tunneling only in the superconducting state, and in the pair-tunneling condition $E_c < 2\Delta$ when the pairing energy dominates over the Coulomb charging energy [76]. The high permittivity of SrTiO₃ leads to a significant reduction of the charging energy for LaAlO₃/SrTiO₃ nanowire SSETs, enabling them to operate in the pair-tunneling regime (see §§ 3.4.1.1 and 3.4.1.2 for estimates and analysis). The observed ZBP splitting indicates that electron pairing is the preferred ground state that persists in magnetic fields far larger than $\mu_0 H_{c2}$, above which superconductivity is suppressed.

3.4.1.1 Device Transport Parameters As mentioned previously, bulk SrTiO₃ is an incipient ferroelectric at low temperatures with a divergently large and gate-tunable dielectric constant [19] $\epsilon_r \approx 20,000$. Consequently, estimation of the gate-dot capacitance yields $C_{sg} \approx 100$ fF, using a parallel wire model $C_{sg} = \pi\epsilon_r\epsilon_0 L / \cosh^{-1}[d/2r]$ with vacuum permittivity ϵ_0 , QD length $L = 1 \mu\text{m}$, QD-gate spacing $d = 1 \mu\text{m}$, and nanowire radius $r_{QD} = 5 \text{ nm} =$ side gate radius $r_{sg} = 5 \text{ nm}$. The corresponding charging energy is vanishingly small in the ideal case (that is, zero V_{sg}) $E_c = e^2/C_\Sigma < e^2/C_{sg} = 2 \mu\text{eV}$, where C_Σ is the total capacitance of the QD. The actual E_c could be larger since ϵ_r is expected to be reduced by electric field and strain effects at the interface.

For a nanowire with length $L = 1 \mu\text{m}$ and width $w = 5 \text{ nm}$, the number of carriers can be estimated as $N = n_s L w = 500$ by using a typical two-dimensional LaAlO₃/SrTiO₃ carrier density $n_s \approx 10^{13} \text{ cm}^{-2}$. The mean level spacing between spin-degenerate levels can be estimated by using a ‘particle in a one-dimensional box’ model and effective mass [82] $m^* = 0.7m_e$. This gives $\delta E = \frac{\partial E}{\partial N} = \frac{\pi^2 N \hbar^2}{m^* L^2} \approx 500 \mu\text{eV}$, which is consistent with the values of E_{add} . As one can see, the addition energy is dominated by orbital level spacing δE .

The ability of the side gate to tune the chemical potential of the device is characterized by $\alpha = C_{sg}/C_\Sigma$. The coupling factor can be calculated using the slopes β and γ which define the diamonds in the dI/dV map, $1/\alpha = 1/\beta + 1/\gamma$. Coupling factors vary from $\alpha \approx 0.03 - 0.13 \text{ eV/V}$, with a typical $\alpha \approx 0.10 \text{ eV/V}$. For all devices, the coupling factor is observed to decrease at high V_{sg} values; this variation is reflected in Table 1.

Table 1: Parameters of eight SSET devices. All devices have a schematic similar to that of device A but with different control (open) wire length L_w , distance between two barriers L_b , single barrier resistance $\Delta R/2$, and range of side gate coupling factor α for all the diamonds.

Device Name	L_w (μm)	L_{QD} (μm)	$\Delta R/2$	Coupling Factor Range (eV/V)
A	2.5	1	32	0.08-0.13
B	2.5	1	30	0.06-0.11
C	2.5	1	15	0.04-0.10
D	2.5	1	15	0.04-0.10
E	2.5	1	25	0.03-0.06
F	2	0.5	20	0.03-0.06
G	2	0.5	110	0.06-0.12
H	2	0.5	305	0.07-0.09

3.4.1.2 Constant Interaction Model The constant interaction model is widely used to analyze QD transport characteristics through two independent variables: Coulomb interactions and single-particle energy levels [80]. Here, superconductivity is combined with the constant interaction model and the analysis from ref. [83] is extended by including non-zero orbital level spacing. In a QD with N electrons, the excess charge has two parts: the integer part $n = N - N_0$ and a continuous part $C_{sg}V_{sg}/e$ representing electrostatic charge induced by the gate, where N_0 is the charge at zero gate voltage. The system ground state energy $E(N)$ can be written as

$$E(N) = \sum_{i=1}^N E_i + E_c(n - V_{sg}\alpha e/E_c)^2/2 + p\delta_p \quad (3.2)$$

where E_i are single-particle energy levels, p is a parity factor with $p = 0(1)$ for even (odd) N and δ_p is parity energy. The first term in equation 3.2 is the electrochemical contribution determined by quantum confinement, the second term is electrostatic part induced by V_{sg} and the third term is the extra energy $p = (E(N_{odd}) - (E(N_{odd} + 1) + E(N_{odd} - 1)))/2$ which the

odd electron has to pay to enter the QD. The addition energy E_{add} , which is the difference (of chemical potential μ) of a difference (of total energy E), is directly measured in the tunneling spectroscopy measurement. Namely, the chemical potential is

$$\mu(N) = E(N) - E(N - 1) = E_N + E_c(n - 1/2) - e\alpha V_{sg} + \beta\delta_p \quad (3.3)$$

where $\beta = -1(1)$ for even (odd) number of electrons (N). E_{add} can subsequently be written as

$$E_{add} = \mu(N + 1) - \mu(N) = E_c + \delta E(N) + \gamma\delta_p \quad (3.4)$$

where $\gamma = 2(-2)$ for even (odd) number of electrons. Interestingly, $E_{add} = E_c - 2\delta_p$ can be negative in the odd case ($\delta E(N_{odd}) = 0$) if $E_c < 2\delta_p$, suggesting this unpaired electron is not stable and wants to pair with a partner. In a BCS superconductor, the parity energy is approximately the gap energy ($\delta_p \approx \Delta$) in the limit of small level spacing $\delta E(N)$ compared to the superconducting gap Δ ($\delta E < \Delta$). In the opposite extreme limit $\delta E \gg \Delta$, δ_p can be enhanced such that $\delta_p = \delta E / 2 \ln(\delta E / \Delta)$ due to quantum fluctuations [84]. Either way it is reasonable to assume $E_c < 2\delta_p$ based on the estimate of E_c , suggesting pair tunneling is the preferred transport mechanism in the devices explored here. Note in the case of pairing without superconductivity, the parity energy δ_p should be replaced by the pair binding energy Δ_b in equations 3.2-3.4. When the temperature and magnetic field are increased, δ_p and Δ_b are suppressed to zero at the same B_p where the Zeeman splitting of the peaks occurs.

3.4.2 Attractive Hubbard Model

Electron pairing without superconductivity can be described by a phenomenological Fermi-Hubbard model (equation 3.5) with an attractive on-site potential $U < 0$ [85]. The QD is represented by a one-dimensional chain of local pairing sites that can be occupied with zero, one, or two electrons. For sufficiently attractive $U < 0$, electrons will bind into pairs. This is the regime of the parity effect: in zero external field, the ground state as a function of gate voltage (represented by the chemical potential in equation 3.5) will always contain an even number of electrons. The external magnetic field B favors polarized states, breaking the pairs. For magnetic fields greater than a critical field $B > B_p$, ground states with odd

electron numbers can be stabilized. The interaction between pairs causes the critical field to decrease monotonically with increasing filling (increasing chemical potential or gate voltage). The Hamiltonian is written as:

$$H = -t \sum_{i,\sigma} (c_{i+1,\sigma}^+ c_{i,\sigma} + c_{i,\sigma}^+ c_{i+1,\sigma}) + U \sum_i n_{i\uparrow} n_{i\downarrow} + g\mu_B B \sum_i S_i^z - \mu \sum_{i,\sigma} n_{i,\sigma} \quad (3.5)$$

where $c_{i,\sigma}^+$ and $c_{i,\sigma}$, are creation and annihilation operators for electrons on site i with spin $\sigma = \uparrow, \downarrow$; the kinetic parameter $t > 0$ quantifies the effective hopping between adjacent pairing sites; $n_{i,\sigma} = c_{i,\sigma}^+ c_{i,\sigma}$ is the number operator; $S_i^z = (1/2)(n_{i,\uparrow} - n_{i,\downarrow})$ is the spin operator; $U < 0$ represents the on-site attractive interaction strength; B is the applied magnetic field; and μ is the chemical potential.

Here, the Hubbard model is solved on an infinite chain with zero, one and two electrons. The Bethe ansatz may be used to solve the model for arbitrary filling, but it is much more complicated than the approach presented here [86]. For zero and one electrons, the energies are simply given by:

$$E_0 = 0 \quad (3.6)$$

$$E_1 = -2t - \frac{1}{2}g\mu_B B - \mu \quad (3.7)$$

Only the low-field two-electron ground state, which is a spin singlet [87, 88], is considered for this analysis. The triplet will be the ground state at higher fields for two electrons. The ground state has zero momentum, so the wavefunction depends only on the separation between the electrons and must behave exponentially. Thus the non-normalized wavefunction is

$$\phi(i, j) = e^{-\zeta|i-j|} \quad (3.8)$$

for electrons on sites i and j . For $i \neq j$, Schrodingers equation gives

$$E_2 = -2t(e^{-\zeta} + e^{\zeta}) - 2\mu \quad (3.9)$$

while for $i = j$ it gives:

$$E_2 = U - 4te^{-\zeta} - 2\mu. \quad (3.10)$$

Combining equations (9) and (10) yields

$$\zeta = \log \frac{-U + \sqrt{16t^2 + U^2}}{4t}, \quad (3.11)$$

$$E_2 = -\sqrt{16t^2 + U^2} - 2\mu. \quad (3.12)$$

Thus the binding energy for an electron pair is

$$\Delta_b = 2E_1 - E_2 = \sqrt{16t^2 + U^2} - 4t - g\mu_B B \quad (3.13)$$

and the ‘size’ of the pair is simply $1/\zeta$. The boundary between the phases with 0 and 1 electrons is given by:

$$B_{0,1} = -\frac{4t + 2\mu}{g\mu_B}. \quad (3.14)$$

The boundary between the phases with 1 and 2 electrons is given by

$$B_{1,2} = -\frac{-4t + 2\sqrt{16t^2 + U^2} + 2\mu}{g\mu_B} \quad (3.15)$$

and the boundary between the phases with 0 and 2 electrons is independent of B :

$$\mu_{0,2} = -\frac{1}{2}\sqrt{16t^2 + U^2}. \quad (3.16)$$

The plot of these three boundaries will have the shape of the letter Y. The three boundaries meet at a critical point given by:

$$\mu_p = -\frac{1}{2}\sqrt{16t^2 + U^2}, \quad (3.17)$$

$$B_p = \frac{-4t + \sqrt{16t^2 + U^2}}{g\mu_B}. \quad (3.18)$$

To expand the discussion, the lowest eigenvalues of the Hubbard Hamiltonian (equation 3.5) are solved on a 16-site chain using the iterative Lanczos algorithm, which is particularly efficient for sparse matrices [89, 90, 91, 92]. The full Hilbert space has 4^{16} states, which are split into smaller subspaces using the total electron number, $N_e = \sum_{i,\sigma} n_{i,\sigma}$, the total z -component of spin, $S^z = \sum_i S_i^z$, and the mirror symmetry of the system. The total spin is an additional symmetry of the Hamiltonian which is not exploited. The largest subspace contains 82,820,900 states.

Figure 20(a) shows the energy of the ground state for $N_e \leq 16$ in zero applied magnetic field. The lowest-energy state has total $S^z = 0$ for N_e even and $S^z = 1/2$ for N_e odd. The ground state always has an even number of electrons, which can be seen by shifting all the energies by a suitable function of μ , chosen here as quadratic. This does not change their relative order but can make the energy differences easier to visualize. In Fig. 20(b), the parity effect is apparent: the ground state always contains an even number of electrons.

Increasing the magnetic field reduces the energy of the higher spin states relative to the $S = 0$ ground states at $B = 0$. The ground state is polarized in the $-z$ direction, so the total spin S is identical to the z -component of spin S^z . The phase diagram as a function of magnetic field and chemical potential μ is shown in Fig. 21. At low magnetic fields, the system consists of electron pairs: N_e is even, and the total spin $S = 0$. At slightly higher fields, it becomes favorable to have a single unpaired electron, resulting in odd N_e and $S = 1/2$. Increasing the field further results in two unpaired electrons. Now N_e is even again, but with total spin $S = 1$. The pattern continues with increasing field—the number of unpaired electrons increases monotonically.

The zero-temperature stability diagram of the 16-site model (Fig. 22(b)) qualitatively captures many of the experimentally observed features: the existence of a critical pairing field B_p , a Zeeman-like splitting for $|B| > B_p$, a decrease of B_p with increasing μ , and re-entrant pairing at higher magnetic fields (Fig. 16(f)). The Hamiltonian (equation 3.5) has no disorder, resulting in the even level spacing seen in Fig. 22(b). Adding some disorder to the Hamiltonian, either in the energy levels of each pairing site or in the kinetic hopping between pairing sites, makes the level spacings less regular, more closely resembling the spacings seen in the experimental ZBPs (Fig. 22(a)). Additionally, the superconducting regime of the

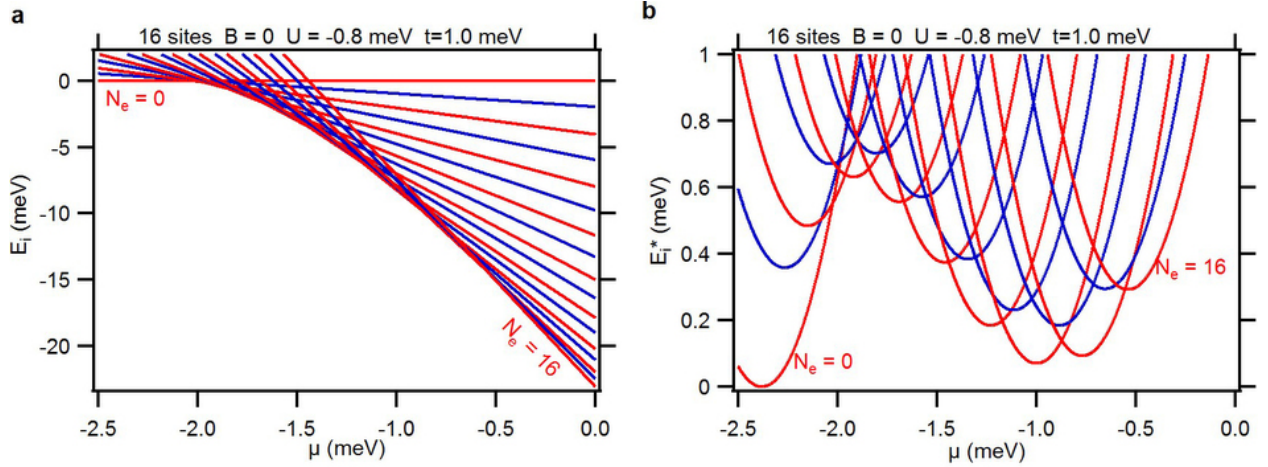


Figure 20: Parity effect. **a**, Energies E_i of the Hubbard model (equation 3.5) of a one-dimensional 16-site chain with open boundary conditions, $t = 1$ meV, $U = 0.8$ meV, and $B = 0$ for fillings $N_e \leq 16$. The slope of each line is proportional to N_e ; red (blue) lines have even (odd) N_e . For all chemical potentials μ , the ground state has even N_e . **b**, Energies of the Hubbard model for the same parameters as a shifted by a quadratic function of μ , $E_i^*(\mu) = E_i(\mu) + c\mu^2$, where c is arbitrary. The lowest energy for each value of μ is easier to discern. The ground state always has even N_e .

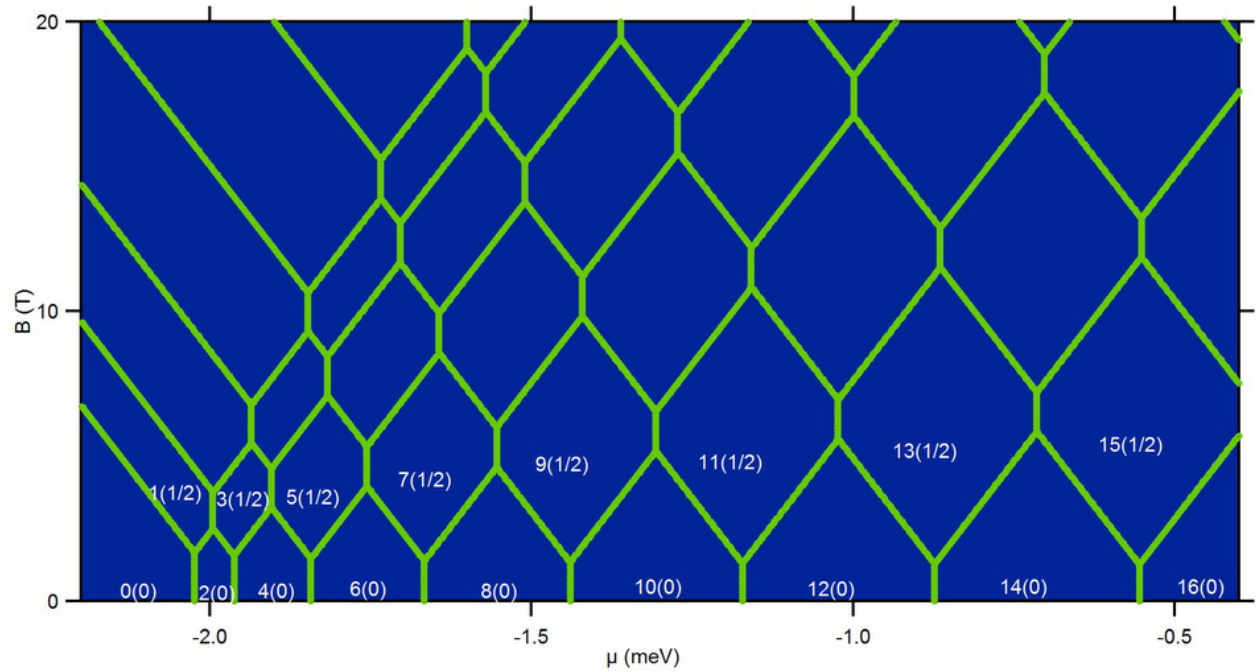


Figure 21: Phase diagram of the Hubbard model on a one-dimensional 16-site chain with $t = 1$ meV and $U = 0.8$ meV. The total number of electrons N_e and total spin S are labeled for some of the larger phases as $N_e(S)$. The quantum numbers of the other phases can be deduced from their neighbors.

attractive Hubbard model is not explored here, but is covered extensively in the literature [93]. Being phenomenological, equation 3.5 does not specify a physical mechanism for the attractive on-site interaction.

3.4.3 Pairing Mechanisms

The attractive Hubbard model does not specify a physical origin of the pairing mechanism. Here we discuss two possible forms of pairing sites: negative-U centers and bipolarons. The negative-U center, which hosts a bounded electron pair, was first proposed in ref. [94] to account for the diamagnetism in amorphous semiconductors. Its existence has been reported in various materials, for example, hydrogenic [95] or oxygen impurities [96] in GaAs. Meanwhile, negative-U centers have been proposed as a pairing mechanism in some unconventional superconductors such as Tl-doped PbTe (refs [97, 98]). In SrTiO₃, negative-U centers can possibly originate from oxygen vacancies (or vacancy clusters) since the lowest threshold carrier density is only observed in vacancy doped samples but not in samples with other n-type dopants (for example, Nb) [99]. Another possible mechanism for local pairing is bipolaron formation. Bipolarons are bound states of two polarons [93], which are self-localized electronic states formed from lattice distortions; for example, via the Jahn-Teller effect [100]. When two polarons meet, they can share the same lattice distortion, lowering the total energy per electron and thus forming a bound state under certain conditions. The existence of polarons in SrTiO₃ has been extensively reported (see, for example, refs [101, 102]). While there is no definitive experimental evidence of bipolaron formation in SrTiO₃, there are reports of bipolarons in other titanites [103]. Such specific mechanisms for strong pairing are not directly implied by the measurements reported here, although some predictions may be testable with suitable refinements of this experimental approach.

3.4.4 Alternative Explanations

Alternative explanations for the ZBP splittings have been considered. The Kondo ridge in Coulomb diamonds can split above a critical magnetic field [104]. However these splittings are generally observed at non-zero biases; furthermore, other Kondo parity signatures [105]

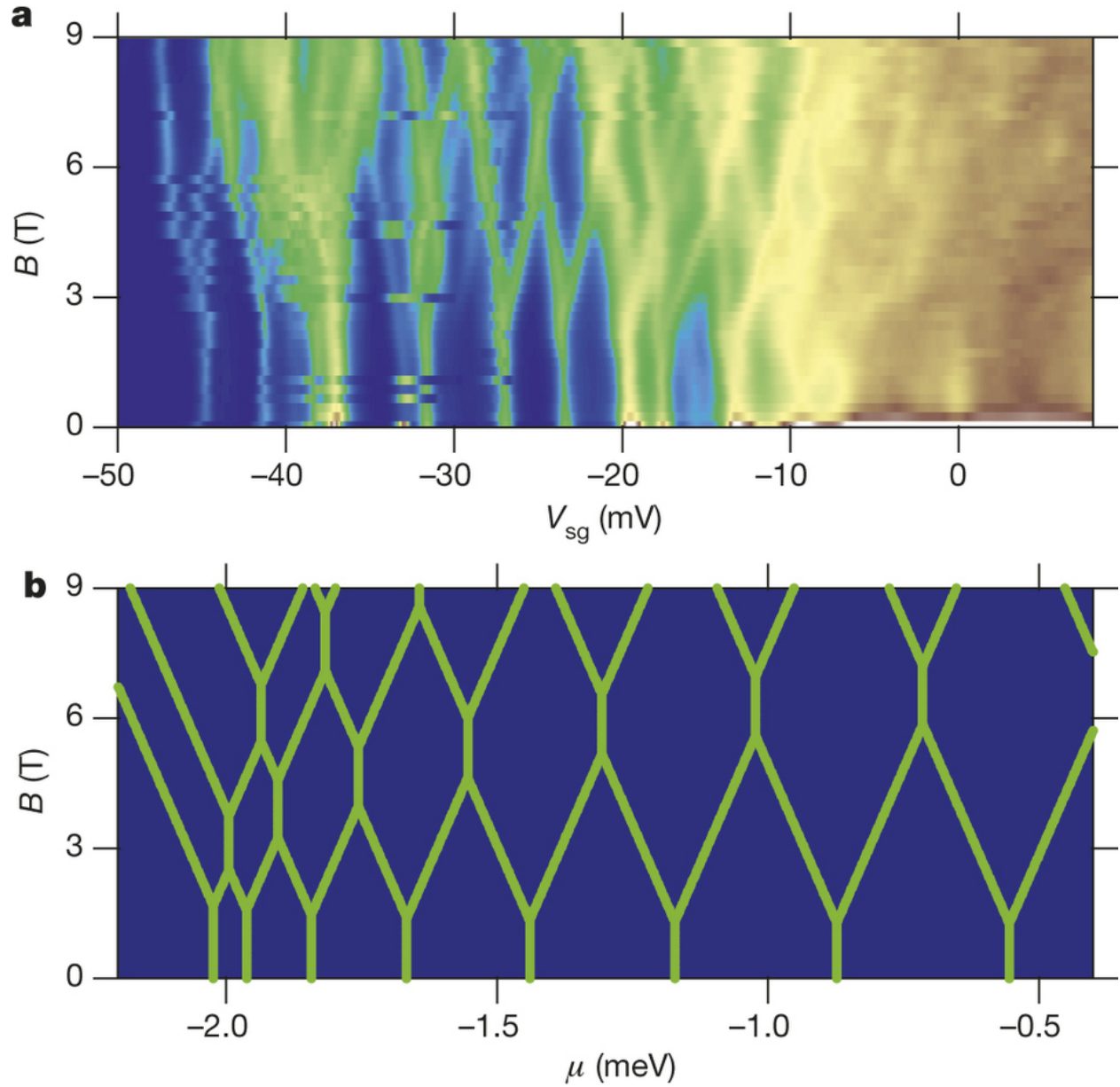


Figure 22: Comparison between experiment and attractive Hubbard model. **a**, Dependence of ZBPs on V_{sg} and B of device A on a larger V_{sg} scale. **b**, Simulation result from the attractive Hubbard model of 16 sites with $t = 1$ meV and $U = 0.8$ meV.

are not observed here. In ultrasmall superconducting grains where $\delta E \gg \Delta$, quantum fluctuations may promote the even-odd parity energy, leading to a possibly similar ZBP splitting [84]. Such an effect, however, is only expected for $T < T_c$.

Charge traps that exist in parallel with tunneling barriers can release additional electrons to the transport [106], resulting in occasional resonance-doubling features. A single-electron charge trap can be modeled with a series of capacitances that reflect the coupling between the trap and the QD, source and drain, as described in ref. [106]. When the trap is in series with the QD, a large source-drain bias is needed to pass through the typically misaligned energy levels of the trap and QD. Namely, the conductance diamonds will have a large gap close to the zero-bias region (in contrast to our observations). When the trap is in parallel with the QD, the contribution to the conductance will be negligible since the coupling between the trap and either source or drain will be very weak due to the small trap size (compared to the 1 μm nanowire QD length). A more realistic scenario is a combination of both the series and parallel coupling. Namely, the trap is in parallel with one of the tunnel barriers and can occasionally release an electron to QD, which is commonly referred as the background or offset charge [107, 108]. The transport signatures of this type of trap are ‘sawtooth’-like diamonds, and abrupt shifts of ZBPs in external magnetic fields. Such features are not present in results reported here. Finally, perturbations of charge traps to the QD only happen occasionally, while the main features reported here are consistently reproduced in more than 50 devices (see Fig. 23 for more examples), and do not fit the statistical profile of charge traps.

3.5 CONCLUSION

The existence of electron pairs outside the superconducting regime does not automatically imply that the electron pairing described here contributes to the superconductivity itself. It would, however, be a remarkable coincidence for the two phenomena to be superimposed without any interrelationship. In fact, electron pairing and superconductivity are demonstrably linked. The vertical linecut in Fig. 16(f) shows a sharp superconducting enhancement

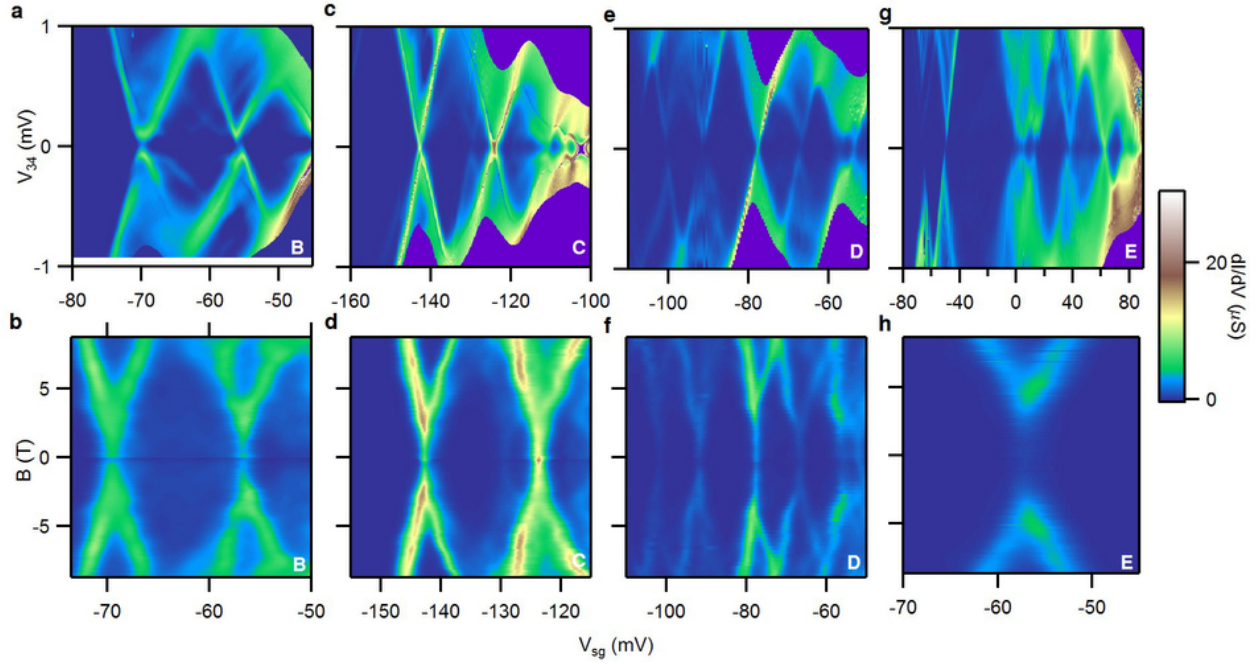


Figure 23: Transport characteristics of devices B, C, D and E, which are all of the same geometry as device A. Device letter is shown at lower right-hand corner of all plots. **a,c,e,g**, dI/dV as a function of V_{sg} and V_{34} at $T = 100$ mK, and $V_{bg} = 0.7$ V, -4.4 V, -1.4 V and -2.2 V for devices B, C, D and E respectively. A small gap close to zero-bias in the diamonds is due to the absence of normal carriers in the superconducting source/drain leads. **b,d,f,h**, Devices B, C, D and E ZBP splitting in an out-of-plane magnetic field B .

of the ZBP at $V_{sg} = -19$ mV. Like the other ZBPs, the paired electron state bifurcates at $B_p \approx 2$ T. This marked enhancement of conductance in the superconducting regime demonstrates that the electron pairs couple strongly to the superconducting leads.

Note that spin-orbit coupling is neglected in this analysis, even though such effects are known to be important in two-dimensional transport experiments [5, 6]. Spin-orbit coupling makes electron pairs less sensitive to magnetic fields and leads to the violation of the Pauli limit in SrTiO₃ ($\mu_0 H_c^P = 1.84T_c \approx 0.5$ T) [5, 109]. However, it is not clear how such coupling will increase the pairing energy above T_c . At the LaAlO₃/SrTiO₃ interface, spin-orbit coupling is known [5, 6] to be strongly dependent on the carrier density n_s . Direct measurements of carrier density are not feasible in the geometry employed here, although the density is believed to increase monotonically with gate voltage.

The existence of pre-formed electron pairs in this SrTiO₃-based system, forming a superconducting condensate at lower temperatures and lower magnetic fields, follows the paradigm of BEC superconductivity. In this regime, pairing is local and precedes the formation of a superconducting state. The only well-established physical embodiments of fermionic BEC-like superfluidity have been in ultracold atomic gases, where the BEC-BCS (Bardeen-Cooper-Schrieffer) crossover can be tuned via a Feshbach resonance [24]. Although it is not clear if the electron pairing in our system can be tuned (for example, via strain), a crossover to BCS-like superconductivity at higher electron density is expected. The ability to confine electrons at nanoscale dimensions, combined with an inherent affinity for strong pairing, suggests that our system constitutes an ideal ‘laboratory’ in which to explore strongly correlated electronic phases in a solid-state host.

4.0 TUNABLE ELECTRON-ELECTRON INTERACTIONS IN LaAlO₃/SrTiO₃ NANOSTRUCTURES

4.1 INTRODUCTION

The contents of this chapter represent a collaborative work published in Cheng, Tomczyk, Tacla, Lee, Lu, Veasey, Huang, Irvin, Ryu, Eom, Daley, Pekker and Levy, *Physical Review X* **6** 041042, 2016 December 1. The conductance calculation in § 4.4.1.1 was performed by A. Tacla. The sub-gap density-of-states calculation in §§ 4.4.1.3 and 4.4.1.4 was performed by D. Pekker.

Electron-electron interactions lead to many remarkable properties in the solid state, ranging from superconductivity and quantum magnetism to fractionalized excitations [110, 111, 112], Wigner crystals [113], and a variety of predicted topological phases [114]. While the natural Coulomb interaction is repulsive, many of these properties rely on effective attractive interactions, which can be mediated by phonons [12] or other degrees of freedom. Although the fine details of electron-electron interactions usually depend on carrier density, qualitative details like the interaction sign are usually density-independent.

While the dome-shaped phase diagram extracted from gate-dependent transport experiments on LaAlO₃/SrTiO₃ marks the boundary of superconductivity, it does not reveal details of the underlying nature of the electron-electron interactions. The non-monotonic dependence of the transition temperature on carrier density bears a striking resemblance to that of high-temperature superconductors. However, while there is experimental and theoretical work suggesting that pairing in cuprates is mediated by repulsive interactions [115, 116], there is no analogous work to describe the superconducting dome in LaAlO₃/SrTiO₃.

The previous chapter studying sketched quantum dot devices revealed a phase in which electrons form pairs, implying a strongly attractive electron-electron interaction. In this chapter, we locally probe local electron-electron interactions at the $\text{LaAlO}_3/\text{SrTiO}_3$ interface using a superconducting single electron transistor (SSET), a sensitive and local probe of single electron/pair tunneling. These devices can exhibit a gate-tunable transition from a pair-tunneling regime with strong electron-electron interactions to a single-electron (Andreev bound state) tunneling regime where the interactions become repulsive. The electron-electron interaction sign change is associated with a Lifshitz transition within the superconducting dome where the d_{xz} and d_{yz} bands start to become occupied. These observations provide crucial constraints that may lead to a fundamental understanding of electron pairing and superconductivity in SrTiO_3 -based systems, as well as providing a novel tool for controlling electron transport in these materials.

4.2 DEVICE GEOMETRY AND FABRICATION

We investigate electron-electron interactions at the $\text{LaAlO}_3/\text{SrTiO}_3$ interface by measuring transport through an SSET. The geometry of an SSET consists of a QD proximity coupled to two superconducting nanowire leads and a side gate. This setup is geometrically similar to the one reported in Ref. [8], but here we investigate higher electron densities on the QD and different gap structures in the leads.

The SSET devices are fabricated by c-AFM lithography [8], as shown in Fig. 24(b) and described in section 3.2. Using a voltage-biased c-AFM tip ($V_{tip} = 12$ V), we first “write” a nanowire network consisting of main channel leads (1 and 5) and three voltage sense leads (2, 3, and 4). The c-AFM tip is then directed to cut across the main channel with a small negative voltage applied ($V_{tip} = -0.3$ V) to engineer two tunnel barriers separated by $1 \mu\text{m}$ and located between leads 3 and 4. The tunnel barriers define the QD, and their strength determines the initial coupling strength to the leads. The nanowire section between leads 2 and 3 has no barriers and serves as a control wire. Finally, a side gate nanowire is written $1 \mu\text{m}$ away from the main channel to tune the chemical potential μ , interaction strength U ,

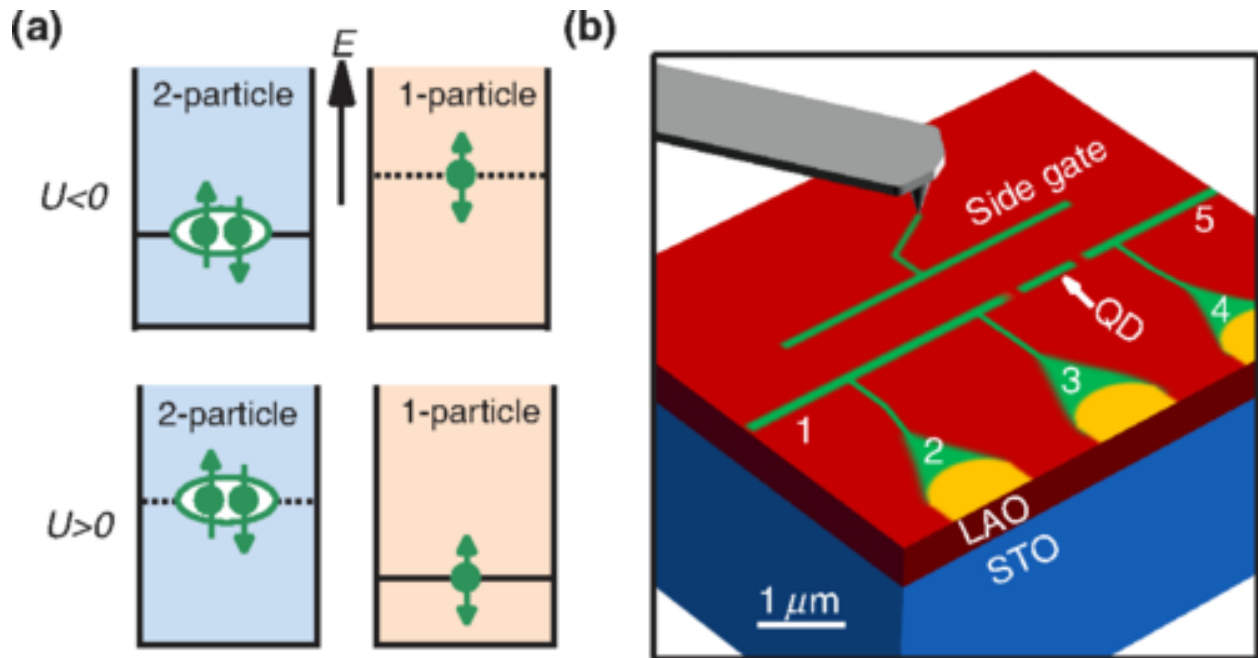


Figure 24: Superconducting single electron transistor (SSET). **a**, The excitation spectra of a QD depends on the sign of the interaction strength U . When $U < 0$ (top two panels), the 2-electron ground state (top left panel) is lower than the 1-electron ground state. When $U > 0$ (bottom two panels), the 1-electron ground state is lowest (bottom right panel). **b**, Electron-electron interactions are probed by an SSET fabricated by *c*-AFM lithography. The nanowire QD is defined by two barriers between leads 3 and 4 separated by $1 \mu\text{m}$. A side gate tunes the chemical potential of the QD.

and tunneling coefficient t . All of the nanowires have width $w \sim 10$ nm at room temperature [71]. The entire setup can be regarded as a superconducting nanowire-QD-nanowire system.

4.3 EXPERIMENTS AND RESULTS

Transport is measured in a four-terminal setup: we extract the differential conductance dI/dV of the QD by passing a current through the main channel and simultaneously measuring the voltage drop between leads 3 and 4. Figure 25(a) shows the differential conductance dI/dV of a typical SSET device as a function of the source-drain bias V_{34} and side gate voltages V_{sg} at low temperatures ($T = 50$ mK) and zero magnetic field ($B = 0$ T). Four distinct transport regimes can be identified in terms of V_{sg} ranges: (i) well-defined conductance diamonds associated with resonant pair tunneling ($V_{sg} < -40$ mV), (ii) sub-gap transport via pair bound states (-40 mV $< V_{sg} < -30$ mV), (iii) sub-gap transport via Andreev bound states (-30 mV $< V_{sg} < -10$ mV) and (iv) Josephson transport ($V_{sg} > -10$ mV).

(i) The well-defined conductance diamonds regime ($V_{sg} < -40$ mV) is qualitatively similar to the transport reported in Chapter 3, in which we have associated the diamonds with resonant tunneling of strongly bound electron pairs. A series of zero-bias conductance peaks (ZBPs) are present near the “tips” of the diamonds as indicated in Fig. 25(a). The ZBPs bifurcate as we increase the magnetic field above a critical value ($B_p \sim 1 - 2$ T), indicating the breaking of strongly bound pairs [Fig. 25(c)]. B_p is typically much larger than the upper critical magnetic field $\mu_0 H_{c2} \sim 0.3$ T for destroying superconductivity [8].

The diamonds have a nearly insulating gap of roughly $4\Delta/e$, where $\Delta \sim 48$ μ eV, in contrast to those observed in Chapter 3 without the insulating gap. This conductance gap, which is determined by the superconducting gap Δ_s in the source lead (as will be discussed later), is only weakly dependent on V_{sg} since the source lead is weakly coupled to the side gate. Moreover, the diamonds are offset horizontally while still being connected by a straight line [see Fig. 25(a)], which (as will be discussed below) indicates that the drain lead has gapless excitations while the source lead remains gapped. Such gapless excitations can arise from nanoscale imperfections (e.g., in carrier density), although the source and drain leads should

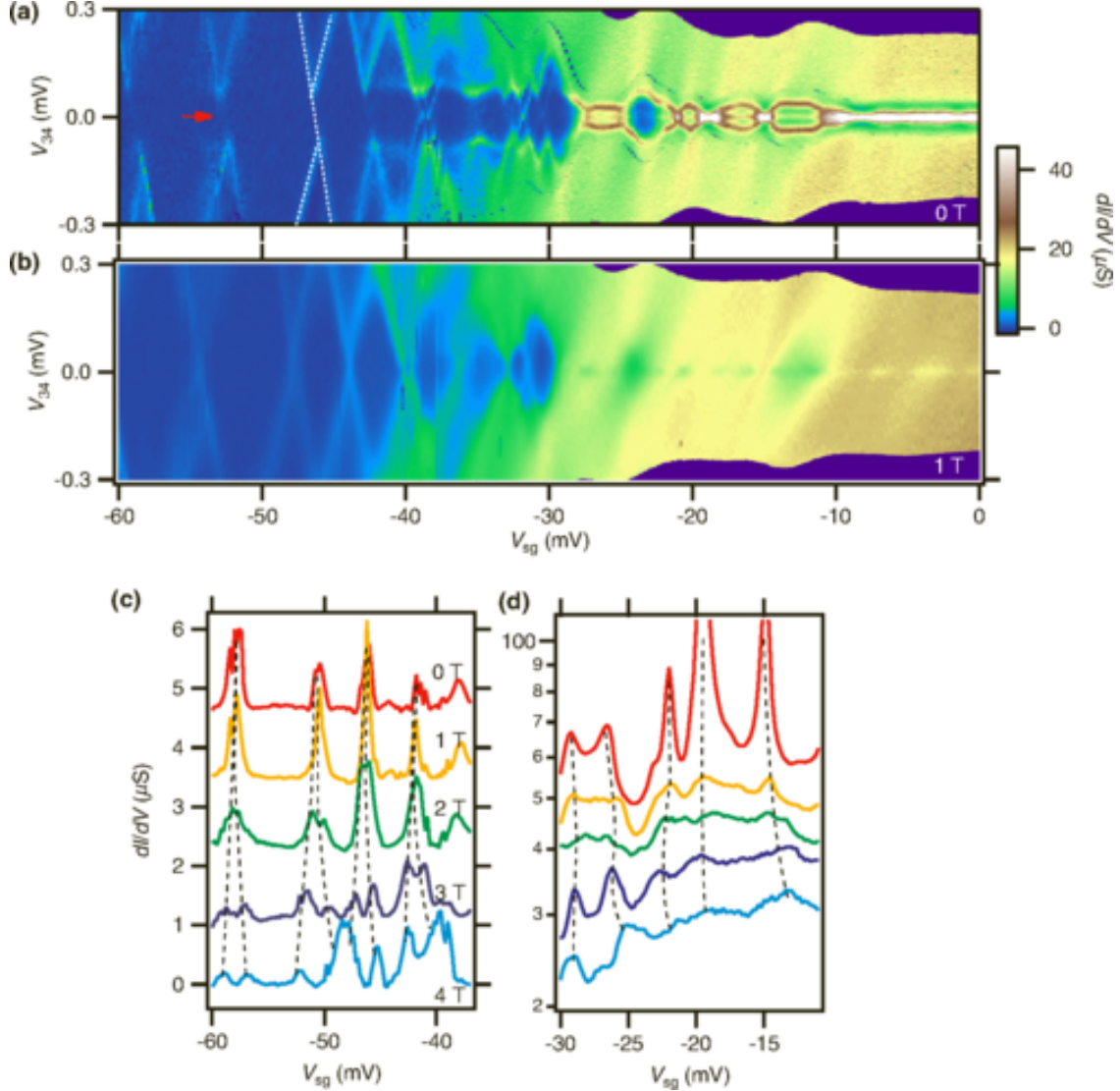


Figure 25: Transport characteristics of an SSET. At $T = 50$ mK, dI/dV is measured as function of V_{34} and V_{sg} at **a**, $B = 0$ T and **b**, $B = 1$ T. The dashed line in (a) is a guide to the eye showing how the diamonds are offset. The fact that the diamonds can be connected by a straight line indicates that one lead has a gap while the other is not gapped. The red arrow indicates the location of zero-bias peak. **c**, Zero-bias line cuts at $B = 0 - 4$ T in low V_{sg} range ($-60 \text{ mV} < V_{sg} < -35 \text{ mV}$). The ZBPs bifurcate above B_c ($1 \sim 2$ T), signifying pair tunneling. Curves are shifted by $1.16 \mu\text{S}$ starting from $B = 4$ T data for clarity. **d**, Zero-bias line cuts at $B = 0 - 4$ T in high V_{sg} range ($-30 \text{ mV} < V_{sg} < -10 \text{ mV}$). The ZBPs do not bifurcate, signifying single electron tunneling. Curves are shifted by $7.75 \mu\text{S}$ starting from $B = 4$ T data for clarity.

be nominally identical. At sufficiently large magnetic fields, the pairing gap and the offset between the diamonds are simultaneously suppressed, see Fig. 25(b). The field (~ 1 T) at which the offset vanishes coincides with B_p for electron pairing, suggesting the source lead is still gapped even when the superconductivity is suppressed above the upper critical field $\mu_0 H_{c2} \sim 0.3$ T.

(ii) The regime of sub-gap transport via pair bound states (-40 mV $< V_{sg} < -30$ mV) is characterized by the appearance of relatively stronger conductance features inside the gap. These “X”-shaped features extend all the way across $4\Delta/e$ gap and appear to be particle-hole symmetric. We ascribe these features to pair bound states on the QD: electron pairs that are in a superposition of being a bound pair on the QD and in the superconducting lead.

(iii) The sub-gap transport via Andreev bound states (ABS) regime (-30 mV $< V_{sg} < -10$ mV) is characterized by a dramatic change of the transport characteristics. The gap shrinks from $4\Delta/e$ to $2\Delta/e$ and at the same time the sub-gap features become much “brighter” (dI/dV increases ~ 10 -fold) as well as changing shapes from characteristic “X” features to “loop” features. We ascribe the dramatic change of the transport to the appearance of Andreev reflections. The absence of features at $V_{34} = 2\Delta/ne$, ($n=1,3,4$) suggests that multiple Andreev reflection processes are irrelevant. Rather, the well-defined smooth loop features are a clear manifestation of transport via ABS.

In the diamond regime and the pair-bound state regime, the lowest excited state of the QD corresponds to adding (or removing, depending on V_{sg}) a *pair* of electrons from the dot. The emergence of ABS loops indicates the lowest excited QD level is characterized by adding (or removing) a *single* electron to the dot, as illustrated in Fig. 24(a). This assignment of the QD excitation structure can be further confirmed by examining the field dependence of the ZBPs. As shown in Fig. 25(d), no signs of ZBP bifurcation are observed up to $B = 4$ T in the ABS regime, except for a decrease in amplitude of the ZBPs due to suppression of superconductivity. In contrast, in the diamond regime the ZBPs bifurcate above $B_p \sim 1 - 2$ T. Since B_p is generally decreasing with increasing V_{sg} [8], this observation supports the conclusion that the origin of the ZBPs is single-particle in nature.

All the over 50 SSET devices we fabricated show electron pairing without superconductivity in the diamond regime. However, in order to observe closed ABS loops the QD has to be coupled to one gapped superconducting lead and one gapless “probe” lead. Although we did not purposefully design the gap structure in our devices, about 10% of the devices did have pronounced ABS loops. The existence of nanoscale imperfections which will sometimes make a particular lead gapless is probably the primary factor in creating conditions necessary to observe ABS.

(iv) The Josephson regime ($V_{sg} > -10$ mV) appears at high side gate voltages (and hence, electron densities). In this regime the electron tunneling matrix element between the QD and the superconducting leads becomes large enough to enable coherent Josephson transport through the QD. The $I - V$ characteristics in this regime are consistent with the resistively and capacitively shunted junction (RCSJ) model [117, 118] of transport through a shunted Josephson junction with a typical critical current $I_c \sim 2.8$ nA (see § 4.4.1.5).

4.4 DISCUSSION

4.4.1 Theoretical Model of Transport in the SSET

The experimental signatures of attractive and repulsive electron-electron interactions in transport can be well described by a minimal model of the SSET device. The ingredients for the model are (1) a superconducting lead with gapped excitations, which acts as a source of electron pairs; (2) a QD with a single-electron level of either attractive or repulsive interactions; (3) and a normal lead with gapless excitations, which acts as a sensor of electronic states on the QD. The reason for including both a gapless and a superconducting lead in the model is the fact that sketched LaAlO₃/SrTiO₃ nanowires tend to show at the same time both electron pairing and gapless excitations. This dual nature has been observed in previous tunneling experiments [3] and is consistent with our observations of sub-gap transport all the way to zero bias.

We shall now discuss the origin of the conductance features that appear in transport measurements. Our starting point is the single-level QD Hamiltonian

$$H_{QD} = \sum_{\sigma=\{\uparrow,\downarrow\}} \varepsilon_{\sigma} n_{\sigma} + U n_{\uparrow} n_{\downarrow} \quad (4.1)$$

where $n_{\sigma} = d_{\sigma}^{\dagger} d_{\sigma}$ is the electron number operator, $d_{\sigma}^{\dagger} (d_{\sigma})$ creates (annihilates) an electron with spin σ on the QD, ε_{σ} is the single-electron energy on the QD (which is tuned by V_{sg} and B field), and U is the electron interaction parameter that can be both positive (repulsive) and negative (attractive). As we have described in the introduction, in zero magnetic field ($\varepsilon_{\uparrow} = \varepsilon_{\downarrow}$) the parity of the QD ground and first excited state depends on the sign of interactions. Specifically, for the case of attractive interactions ($U < 0$) the QD ground state has even parity as does the first excited state and the odd parity states lie at higher energies [see Fig. 24(a)].

4.4.1.1 Weak Coupling Regime How does the unusual level structure in the presence of attractive interactions on the QD reflect on transport through the QD? We begin by considering the case in which both the superconducting and the normal leads are *weakly* coupled to the QD. In this case the electrons move by a series of resonant pair tunneling processes: the electron pair tunnels from the source lead to the QD and then to the drain lead. In order for the resonant tunneling processes to take place the two-electron excitation on the QD must be resonant with an occupied two-electron state in the source lead and an empty two-electron state in the drain lead. The two-electron spectral function in a superconductor has a 4Δ gap, as compared to the one-electron spectral function that has a 2Δ gap. Taking into account this gap we find the conductance maps (see Fig. 26). We observe that in order to connect the two diamonds with a straight line, as seen in the experiment, we must have one lead gapless, resulting in a $4\Delta/e$ gap as shown in Fig. 25(a). We note that the electron pairs in the source and drain leads can still tunnel through the QD, however, the contributed conductance is very small due to the low density of states. The conductance peak at zero-bias, shown in Fig. 26(b), is consistent with the observation in Fig. 25.

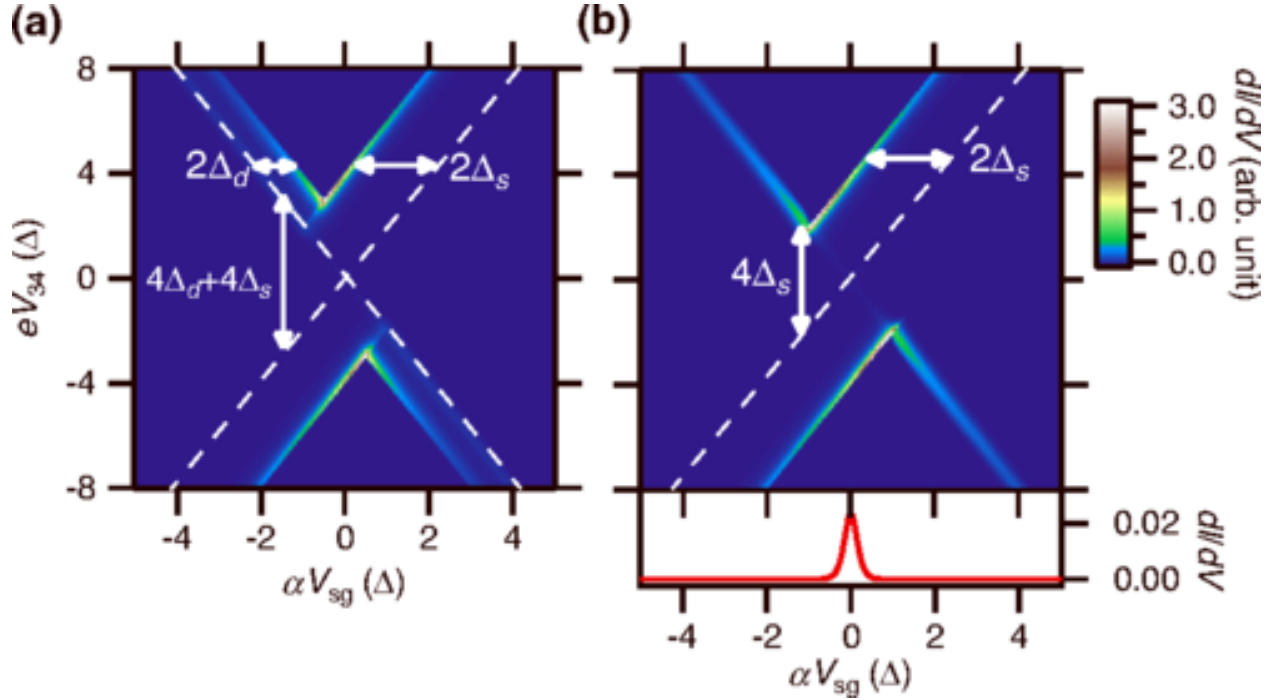


Figure 26: Simulation of pair conductance diamonds on varying gapped excitations in the leads. **a**, When both source and drain leads only have gapped excitations, the diamonds are offset away from the gapless excitations indicated by the dashed lines. An insulating gap of $4(\Delta_s + \Delta_d)/e$ appears between the tips of diamonds, where Δ_s and Δ_d are the pairing gaps of source and drain leads. **b**, When the drain lead has gapless excitations, one side of the diamonds stay connected by a straight line. Note electron pairs can still tunnel through the device when $|V_{34}| < 2\Delta_s/e$, as shown in the conductance peak at zero-bias in the bottom panel.

To calculate the conductance in the well-defined conductance diamonds regime, where the strong electron-electron attraction dominates the spectrum of the QD, we treat the electrons on the QD as being tightly bound into pairs, and low energy excitations of the QD correspond to adding or removing an electron pair from the QD. The effective Hamiltonian for the QD becomes

$$H_{QD} = (C_{sg}V_{sg} - 2ne)^2/C_{\Sigma} \quad (4.2)$$

where C_{sg} and C_{Σ} are the effective gate capacitance and total capacitance for adding electron pairs, and n is the number of pairs on QD. We model the transport through the QD using a master equation that describes the hopping of electron pairs between the leads and the QD. To connect the QD to the leads we need the two-electron spectral functions $A_1^{(2)}(\omega)$ and $A_2^{(2)}(\omega)$ in the two superconducting leads along with the pair distribution functions. We can split the spectral function in the leads into three contributions [119]:

- (1) a peak at $\omega = 0$ corresponding to the pair condensate (this peak is expected to be significantly broadened for 1D superconductors, like our leads) ;
- (2) a finite spectral weight for $\omega < 2\Delta$ corresponding to bound pairs at finite momentum (i.e. the phase and amplitude modes);
- (3) a large spectral weight at $\omega \geq 2\Delta$ corresponding to pairs of free propagating particles (either hole-like or electron-like).

Instead of computing the spectral function and the pair distribution function from first principles, we use a phenomenological model. To account for the fact that the pairs are made of electrons, we use the Fermi-distribution function n_F to model the pair distribution function. We model the spectral function using the expression

$$A_j^{(2)}(\omega) = Re\left(\frac{1}{\sqrt{\omega^2 - (2\Delta_j)^2 + i\gamma_j^2}}\right) \quad (4.3)$$

which has peaks at $\omega = \pm 2\Delta$ associated with type (3) excitation and a finite weight at $0 \leq \omega < 2\Delta$ associated with type (1) and (2) excitations.

Consider the V_{sg} range near the tip of one of the conductance diamonds where the QD level with $n + 1$ pairs becomes degenerate with the QD level with n pairs. The populations

with n and $n + 1$ pairs on the QD follow

$$\dot{c}_n = -c_n \sum_{j=1,2} A_j(\mu_j - \varepsilon) n_F(\mu_j - \varepsilon) + c_{n+1} \sum_{j=1,2} A_j(\mu_j - \varepsilon) (1 - n_F(\mu_j - \varepsilon)), \quad (4.4)$$

$$\dot{c}_{n+1} = c_n \sum_{j=1,2} A_j(\mu_j - \varepsilon) n_F(\mu_j - \varepsilon) - c_{n+1} \sum_{j=1,2} A_j(\mu_j - \varepsilon) (1 - n_F(\mu_j - \varepsilon)) \quad (4.5)$$

where $\mu_1 = eV_{34}/2$ and $\mu_2 = -eV_{34}/2$ are the chemical potentials in the two leads and $\varepsilon = \alpha(V_{sg} - V_{sg0})$ converts V_{sg} to energy with the lever arm α and V_{sg0} is the degeneracy point between states with n and $n + 1$ pairs on the QD. The corresponding current is

$$I(\mu_1, \mu_2, \varepsilon) = \frac{A_1^{(2)}(\mu_1 - \varepsilon) A_2^{(2)}(\mu_2 - \varepsilon) [n_F(\mu_1 - \varepsilon) - n_F(\mu_2 - \varepsilon)]}{A_1^{(2)}(\mu_1 - \varepsilon) + A_2^{(2)}(\mu_2 - \varepsilon)}. \quad (4.6)$$

The dI/dV obtained from this formula is plotted in Fig. 26.

4.4.1.2 Intermediate Coupling Regime As the coupling between the QD and the superconducting lead becomes stronger, the QD begins to coherently exchange electrons with the superconductor. We describe these processes by supplementing H_{QD} with H_{SC} that describes the conventional gapped Bogoliubov excitations in the superconducting lead, and H_T that describes the electron tunneling between the superconducting lead and the QD

$$H = H_{SC} + H_{QD} + H_T \quad (4.7)$$

$$H_{SC} = \sum_{k\sigma} \xi_k c_{k\sigma}^+ c_{k\sigma} + \Delta \sum_k (c_{k\uparrow}^+ c_{-k\downarrow}^+ + c_{-k\downarrow} c_{k\uparrow}) \quad (4.8)$$

$$H_T = \sum_{k\sigma} t c_{k\sigma}^+ d_\sigma + h.c. \quad (4.9)$$

where $c_{k\sigma}^+$ and $c_{k\sigma}$ are the electron creation and annihilation operators in the superconducting lead, ξ_k is the electron energy in the absence of the pairing gap Δ , and t is the tunneling coefficient.

The experimentally-observed sub-gap features can be readily seen in the one- and two-electron density of states (DOS) computed within our model (see §§ 4.4.1.3 and 4.4.1.4 for details). For the case of strong attractive interactions ($U < -\Delta$), only the two-electron spectral function has sub-gap features. These “X”-shaped features originate in pair bound states on the QD and have particle-hole symmetry [see Fig. 27(a)]. On the other hand, for the case of strongly repulsive interactions ($U > \Delta$) only the one-electron spectral function has sub-gap features, and these originate in the ABS [see Fig. 27(b)]. The qualitative appearance of these sub-gap features is not sensitive to details such as the tunneling strength t or the exact value of the interaction strength U . By comparing the sub-gap spectral function features with the experimental transport data we can identify two regimes in the transport data: the pair bound state regime and the ABS regime. We therefore identify the experimentally-observed transition in the character of transport with the change in the sign of electron-electron interactions on the QD.

To model the experimentally observed transition from attractive to repulsive interactions, we extend the QD to 4 levels with the lower 2 levels of attractive character and the upper 2 levels of repulsive character. The corresponding one- and two-electron spectral functions [see Fig. 28(b)] show two distinct regimes: “X”-shaped two-electron features at low electron densities on the QD, and loop-shaped features at high electron densities. The simple 4-level QD calculation agrees with the experimental data quite well [see Fig. 28(a)].

4.4.1.3 Spectral Functions Following Eqs. 4.7-4.9, we work in the Bogoliubov quasiparticle representation with $\xi_k = \hbar^2 k^2 / (2m^*) - E_F$, where E_F is the Fermi energy and m^* is the effective mass of the electron. The quasiparticle creation and annihilation operators can be constructed into the electron operators as

$$c_{k\uparrow} = u_k \gamma_{k\uparrow} + v_k \gamma_{k\downarrow}^+ \quad (4.10)$$

and

$$c_{-k\downarrow} = u_k \gamma_{k\downarrow} - v_k \gamma_{k\uparrow}^+, \quad (4.11)$$

where $u_k = \sqrt{\frac{1}{2}(1 + \frac{\xi_k}{E_k})}$ and $v_k = \sqrt{\frac{1}{2}(1 - \frac{\xi_k}{E_k})}$.

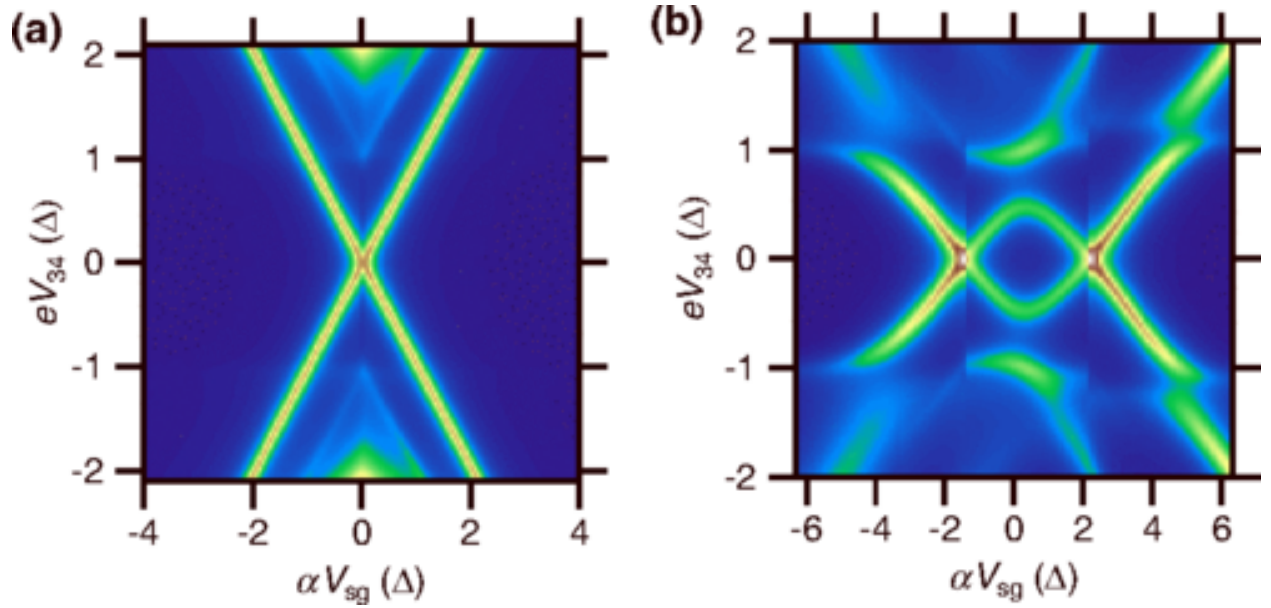


Figure 27: Theoretical calculation of DOS spectra in a single level QD in the presence of **a**, attractive ($U = -4\Delta$) and **b**, repulsive ($U = 2\Delta$) electron-electron interaction. For the case (a) of strong attractive interactions, the two-electron “X”-shaped resonances are dominant, whereas for case (b) of strong repulsion, the dominant sub-gap “loop” features are one-electron resonances with Andreev bound states.

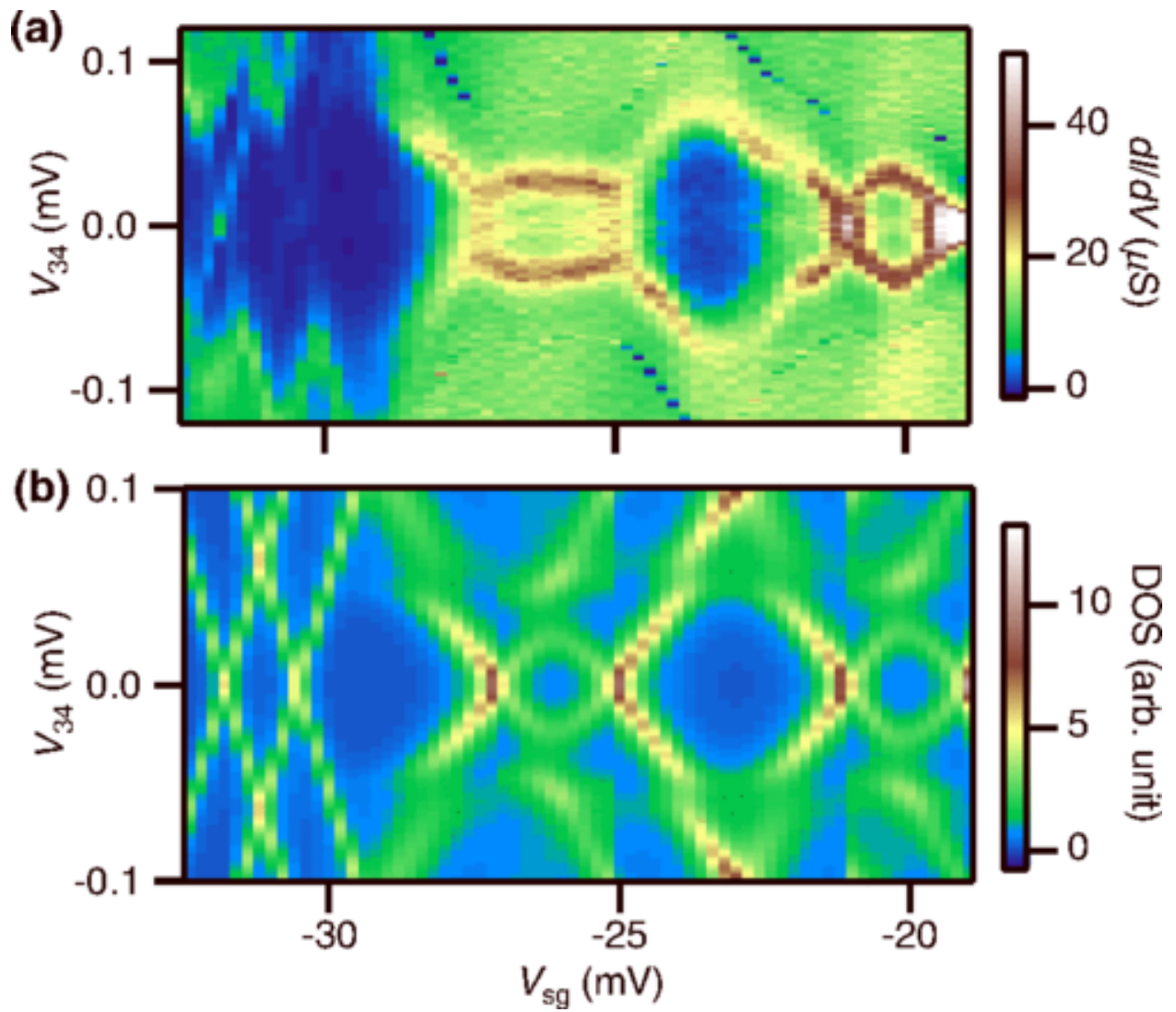


Figure 28: Comparison between data and calculation. **a**, Magnified data plot in $-33 \text{ mV} < V_{sg} < -19 \text{ mV}$. **b**, Calculation of the DOS on the QD in the same V_{sg} range. The QD is restricted to 4 levels, with negative (positive) interaction for the bottom (upper) 2 levels in band 1 (2).

This brings H_{SC} to diagonal form

$$H_{SC} = \sum_{k\sigma} E_k \gamma_{k\sigma}^+ \gamma_{k\sigma} \quad (4.12)$$

where $E_k = \sqrt{\Delta^2 + \xi_k^2}$. Then we can write H_T as

$$H_T = \sum_{kj\sigma} [t_j (u_k \gamma_{k\sigma}^+ + \sigma v_k \gamma_{k\sigma}) d_{j\sigma} + h.c.] \quad (4.13)$$

where the tunneling coefficients t_j only depend on the QDs energy level j . We then numerically reconstruct the QDs DOS by computing the one- and two-electron spectral functions, which are given by

$$A_{j,\sigma}^{(1)}(V) = \sum_n |\langle \psi_n | d_{j\sigma} | \psi_g \rangle|^2 \delta(E_n - E_g - eV) + |\langle \psi_n | d_{j\sigma}^+ | \psi_g \rangle|^2 \delta(E_n - E_g - eV) \quad (4.14)$$

$$A_{1,j}^{(2)}(V) = \sum_n |\langle \psi_n | d_{i\uparrow} d_{j\downarrow} | \psi_g \rangle|^2 \delta(E_n - E_g - eV) + |\langle \psi_n | d_{i\uparrow}^+ d_{j\downarrow}^+ | \psi_g \rangle|^2 \delta(E_n - E_g - eV) \quad (4.15)$$

where $|\psi_g\rangle$ represents the ground state of the composite S-QD system and $\{|\psi_n\rangle\}$ the manifold of excited states, with E_g and $\{E_n\}$ being their respective energies. The QDs DOS is then given by

$$N_{QD}(V) = \sum_{j,\sigma} A_{j,\sigma}^{(1)}(V) + \sum_{i,j} A_{i,j}^{(2)}(V). \quad (4.16)$$

In the calculations of this work, we account for broadening effects by replacing the delta functions in Eqs. 4.14 and 4.15 for (unity normalized) Lorentzians with width Γ of the form

$$\delta(E_e - E_g - eV) \rightarrow \frac{\Gamma/(2\pi)}{(E_e - E_g - eV)^2 + (\Gamma/2)^2}. \quad (4.17)$$

4.4.1.4 Numerical Calculation of the DOS In tunnel experiments, one can typically express the tunneling current in terms of the spectral functions. In particular, if the DOS of the tunneling probe can be assumed to be approximately constant, one can show that to lowest order in the tunneling

$$\frac{dI}{dV} \propto \sum_{j,\sigma} A_{j,\sigma}^{(1)}(-eV), \quad (4.18)$$

which allows for a direct mapping between the one-electron DOS of the device and the measured dI/dV .

We numerically reconstruct the QDs DOS by diagonalizing the model Hamiltonian as a function of chemical potential $\mu(V_{sg})$ to compute the one- and two-electron spectral functions, as instructed by Eq. 4.16. We first consider the superconductors quasiparticle modes in the continuum limit, so that

$$H_{SC} = \sum_{\sigma} \int_{\Delta}^{\infty} dE \gamma_{\sigma}^{\dagger}(E) E \gamma_{\sigma}(E), \quad (4.19)$$

$$H_T = \sum_{j,\sigma} t_j \int_{\Delta}^{\infty} dE g(E) (u(E) \gamma_{\sigma}^{\dagger}(E) + \sigma v(E) \gamma_{\sigma}(E)) d_{j,\sigma} + h.c. \quad (4.20)$$

where $\gamma_{\sigma}(E) = g(E) \gamma_{k\sigma}$ and

$$g(E) = \sqrt{\frac{L}{2\pi} \frac{dk}{dE}} = \left(\frac{L}{2\pi} \frac{\sqrt{m}}{\sqrt{2}\hbar} \frac{E}{(E^2 - \Delta^2)^{3/4}} \right)^{1/2} \quad (4.21)$$

with L being the length of the superconducting wire. We then discretize the energy integrals and the energy-dependent quasi-particle operators into M effective modes according to

$$\int_{E_i}^{E_{i+1}} dE f(E) \cong \varepsilon f(E_{i+1/2}), \quad (4.22)$$

$$\gamma_{\sigma}(E_{i+1/2}) = \gamma_{i\sigma} / \sqrt{\varepsilon} \quad (4.23)$$

where

$$\varepsilon = \frac{E_c - \Delta}{M} \quad (4.24)$$

is the energy spacing between two consecutive quasiparticle levels, defined in terms of an energy cutoff E_{cut} . Putting these results together gives the final form of the discretized superconductor and tunneling Hamiltonians

$$H_{SC} = \sum_{\sigma} \sum_{i=1}^M E_{i+1/2} \gamma_{i\sigma}^{\dagger} \gamma_{i\sigma}, \quad (4.25)$$

$$H_T = \sum_{j,\sigma} \sum_{i=1}^M \tau_{ij} \left(u(E_{i+1/2}) \gamma_{i\sigma}^{\dagger} + \sigma v(E_{i+1/2}) \gamma_{i\sigma} \right) d_{j,\sigma} + h.c. \quad (4.26)$$

where

$$\tau_{ij} = t_j \sqrt{\varepsilon} g(E_{i+1/2}) = \tilde{t}_j \left(\frac{\varepsilon E_{i+1/2} / \Delta^2}{(E_{i+1/2}^2 / \Delta^2 - 1)^{3/4}} \right)^{1/2} \quad (4.27)$$

with

$$\tilde{t}_j = t_j \left(\frac{L}{2\pi} \frac{\sqrt{m\Delta}}{\sqrt{2}\hbar} \right)^{1/2} \quad (4.28)$$

which we treat as a free parameter. Other free parameters include the QDs energies $\varepsilon_{j\sigma}$ and the interaction coefficients U_{ij} , which we adjust in order to reproduce the subgap features in the observed dI/dV characteristics shown in Fig. 28(a). We use the experimental estimate of $\Delta = 48 \mu\text{eV}$ for the superconducting gap (at $V_{sg} = -40 \text{ mV}$) and assume a linear relationship between V_{sg} and μ , phenomenologically found to be approximately given by $\mu \cong eV_{sg}/20$. The calculated DOS is shown in Fig. 28(b). This simulation is for a 4-level QD, with two levels lying within each band, with electrons in band 1 being strongly attracting ($U_1 < 0$) and in band 2 repulsive ($U_2 > 0$). We also allow for interband interactions ($U_{12} \neq 0$). To make this calculation numerically tractable, we reduce the size of the Hilbert space of the SC to the one- and the two-quasiparticle sectors, with the latter being restricted to the subspace of two-quasiparticle states of opposite spins. In addition, we further reduce the size of the total Hamiltonian matrix by only considering the coupling between states whose overall energies lie within the energy window set by the energy cutoff $E_{cut} = 6\Delta$. The broadening of resonance lines is qualitatively captured by replacing the delta functions by Lorentzians in the spectral functions and by adjusting the width Γ .

4.4.1.5 Strong Coupling Regime and RCSJ Model At sufficiently high V_{sg} values ($V_{sg} > -10$ mV), the two barriers become transparent and coherent Josephson transport becomes dominant. The $I - V$ curves can be well fitted by the extended resistively and capacitively shunted junction (RCSJ) model [117, 118]. We take into account the lead resistance R_L (of wire sections from the barriers to lead 3 and 4) and shunt resistance R_J of the QD [Fig. 29]. The $I - V$ curve takes the following form

$$I(V_{34}) = \left(I_c \operatorname{Im} \left[\frac{I_{1-i\eta}(I_c \hbar / 2ek_B T)}{I_{-i\eta}(I_c \hbar / 2ek_B T)} \right] + \frac{V_{34}}{R_J} \right) \frac{R_J}{R_J + R_L} \quad (4.29)$$

where $\eta = \hbar V_{34} / 2eRk_B T$, k_B is the Boltzman constant and $I_\alpha(x)$ is the modified Bessel function of complex order α . The extracted critical current $I_c = 2.8$ nA (at $V_{sg} = 0$ mV) is larger than the switch current $I_s = 1$ nA. Theoretically, the maximum of critical current I_{cmax} has a simple relation with Δ in the strong-coupling regime, $I_{cmax} = 2\pi\Delta a/h$ by assuming equal coupling strength of two barriers, where h is the Planck constant [120]. Taking $\Delta = 48$ μ eV, the calculated $I_{cmax} = 11.7$ nA is about 4 times of the measured result. This is in fact in excellent agreement considering only a room temperature microwave (RF) filter is used in the experiment, as electromagnetic radiation is the major reason for this discrepancy.

4.4.2 Mechanisms for Density-Tuned Interactions

While electron-electron interactions are generally tuned by the electron density, it is important to consider why the observed transition from attractive to repulsive interactions is such an abrupt function of the electron density. We suspect that the underlying mechanism is connected to the Lifshitz transition at the LaAlO₃/SrTiO₃ interface. The 2DEG at the interface is formed from the three titanium t_{2g} d electron bands. Interfacial confinement effects split these d electron bands into a lower d_{xy} band and higher d_{xz}/d_{yz} bands [28]. Lateral (1D) confinement can create subband structure but is expected to preserve the underlying orbital character.

We conjecture that the d_{xy} electrons have attractive character while the d_{xz}/d_{yz} electrons have repulsive character. At low electron densities only the d_{xy} levels are available and hence the interactions on the QD are attractive. At a critical electron density, marked

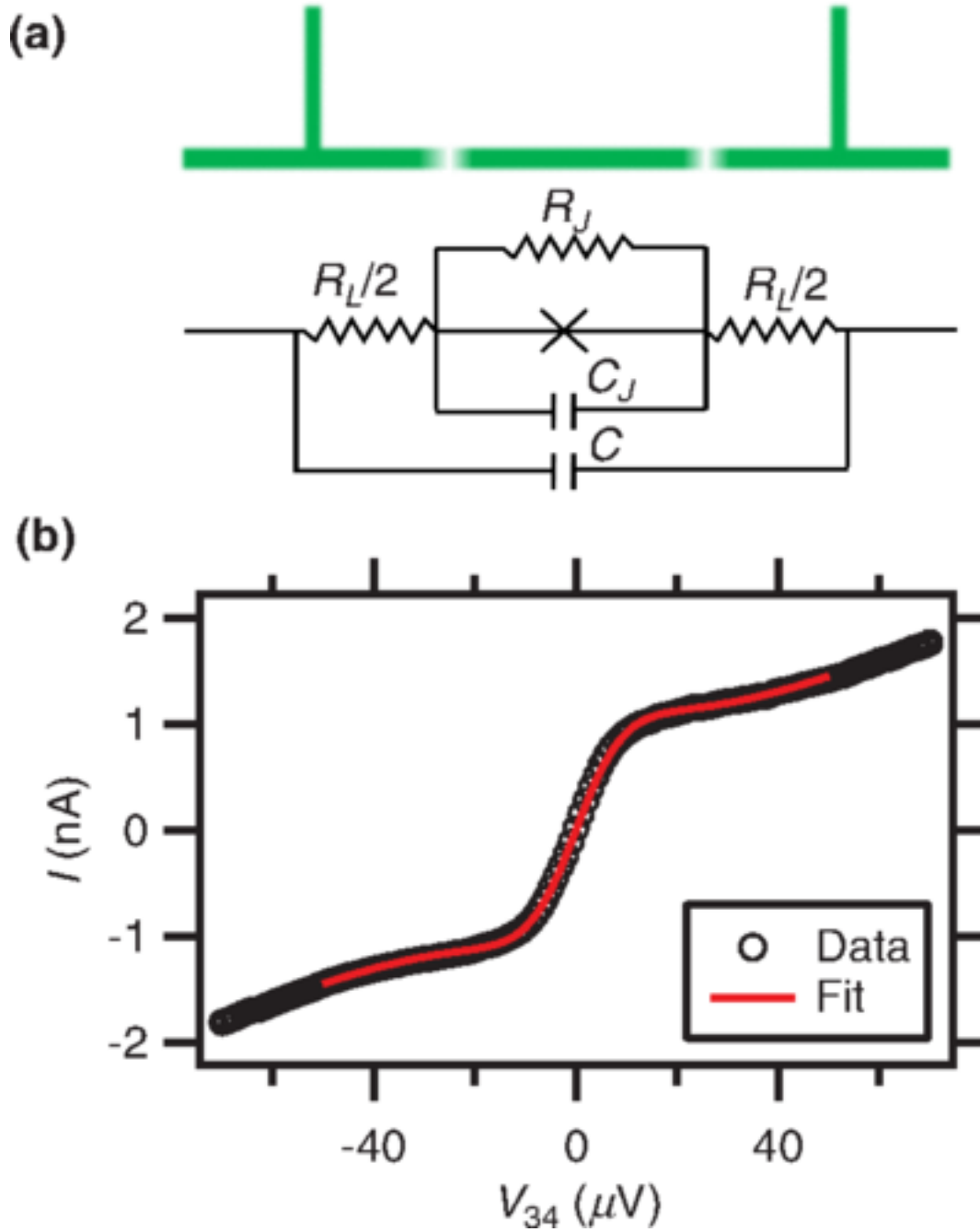


Figure 29: RCSJ model fitting. **a**, Schematic. **b**, RCSJ fitting of $I - V$ curve at $V_{sg} = 0$ mV yielding $I_c = 2.8$ nA, $R_J = 40.4$ k Ω and $R_L = 5.0$ k Ω .

by the Lifshitz transition point (on the QD), the higher d_{xz}/d_{yz} bands become available and the interactions on the QD become repulsive. This interpretation, that the lower d_{xy} band is the cradle of attractive interactions, is consistent with the measurement at the 2D LaAlO₃/SrTiO₃ interface, which shows that the optimal doping for superconductivity happens at the Lifshitz transition [28]. We note that an alternative description of phenomena ascribed to the Lifshitz transition has been presented by Maniv et al. [121], who ascribes the onset of superconductivity as arising from population of the d_{xz}/d_{yz} bands, and interactions within those bands that map out the superconducting dome.

Titanium d_{xy} ferromagnetism has been reported at the 2D LaAlO₃/SrTiO₃ interface [38], which might imply that the d_{xy} band has repulsive electron-electron interactions. However, there is evidence from a variety of experiments that d_{xy} electrons can pass through a mobility edge [122], with the localized electrons giving rise to moments available for magnetic ordering, while the latter giving rise to other transport phenomena. Indeed, there are several reports showing a coexistence of superconducting and ferromagnetic order [29, 123].

We now consider alternative explanations aside from the Lifshitz transition for the abrupt change in the character of transport. Abruptly increasing the tunneling matrix element t (e.g. by gating the barrier between the QD and the superconducting lead) may seem like a viable candidate for affecting the ground state parity [124], but an increase in t (with increasing V_{sg}) neither favors an odd parity ground state nor does it bring down the single-electron states into the gap, which conflicts with the observation here. A more workable possibility is to abruptly introduce a large Zeeman field, in the presence of attractive interactions, to break the electron pairs on the QD and thus drive a transition from the two-electron to the one-electron transport regime. However, the only possible origin of such a Zeeman field is the exchange interaction between electron spins on the QD and a magnetic impurity spin in a charge trap. Loading an electron into the charge trap has a large impact on the transport characteristics [8, 106, 107], either giving rise to a sudden “sawtooth-like” diamond if the trap is in parallel with the QD [107, 108] or causing a large insulating gap independent of the opening and closing of the pairing gap inside the diamonds if the trap is in series with the QD. Because these trap signatures are not observed here, it is highly unlikely that the transition could be attributed to the presence of impurity spin.

4.4.3 Signatures of Pre-Formed Pairs

So far we have discussed our observations of ABS at the strongly correlated LaAlO₃/SrTiO₃ interface. In other strongly correlated systems like high- T_c cuprates, ABS is predicted to exist in the pseudogap regime [125]. We now explore the correlation between ABS and pre-formed pairs in LaAlO₃/SrTiO₃ by studying the low-magnetic-field dependence of ABS loops. As shown in Fig. 30(a)-(h), the amplitude and width (2Δ in V_{34} direction) of the ABS loops shrink with increasing magnetic field. This evolution is more clearly visible by examining the average line-cuts in the range $-15 \text{ mV} < V_{sg} < -10 \text{ mV}$ [see Fig. 30(i)]. The ABS peaks are completely suppressed above $\mu_0 H_{c2} = 0.3 \text{ T}$. The remaining dip at zero bias is an indication of the pairing gap at higher fields. At $B < \mu_0 H_{c2}$, additional ZBP features appear inside the loops and carry supercurrent at $V_{sg} = -20 \text{ mV}$, -15 mV , and -6 mV where the QD levels align with the source and drain chemical potentials. These features are a consequence of coherent pair tunneling across the QD and are not present in every device. The extracted pairing energy (for the lead) decreases linearly with increasing field, with a zero-energy field intercept $B_i = 1.3 \text{ T}$ which is consistent with B_p in the lower V_{sg} regime.

4.5 CONCLUSIONS

The sign of the electron-electron interaction at the LaAlO₃/SrTiO₃ interface has a profound influence on the electron transport in SSET devices. The attractive interaction in the low V_{sg} regime results in electrons tunneling in pairs even at conditions where superconductivity is suppressed. Meanwhile, the emergence of single-particle ABS loops in the high V_{sg} regime is characteristic of repulsive electron-electron interactions. This abrupt sign change of electron-electron interactions, tuned by a single parameter V_{sg} , is postulated to be driven by the discontinuity of band structure at the Lifshitz transition.

The nature of superconductivity in SrTiO₃ is still not well understood, more than fifty years after its discovery. The observation of tunable electron-electron interactions in LaAlO₃/SrTiO₃ nanostructures provides important insights into basic mechanisms that lead

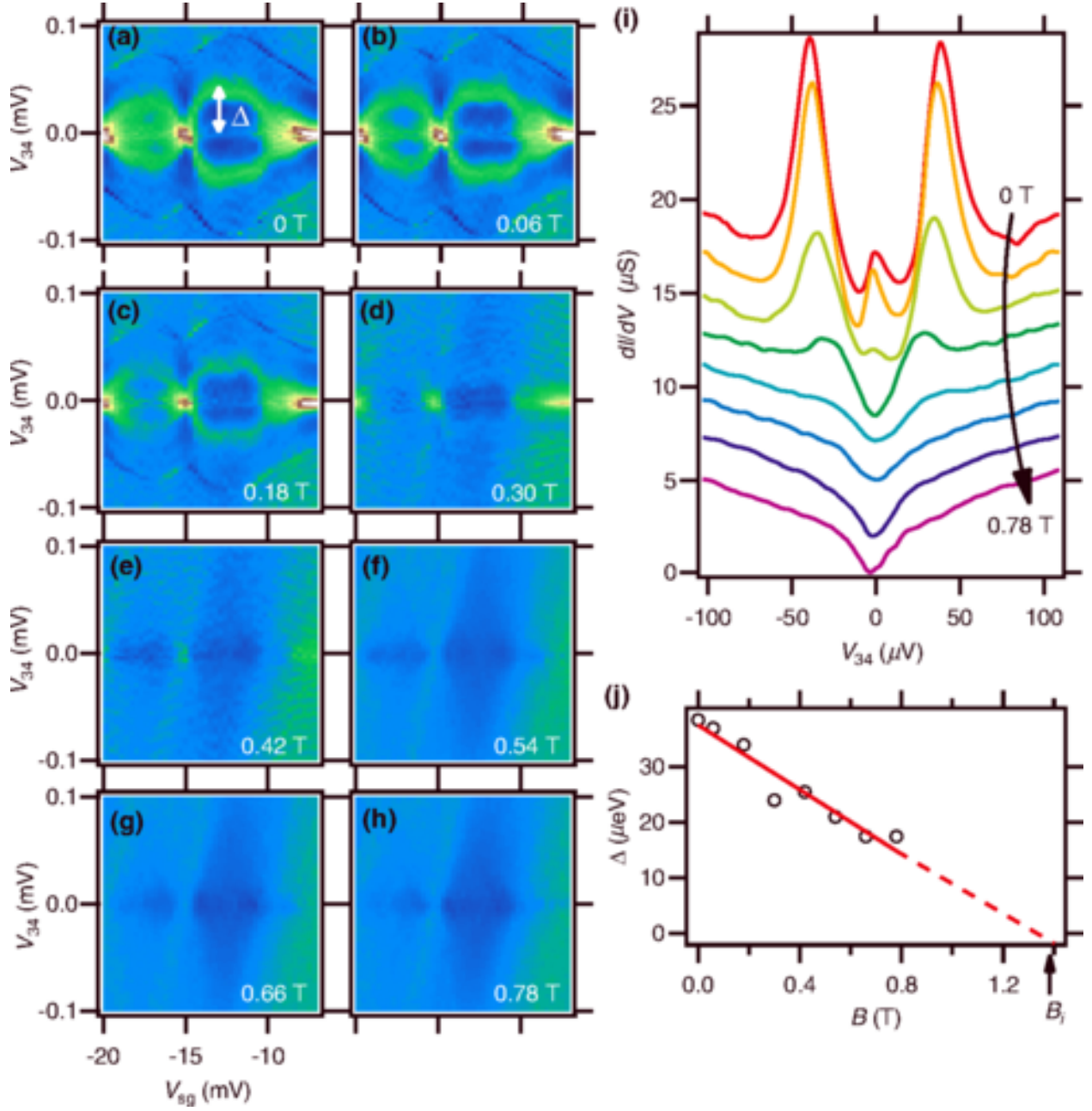


Figure 30: Low-field dependence of ABS. **a—h**, ABS loops at $B = 0$ T, 0.06 T and 0.18 T to 0.78 T in step of 0.12 T. **i**, Average vertical line cuts (averaged in -14 mV $< V_{sg} < -11$ mV). Curves are shifted for clarity. **j**, Extracted pairing gap size as function of B .

to electron pairing in SrTiO₃. At the same time, the ability to program the sign of electron-electron interactions can potentially play a critical role in solid-state quantum nanodevices and/or simulation.

5.0 MICROMETER-SCALE BALLISTIC TRANSPORT OF ELECTRON PAIRS

5.1 INTRODUCTION

The contents of this chapter represent a collaborative work published in Tomczyk, Cheng, Lee, Lu, Annadi, Veasey, Huang, Irvin, Ryu, Eom and Levy, *Physical Review Letters* **117** 096801, 2016 August 26.

5.1.1 Summary

High-mobility complex-oxide heterostructures and nanostructures offer new opportunities for extending the paradigm of quantum transport beyond the realm of traditional III-V or carbon-based materials. Recent quantum transport investigations with LaAlO₃/SrTiO₃-based quantum dots have revealed the existence of a strongly correlated phase in which electrons form spin-singlet pairs without becoming superconducting. Here we report evidence for micrometer-scale ballistic transport of electron pairs in quasi-one-dimensional (quasi-1D) LaAlO₃/SrTiO₃ nanowire cavities. In the paired phase, Fabry-Perot-like quantum interference is observed, in sync with conductance oscillations observed in the superconducting regime (at zero magnetic field). Above a critical magnetic field B_p , electron pairs unbind and conductance oscillations shift with magnetic field. These experimental observations extend the regime of ballistic electronic transport to strongly correlated phases.

5.1.2 Clean One-Dimensional Transport

Compared with the superconductor-insulator transition in two-dimensional systems, the nature of correlated electron transport in one-dimensional systems remains largely unexplored. SrTiO₃-based heterostructures and interfaces exhibit a relatively short phase coherence, of order ~ 100 nm [126, 20]. Exploring the regime where the device dimensions are smaller than the coherence length is challenging; in devices created by optical or electron-beam lithography, the carrier mobility generally decreases as the channel width is reduced to sub-micrometer scales [127, 128]. However, there is growing evidence that scattering lengths, both elastic and inelastic, are greatly enhanced for ultranarrow devices created by conductive atomic force microscope (c-AFM) lithography [71], as described in Section 2.2. It is believed that the tip induces surface protonation and deprotonation [73, 72], effectively modulating the interface conductivity [74] without disrupting the integrity of the interface, which allows long scattering lengths to be achieved.

Previous transport measurements of ~ 10 nm-wide channels at the LaAlO₃/SrTiO₃ interface show a nearly two-order-of-magnitude enhancement of room-temperature Hall mobility compared with two-dimensional counterparts [58]. At low temperature, nanowire mobilities exceed 10^4 cm²/Vs while mobility measurements of two-dimensional devices generally remain an order of magnitude lower [58, 129, 130, 131]. Quasi-one-dimensional LaAlO₃/SrTiO₃ nanowires exhibit conductance values that hover near the single-channel conductance quantum e^2/h , independent of channel length [59]. Additionally, conductance steps have been reported in edge-defined LaAlO₃/SrTiO₃ quantum wires [60]. While conductance steps can arise from any point-like constriction [48], and have also been reported in top-gated SrTiO₃ structures that do not possess a one-dimensional geometry [132], such step-like features suggest that LaAlO₃/SrTiO₃ nanowires may be able to cleanly resolve individual energy subbands.

Quantum interference experiments can provide useful information about electron scattering. Analogous to photonic interference in an optical Fabry-Perot cavity, multiple reflections of electrons from the endpoints of a nanowire cavity can lead to strong interference effects when the elastic scattering length exceeds the cavity length. This interference requires not

only phase coherence but also absence of scattering [133]; many systems with long coherence lengths have much shorter elastic scattering lengths. In ballistic Fabry-Perot cavities, the conductance through the cavity oscillates as a function of the Fermi wavelength, which varies with the chemical potential and is usually controlled by a nearby gate electrode. Only a few material systems have been shown to be capable of supporting micrometer-scale quantum interference: suspended single-wall carbon nanotubes [134], high-mobility graphene structures [135], and III-V semiconductor systems such as high-mobility heterostructures [136] and stacking-fault-free nanowires grown by vapor-liquid-solid techniques [133]. However, these systems often operate in a regime where electron correlations can be neglected; exceptions include Wigner crystal phases, and magnetically and structurally confined one-dimensional systems (i.e., Tomonaga-Luttinger liquids [55]).

Here, we observe evidence of long-range ballistic transport of electron pairs in a complex oxide system. This constitutes a new regime in which strong electronic correlations combine with ballistic electron transport.

5.2 DEVICE GEOMETRY AND FABRICATION

To investigate the ballistic nature of transport in $\text{LaAlO}_3/\text{SrTiO}_3$ nanostructures, quasi-1D Fabry-Perot cavities are created at the $\text{LaAlO}_3/\text{SrTiO}_3$ interface using c-AFM lithography [71]. To create the geometry shown in Fig. 31(a), first a nanowire of width $w \approx 10$ nm is written, followed by erasure steps to create semitransparent barriers at both ends of the cavity. Devices are transferred to a dilution refrigerator within 5 minutes of writing to minimize decay, and are cooled to a base temperature $T = 50$ mK for transport measurements. Current flows through the main channel containing the two barriers. Independent voltage leads enable four-terminal measurements of the cavity conductance, as well as that of an adjoining “open” nanowire, i.e., without barriers. The cavity lengths L between the barriers ranged from 250 nm to 4 μm . The distance from each barrier to the nearest voltage lead was held constant for all devices at 750 nm. The total distance between voltage leads 3 and 4 in Fig. 31(a) was therefore $L + 1.5 \mu\text{m}$. The 4-terminal voltage between leads 2 and 3 in

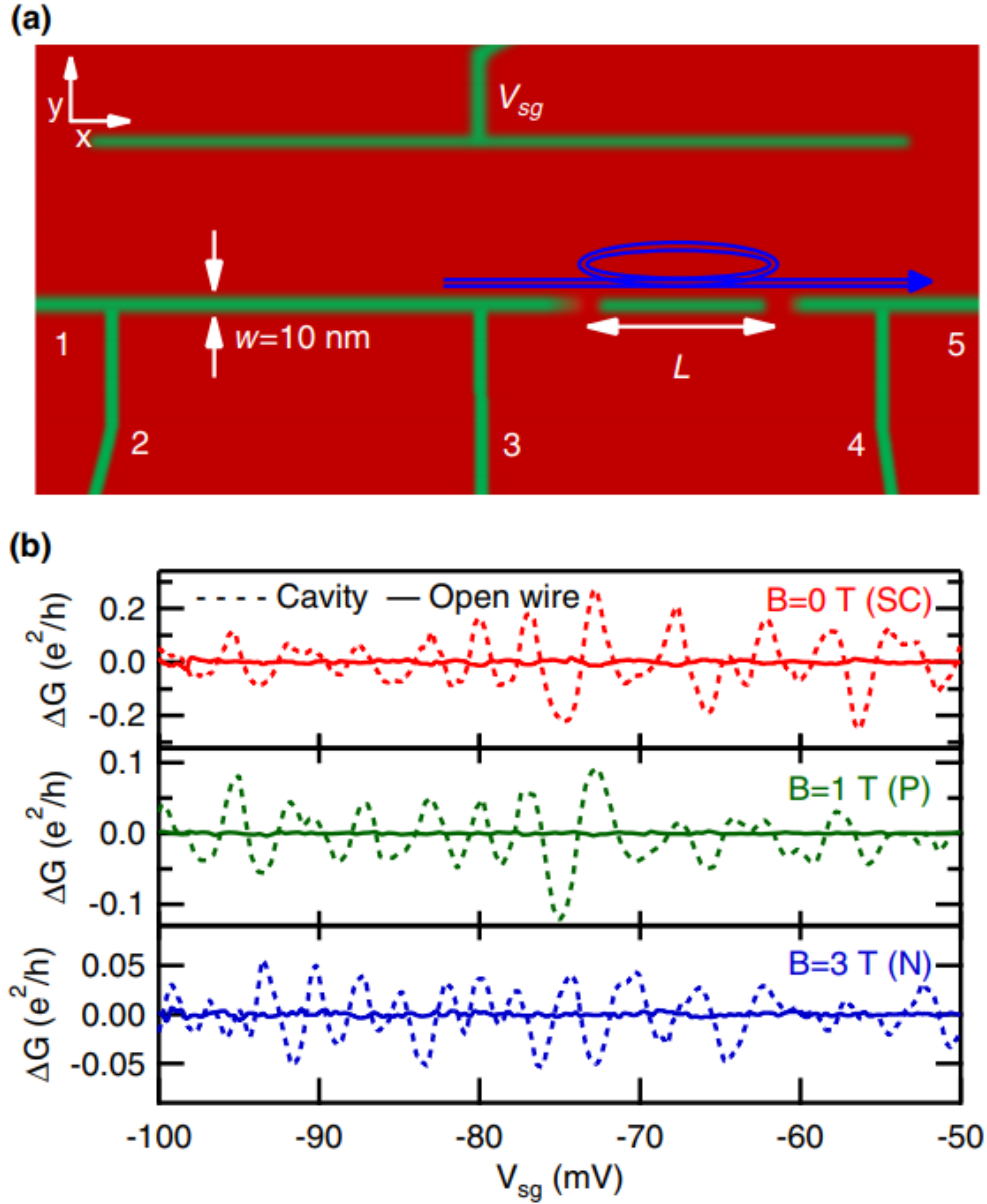


Figure 31: Device schematic and Fabry-Perot oscillations. **a**, Schematic of cavity device defined by two barriers separated by length L . Interference due to coherent scattering in the cavity results in conductance oscillations periodic in Fermi momentum. **b**, Background-subtracted zero-bias differential conductance (dI/dV) of the cavity [between voltage leads 3 and 4 in (a)] and the open wire (between leads 2 and 3) in the superconducting (red), paired (green), and normal (blue) phases of Device A clearly reveals large oscillations are only present in the cavity.

Fig. 31(a) was measured to characterize a segment of nanowire equal in length to the total $L + 1.5 \mu\text{m}$, but without manufactured barriers. This “open” segment acts as a control. The side gate was created with the same c-AFM lithography as the device, running parallel to the main current-carrying channel, about $1 \mu\text{m}$ away. The applied side gate voltage V_{sg} tunes both the transparency of the barriers and the Fermi level in the cavity. The differential conductance is extracted numerically from $I - V$ curves measured as a function of V_{sg} and magnetic field. Lock-in measurements are performed at reference frequency $f = 13.46 \text{ Hz}$ and amplitude $100 \mu\text{V}$. Cavities of length $L = 0.25 - 4 \mu\text{m}$ were studied, and all show qualitatively similar behavior.

5.3 EXPERIMENTS AND RESULTS

There are three distinct transport regimes [8] as a function of the applied magnetic field: superconducting (SC), paired (P), and normal (N). At temperatures below $T_c \approx 300 \text{ mK}$, and for out-of-plane magnetic fields below $B_c = \mu_0 H_{c2} \approx 0.2 \text{ T}$, the $\text{LaAlO}_3/\text{SrTiO}_3$ interface exhibits a sharp increase in conductance that is attributed to superconductivity, both for 2D heterostructures [4] and 1D nanowires [137]. The regime $B_c < B < B_p$ has been previously identified as a strongly correlated phase in which electrons exist as spin-singlet pairs without forming a superconducting condensate [8]. At sufficiently large magnetic fields (above $B_p \approx 2 - 5 \text{ T}$), electrons are unpaired and behave “normally”.

5.3.1 Equilibrium (zero-bias) Transport

As a function of V_{sg} , typical differential conductance $G = dI/dV$ measurements of the cavity exhibit quasi-periodic oscillations at zero-bias, i.e., $V_{4T} = 0 \text{ V}$. The variation in conductance G after subtraction of a slowly-varying background (see § 5.3.1.1) shows clear oscillations in the cavity, but not in the open wire, in all three phases [Fig. 31(b)]. In the superconducting state, the conductance oscillations correspond to modulation of the critical current (see § 5.3.1.2).

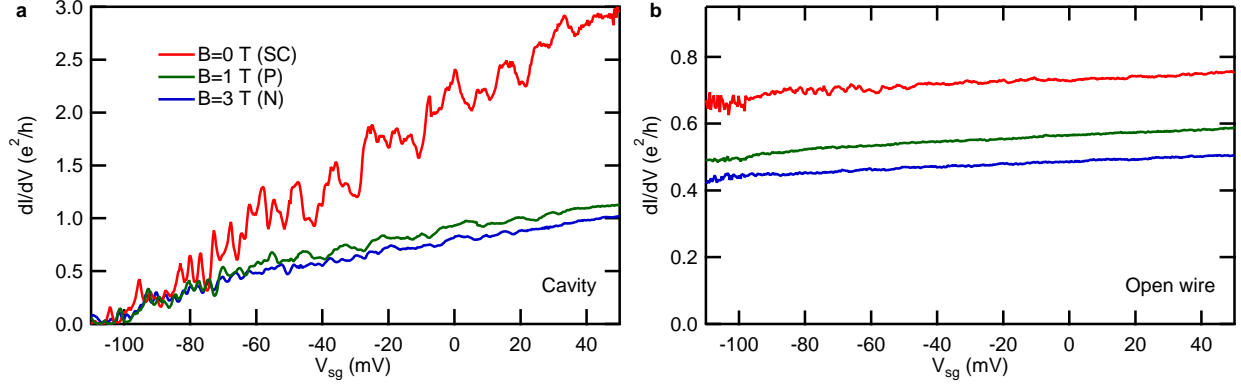


Figure 32: Differential conductance. **a—b**, Zero-bias differential conductance (dI/dV) of the cavity (between voltage leads 3 and 4 in Fig. 31(a)) and the open wire (between leads 2 and 3) in the superconducting (red), paired (green) and normal (blue) phases of Device A.

5.3.1.1 Background Subtraction The original zero-bias dI/dV linecuts from which the panels in Fig. 31(b) were derived are shown in Fig. 32 for both the cavity (a) and the open wire (b). A high-order polynomial fit to a V_{sg} subset from -105 to -48 mV was performed and the resulting slowly-varying background is overlaid with the original data in Fig. 33 for both the cavity and open wire in the superconducting (a), paired (b) and normal (c) phases. The root-mean-square amplitude of the fluctuations in the open wire are suppressed by over 90% compared to the cavity. Interestingly, the background conductance of the normal-state cavity reveals step-like features superimposed beneath the oscillations, reminiscent of interference oscillations originally predicted in ballistic devices with quantized conductance [138]. While these steps are clearly much less than e^2/h , this suggests that perhaps, with refinement of these experiments, quantized conductance is possible to achieve in these ballistic LAO/STO nanowires.

5.3.1.2 Superconducting Phase and Modulation of Critical Current At magnetic fields $|B| < B_c$, the device is superconducting and the conductance is significantly enhanced (Fig. 32, red) compared to the non-superconducting paired phase (green) and the

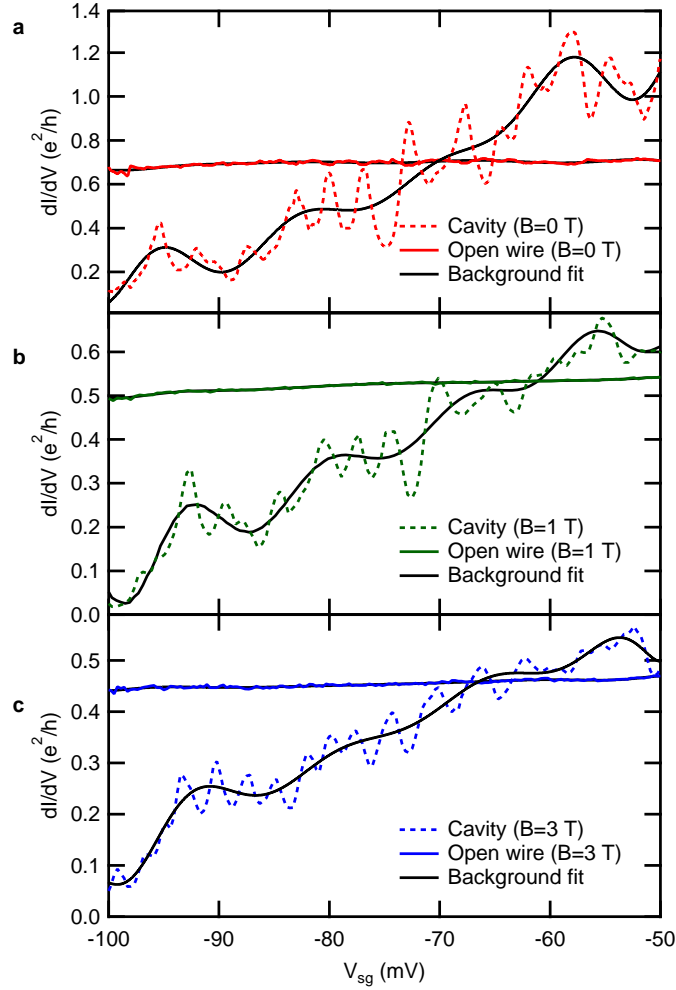


Figure 33: Background subtraction. **a—c**, dI/dV of the cavity (dash) and open wire (solid color) for Device A at $B = 0$ T (**a**), $B = 1$ T (**b**) and $B = 3$ T (**c**). Data shown here is the subset $-100 \text{ mV} < V_{sg} < -50 \text{ mV}$ of the corresponding red, green and blue curves in Fig. 32. A slowly-varying background is overlaid on each curve (solid black). The result ΔG (Fig. 31(b)) of subtracting the slowly-varying background from dI/dV reveals Fabry-Perot interference in the cavity.

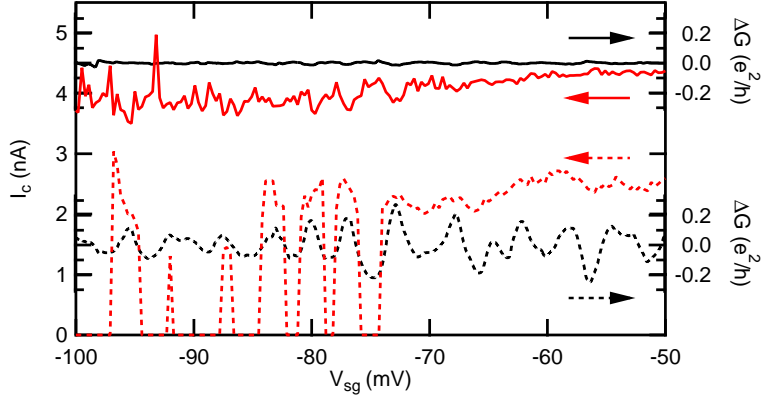


Figure 34: Critical Current Modulations. Critical current I_c of the cavity (red dash) can be greatly modulated with V_{sg} , while I_c of the open wire (red solid) is mostly constant. ΔG of the cavity (black dash) and open wire (black solid) are overlaid with I_c .

normal phase (blue). While a zero-resistance superconducting state is usually not achieved in nanowires, likely due to the increased susceptibility of low-dimensional superconductors to thermally-activated phase slips and other effects [77], the nanowire cavity shows a strong enhancement of conductance oscillations in the superconducting regime (Fig 31(b)). These features are associated with a modulation of the critical current I_c (Fig. 34), similar to supercurrent transistors [139]. While such strong I_c modulation does not occur in the open wire, a slight anti-correlation is observed between the I_c of the cavity and open wires (e.g. $80 \text{ mV} < V_{sg} < 70 \text{ mV}$). To study the critical current as a function of gate voltage, I_c is defined as the location of the resistance peaks in the dV/dI versus I curve. This switching current can be smaller than the true critical current due to dissipation events which prevent a zero-resistance state, but nonetheless can qualitatively characterize the superconducting behavior.

5.3.2 Transconductance

The transconductance dG/dV_{sg} (Fig. 35, left panels), which is computed by numerically differentiating the zero-bias conductance G with respect to side gate, reveals distinct features in

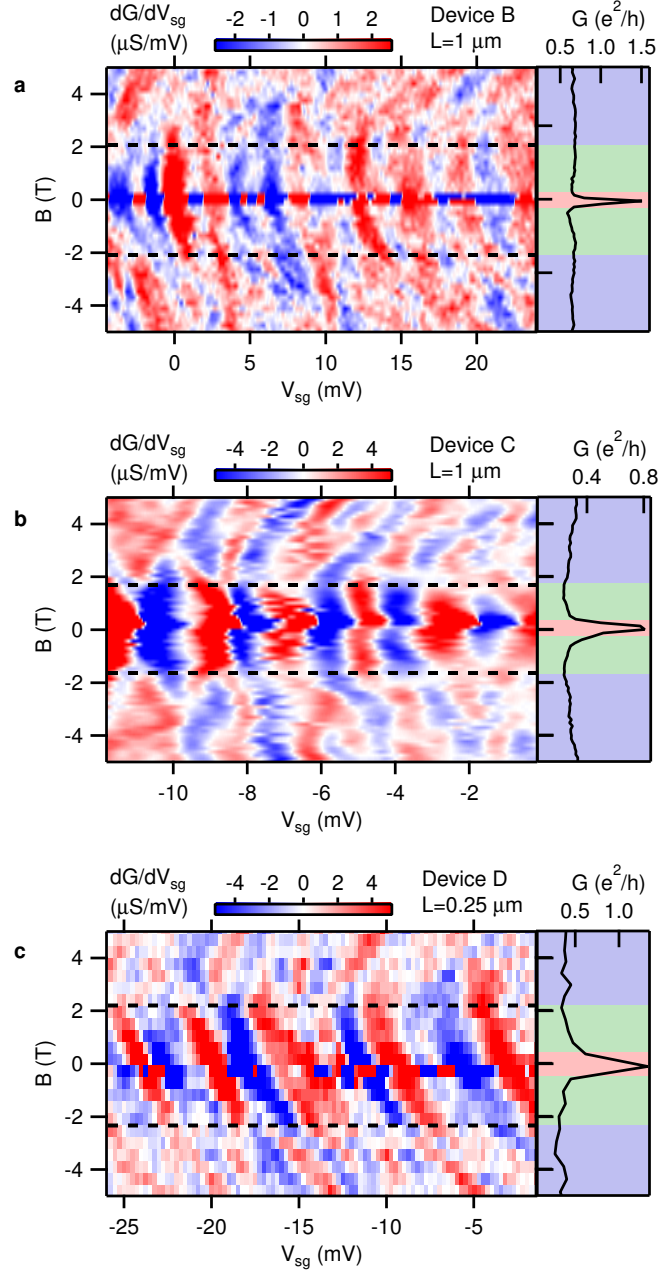


Figure 35: Magnetic field dependence of conductance oscillations for three devices. Left panels, Transconductance dG/dV_{sg} from a lock-in amplifier measurement of G at small ($100 \mu\text{V}$) bias versus B and V_{sg} . Alternating red and blue regions correspond to conductance oscillations. Right panels, Linecuts of G versus B , at $V_{sg} = 0, -2,$ and 0 mV for (a), (b), and (c) respectively, show a sharp peak attributed to superconductivity at $|B| < B_c \approx 0.2$ T (shaded red), while the conductance in the paired (shaded green) and normal (shaded blue) phases is reduced.

the superconducting, paired and normal regimes. The superconducting state is characterized by a sharp conductance peak below $B < B_c$, (Fig. 35, right panels, shaded red); correspondingly, the transconductance exhibits large oscillations. For $B > B_c$, the oscillations decrease in amplitude, yet maintain a definite phase relationship with the superconducting state modulations, confirming that transport continues to be dominated by electron pair states despite the loss of superconducting coherence. This phase relationship is preserved over the magnetic field range $B_c < B < B_p$ (shaded green). A magnetically-induced universal phase shift, which occurs throughout the field range but is hysteretic and not symmetric with field, is subtracted from the data [8]. This global effect does not alter the internal structure of the conductance oscillations. Across $|B| < B_p$, the universal shift is generally very small compared to the shift at large fields (see § 5.3.2.1), indicating an overall insensitivity to magnetic fields, consistent with the spin-singlet nature of the paired state. For $B > B_p$ (shaded blue), the electron pairs break and the transconductance oscillations split and change markedly with magnetic field.

5.3.2.1 Universal shift A global shifting of the conductance features along the side gate axis can result from a number of effects. Many of these are mundane; for example, over the course of a 12-hour experiment, a device might become slightly more (or less) resistive. Temperature fluctuations can also cause such shifting. As the magnet in our system sweeps across zero field, the temperature spikes, then gradually decays back to base temperature, causing a slight asymmetry in the data. Additionally, as the field sweeps, any localized moments in the vicinity of the device can interact with the field and affect the device.

This global shift in each device is not repeatable or single-valued as a function of magnetic field. Fig. 36 shows consecutive field sweeps from 9 to -9 T, and then from -9 to 9 T, for Device C. Clearly the global shift is different for each of these measurements, though in each case, the least drastic shift occurs across $|B| < B_p$. Additionally, the effect of the instrumental temperature spike across zero field can be observed in the asymmetry of the amplitude of the superconducting peak— in the reverse sweep (Fig. 36(a)), the amplitude is larger on the positive field side, then sharply drops at zero field, while in the forward sweep (Fig. 36(b)), the opposite occurs.

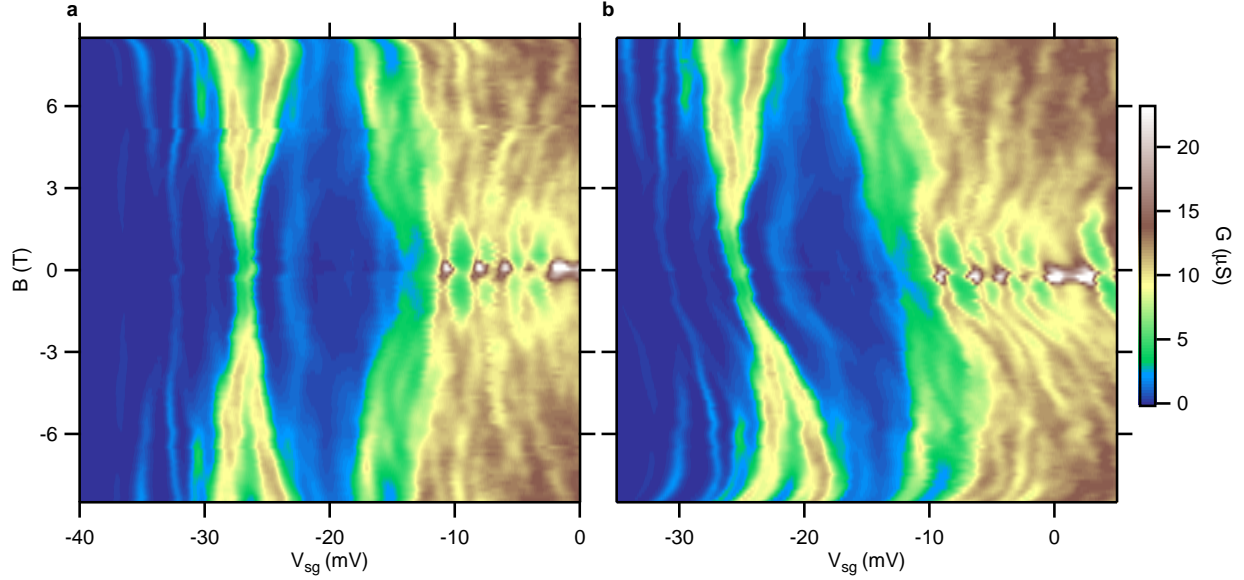


Figure 36: Non-repeatable global shift. **a**, Magnetic field sweep from +9 T to -9 T. **b**, Magnetic field sweep from -9 T to +9 T for the same device.

In Fig. 35(a) (Device B), a universal shift along the side gate axis has been subtracted from the data in the same way as described in Ref. [8]; namely, the side gate axis plotted in Fig. 35(a) is given by $V_{sg}(B) = V_{sg0}(B) - \delta V_{sg}(B)$. The global offset $\delta V_{sg}(B)$ is depicted in Fig. 37. At $|B| < B_p$, the shift is small; above B_p , the shift increases in magnitude. The shift is very asymmetric.

5.3.3 Non-Equilibrium Transport

Transmission resonances through the cavity occur when the quantum phase associated with round-trip passage is altered by a change in chemical potential or magnetic (Zeeman) interaction. In the “equilibrium” case [Fig. 38(a),(c),(e), colored lines], in which there is no net bias across the cavity, oscillations appear as a function of the applied side gate voltage, which changes the wavelength of the propagating electron states. In the “non-equilibrium” regime [Fig. 38(b),(d),(f)], an applied source-drain bias can also change the phase; the result is a

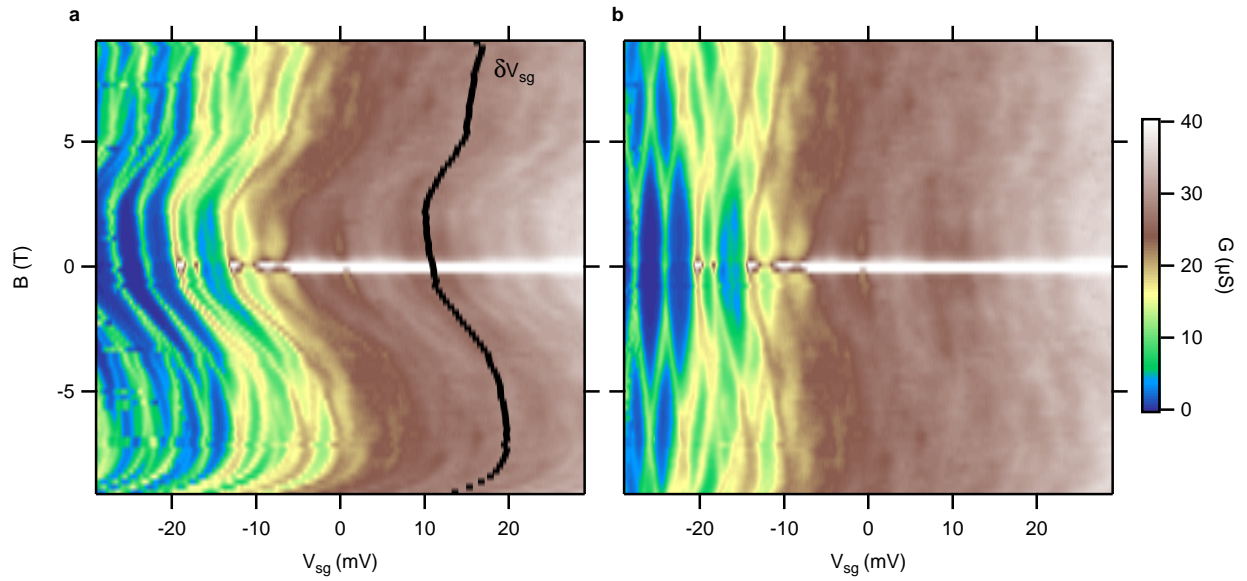


Figure 37: Global shift correction. **a**, Original data for Device B. The global shift is depicted by the black trace, $\delta V_{sg}(B)$. **b**, The same data corrected by shifting the side gate axis of each line by $V_{sg}(B) = V_{sg0}(B) - \delta V_{sg}(B)$.

characteristic “checkerboard” pattern similar to what has been reported for other systems such as carbon nanotubes [134, 133]. In Fig. 38(a),(c), and (e), the non-equilibrium linecuts (black) are out-of-phase with the zero-bias oscillations, creating the checkerboard patterns. The observed transconductance oscillations are consistent with Fabry-Perot interference in cavity devices up to 4 μm in length (Fig. 38).

5.4 DISCUSSION

5.4.1 Modeling of Fabry-Perot Interference

The band structure of the material determines the detailed nature of the observed Fabry-Perot oscillations [140]. Resonant transmission through a cavity of length L is periodic in the Fermi momentum, $k_F = n\pi/L$, so that the period is inversely proportional to length; however, a quadratic relationship between k_F and Fermi energy E_F leads to a resonance period which depends on the effective mass of the energy band, and increases with energy (see Fig. 39). This is in contrast to the constant periodicity of Fabry Perot oscillations in carbon nanotube systems, which have a linear dispersion [134]. Additionally, bulk SrTiO_3 has three degenerate $3d$ conduction bands with t_{2g} orbital character, and interfacial confinement produces an approximately 50 meV upward shift of the d_{xz} and d_{yz} bands relative to the lighter d_{xy} band [32]. The finite width of the quasi-1D nanowire can introduce a manifold of transverse subbands. When new subbands become accessible, abrupt changes in oscillation frequency are expected and observed, and beating between oscillations due to different bands can disrupt a simple checkerboard pattern. These effects can lead to checkerboards appearing in the different subsets mentioned above, and can obscure a direct linear relationship between device length and the interference V_{sg} period. Additionally, inter-mode scattering can affect the Fabry-Perot checkerboards, but is not included in the simple transmission model in Fig. 39.

Both the geometry of the device and the band structure of the material contribute to the interference signatures in a Fabry-Perot cavity [140, 141]. For materials with a single

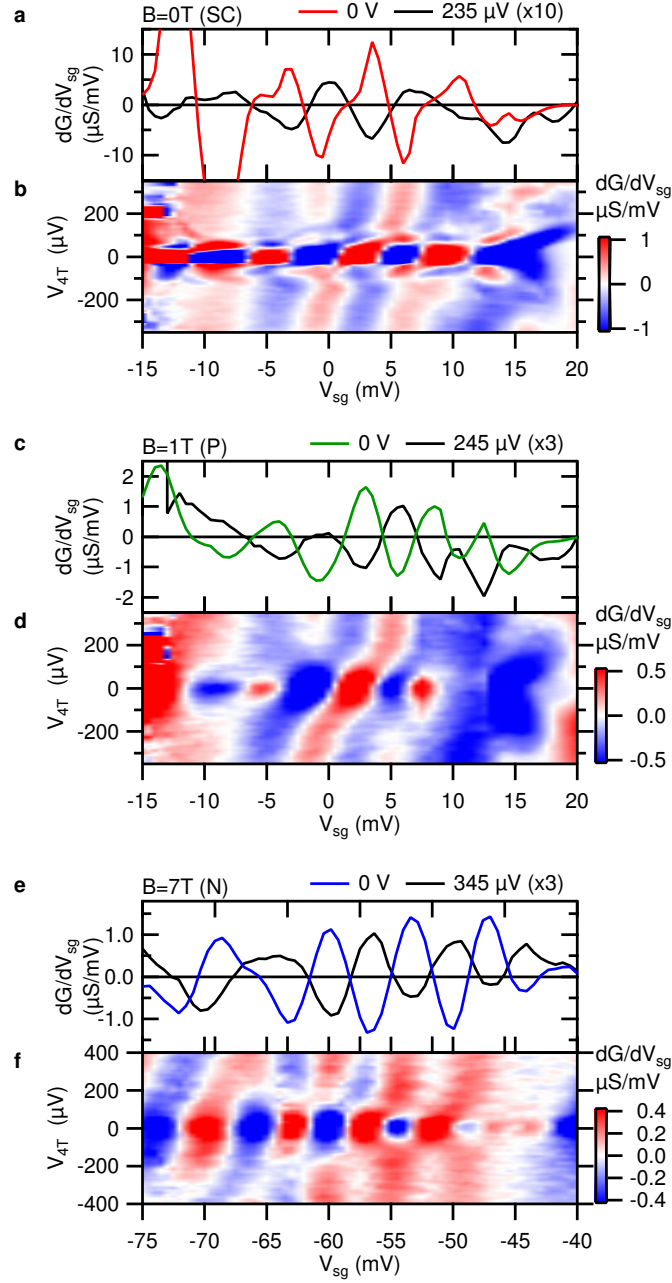


Figure 38: Fabry-Perot interference signatures at finite bias for an $L = 4\mu\text{m}$ cavity (Device E). **a**, **c**, **e**, Zero-bias and finite-bias dG/dV_{sg} linecuts as a function of V_{sg} at $B = 0\text{ T}$ [(a), SC], $B = 1\text{ T}$ [(c), P], and $B = 7\text{ T}$ [(e), N]. **b**, **d**, **f**, dG/dV_{sg} vs V_{4T} and V_{sg} in the superconducting phase [(b), $B = 0\text{ T}$], paired phase [(d), $B = 1\text{ T}$] and normal, unpaired electron phase [(f), $B = 7\text{ T}$], showing checkerboard features in each phase.

band, resonant transmission through a cavity of length L is periodic in the Fermi momentum, $k_F = n\pi/L$. While a linear dependence of Fermi energy E_F on momentum leads to a constant V_{sg} resonance period, a quadratic energy dispersion leads to a V_{sg} period which depends on the effective masses of the various bands, and increases with energy [140] (1-band model in Fig. 39 (a,b)). Bulk STO has three degenerate $3d$ conduction bands with t_{2g} orbital character. Interfacial confinement produces a ~ 50 meV upward shift of the d_{xz}/d_{yz} bands relative to the d_{xy} band [32], while lateral confinement in quasi-1D nanowires is expected to create a manifold of transverse subbands. Here, we simulate these multiple modes in a double-barrier transmission model. Fig. 39 (b) shows an expected interference pattern for a nanowire with three distinct transverse subbands. Although the orbital character of the carriers is not known in these experiments, we assume the three subbands originate from the same d_{xy} orbital.

Total conductance is calculated from the Landauer formula

$$G = \frac{e^2}{h} \sum_i T_i \quad (5.1)$$

where T_i are the transmission of each energy subband i . In this analysis, each subband is assumed to contribute e^2/h , not $2e^2/h$, because the simulation is being compared with data taken in large magnetic fields which drive the LAO/STO interface system normal and break electron pairs [8], so that energy subbands are not assumed to be spin degenerate. Transmission in a quasi-classical approximation [141] is given by

$$\begin{aligned} T_i &= \frac{1}{P^2 + Q^2 + PQ \cos 2k_i L}; \\ P(\epsilon_L, \epsilon_R) &= \sqrt{(1 + e^{-2\pi\epsilon_L})(1 + e^{-2\pi\epsilon_R})}; \\ Q(\epsilon_L, \epsilon_R) &= e^{-\pi(\epsilon_L + \epsilon_R)}; \end{aligned} \quad (5.2)$$

where $\epsilon_{L,R} = (E_F - V_b)/\hbar\omega$ give the Fermi energy E_F normalized by the barrier height V_b and width ω . At each E_F , the momentum k_i for each subband i with subband bottom E_i below E_F was calculated for a parabolic dispersion

$$k_i = \frac{\sqrt{2m_{eff}(E_F - E_i)}}{\hbar}. \quad (5.3)$$

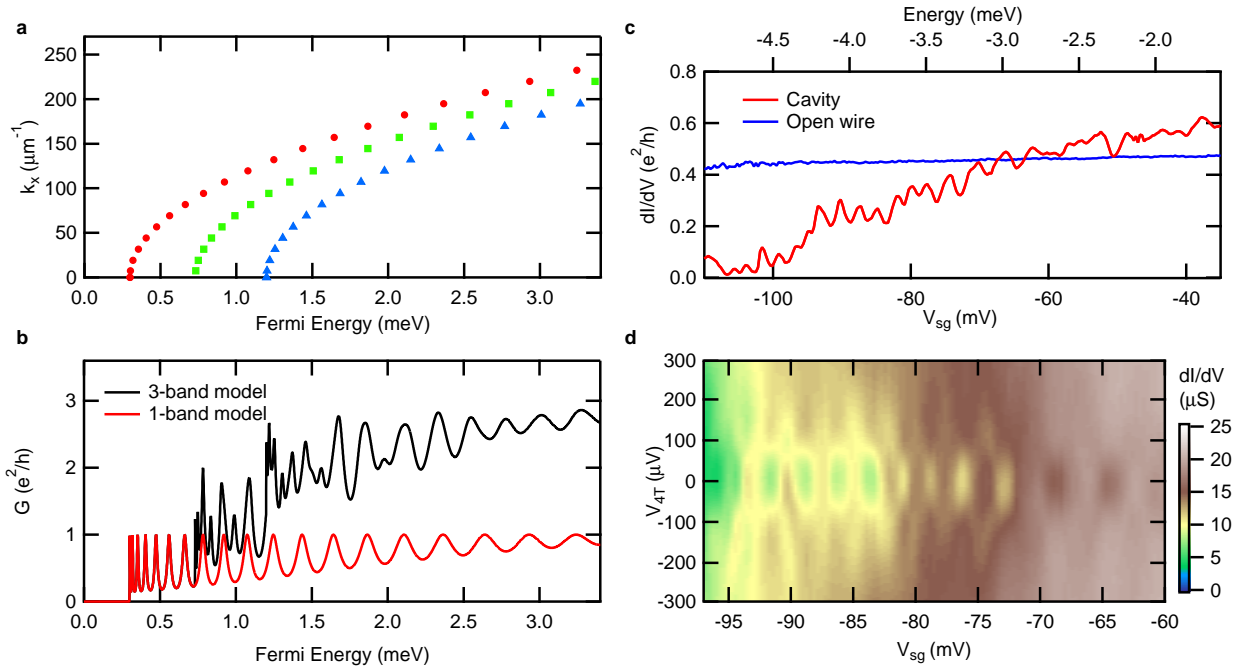


Figure 39: Semi-classical transmission model. **a**, Resonant states periodic in momentum are depicted by symbols for parabolic dispersion of three transverse subbands. **b**, Conductance oscillations due to the lowest energy subband in (a) (red) and conductance oscillations due to coherent transport of all three subbands depicted in (a) (black). **c**, Zero-bias ($V_{4T} = 0$) differential conductance (dI/dV) of Device A ($L = 0.25 \mu\text{m}$, $B = 3 \text{ T}$) for both the cavity and the open wire. Cavity conductance features quasi-periodic oscillations that qualitatively resemble a multimode transmission model. **d**, dI/dV versus V_{4T} and V_{sg} for Device A show a smoothly-changing period over a subset of V_{sg} .

The three-subband model in Fig. 39 uses an effective mass [82] $m_{eff} = 0.7m_e$ for all subbands, assuming that the subbands all originate from the same orbital. Other parameters used are $E_1 = 300 \mu\text{eV}$, $E_2 = 730 \mu\text{eV}$ and $E_3 = 1200 \mu\text{eV}$, barrier height $V_b = 100 \mu\text{eV}$, barrier width $\omega = 1 \times 10^{13} \text{ s}^{-1}$, and length of the cavity $L = 250 \text{ nm}$. The momentum states which give a maximum in T_i are shown in Fig. 39 (a) for the energy dispersion in Eq. (5.3). For the lowest subband depicted (red circles), the conductance in units of e^2/h is calculated according to Eqs. (5.1-5.2). Since Fig. 39 (a-b) share an axis, it is easy to see that each resonant state in the dispersion of the lowest (red) subband in Fig. 39 (a) corresponds to a peak in conductance in the red curve in Fig. 39 (b). The resonant states occur periodically in k_i , and therefore the spacing between resonances increases as a function of E_F . Finally, the conductance for all three subbands was calculated according to Eqs. (5.1-5.2) (Fig. 39 (b), black). In this case, beating between the resonances occurs, resulting in what appear to be random fluctuations in conductance. Zero-bias dI/dV linecuts in the normal, unpaired state (Fig. 39 (c)) clearly show the qualitative similarity between the multiband model and the conductance oscillations observed in cavity devices, contrasted with the lack of such features in the open wires with no barriers. A plot of dI/dV extended to finite bias shows a slowly-increasing period between resonances, as expected, for a small range of V_{sg} (Fig. 39 (d)).

5.4.1.1 Coupling Factor The coupling factor, or lever arm, of the side gate can be determined from Fig. 39 (d) by comparing the size of the oscillations along the V_{sg} and V_{4T} axes, similar to how the coupling factor is determined for coulomb diamonds. Here, in the gate range $-92 \text{ mV} < V_{sg} < -83.5 \text{ mV}$, there are 3 oscillations with an average period of 2.8 mV, extending to $V_{4T} = 125 \mu\text{eV}$, which can be directly converted to energy. This gives a coupling factor of $0.125 \text{ meV}/2.8 \text{ mV} = 0.045 \text{ eV/V}$. This coupling factor was used to determine the equivalent energy scale for Fig. 39 (c). The energy ranges in Fig. 39 (b) and (c) are the same size, though an exact quantitative match is not expected due to the assumptions in the model, such as effective mass, subband spacing, number of subbands, and barrier characteristics- specifically, that the barriers are identical. However, qualitative features- namely, the subsets of quasi-periodic oscillations- are present in both the model and normal-state data. Finally, we note that there is no established transport theory of electron

pairs, so the paired regime, while in some ways qualitatively similar to the normal regime, represents new physics that extends beyond this model.

5.4.2 Finite-Bias Transport

Despite all cavity devices exhibiting zero-bias conductance oscillations, full checkerboard patterns extending to finite source-drain bias only appear in small subsets of gate voltage in most devices. For example, the 4 μm cavity exhibits checkerboards for $-15 \text{ mV} < V_{sg} < 20 \text{ mV}$ in the superconducting and paired phases, and for $-75 \text{ mV} < V_{sg} < -45 \text{ mV}$ and $10 \text{ mV} < V_{sg} < 40 \text{ mV}$ in the normal-state at $B = 7 \text{ T}$ (Fig. 38). Non-equilibrium effects such as heating and the availability of a range of momentum states can dephase transport and damp the oscillations at sufficiently high bias values [Fig. 38(a),(c),(e), black lines]. The preeminence of dips, rather than peaks, has been explained by inter-mode coupling at the scattering centers [134]; the occupation of multiple subbands within the cavity increases the likelihood of inter-mode coupling, which can also lead to suppression of coherence signatures at finite bias.

5.4.3 Single-Barrier Devices

Twelve devices were made with a single barrier, rather than the two barriers which define a cavity. The four-terminal leads were between $0.5 - 1.5 \mu\text{m}$ from the barrier, for a total wire length of $1 - 3 \mu\text{m}$ between the leads for the dozen devices. Half of the devices show no blockade or Fabry-Perot, like Device G in Fig. 40. Compared to a cavity device like Fig. 39(c), Device G clearly has no quasi-periodic oscillations, even at zero-bias. The only non-linear behavior occurs as the device is pinched off by a low side gate voltage. Above a conductance value of $\sim e^2/h$, the conductance increases monotonically with increasing gate bias. The other half of the single barrier devices exhibit both blockade behavior and Fabry-Perot interference. This suggests that an unintentional second barrier exists in these devices, forming a cavity and resulting in the associated interference patterns. These unintentional potential barriers may contribute additional features in some of the devices with two engineered barriers. However, the disorder is not strong enough to cause blockade or Fabry-Perot signatures

in open nanowires with no intentionally manufactured barriers, further supporting the claim of a long elastic scattering length.

5.4.4 Transport through the Open Wire

While conductance oscillations through the cavity are evident for all values of magnetic field explored (up to 9 T), the open wire shows strong suppression of oscillations in all three phases [Fig. 31 (b)]. The root-mean-square amplitude of conductance fluctuations of the open wire is reduced by an order of magnitude compared with the cavity, suggesting that imperfections in the nanowires contribute negligibly to scattering. The pattern of behavior described here, for both cavities and open wires, is consistently observed for all of the 50 cavity devices studied.

5.5 CONCLUSION

While systems which support Fabry-Perot interference are expected to act as quantum dots when tuned to a tunneling regime, not all 1D quantum dot systems can exhibit Fabry-Perot interference [142]. Resonant tunneling observed in LaAlO₃/SrTiO₃ nanowire-based quantum dots at low V_{sg} suggests that extended coherent states exist [8], but does not rule out disorder, which randomizes carrier paths in the transport regime at high V_{sg} . In contrast, Fabry-Perot interference as described here demonstrates micrometer-scale elastic scattering lengths in these nanowire cavities. Interestingly, such clean 1D transport differs from behavior reported in 2D devices. However, local probes have revealed the existence of narrow channel flow along ferroelastic domain boundaries [14, 15], so understanding the distinctive transport in quasi-1D structures is possibly relevant for transport measurements of the 2D LaAlO₃/SrTiO₃ interface.

The observation of Fabry-Perot interference in the paired regime provides evidence for ballistic transport of electron pairs in the quasi-1D LaAlO₃/SrTiO₃ nanowire system. This result is in sharp contrast to Cooper pair insulators, in which electron pairs surviving outside

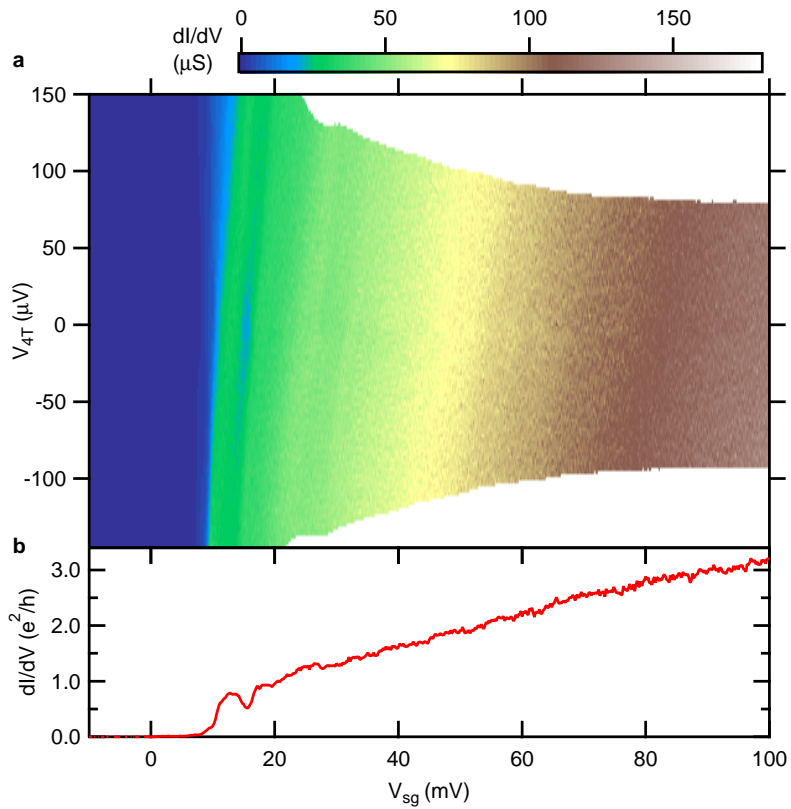


Figure 40: Single barrier device. **a**, dI/dV versus V_{4T} and V_{sg} for Device G at $B = 3$ T. **b**, dI/dV linecut at zero-bias ($V_{4T} = 0$). No Fabry Perot conductance oscillations are observed.

of the superconducting state are localized [143]. Metallic Bose phases have been observed in both optical lattice [144] and solid state [143] systems, but even in clean superconductors where the mean free path is longer than the superconducting coherence length, the mean free path is only on the order of 10 nm [145]. Additionally, these metallic Bose phases always appear below the upper critical field for superconductivity in their systems. The results observed here in $\text{LaAlO}_3/\text{SrTiO}_3$ nanowires are distinct due to both the ballistic nature of transport of the uncondensed electron pairs, and the persistence of this ballistic pair state well above the upper critical field for superconductivity in $\text{LaAlO}_3/\text{SrTiO}_3$.

Coherent, ballistic transport can be associated with delocalization of the electron wavefunction. For the case of ballistic electron pairs, this description is inadequate since it does not describe the strong correlations leading to the formation of composite bosons. Furthermore, what happens when this delocalization length greatly exceeds the superconducting coherence length? In $\text{LaAlO}_3/\text{SrTiO}_3$, the superconducting coherence length is ~ 100 nm [4], much shorter than the micrometer-scale ballistic transport of electrons and electron pairs. Can competition between superconductivity and delocalization alter or suppress the superconducting state in these nanowires? A theoretical framework is necessary for answering the questions raised by the ballistic transport of electron pairs.

Long-range coherent and ballistic transport in a strongly-correlated electronic phase suggest $\text{LaAlO}_3/\text{SrTiO}_3$ nanowires are promising candidates for studying the rich theoretical predictions for one-dimensional transport [43], including charge/spin separation [55]. These results, along with the reconfigurable nature of this interface system, indicate further applications of this system as a platform for quantum information and simulation by using these ballistic nanowires as quantum buses for both electrons and electron pairs with modifiable correlations.

6.0 QUANTIZED BALLISTIC TRANSPORT OF ELECTRONS AND ELECTRON PAIRS IN AN ELECTRON WAVEGUIDE

The contents of this chapter represent a collaborative work submitted in Annadi, Lu, Lee, Lee, Cheng, Tylan-Tyler, Briggeman, Tomczyk, Huang, Pekker, Eom, Irvin and Levy, arXiv:1611.05127. The non-interacting waveguide model and tight-binding calculations in §§ 6.4.1 and 6.4.2, and KWANT calculations in § 6.4.6 were performed by A. Tylan-Tyler. Phase diagram calculations in § 6.4.4 were performed by D. Pekker.

6.1 INTRODUCTION

Electrons undergo profound changes in their behavior when constrained to move along a single axis. Theories of one-dimensional (1D) transport of interacting electron systems depend crucially on the sign of the electron-electron interaction. To date, 1D electron transport has only been explored within material systems with repulsive electron-electron interactions. SrTiO₃-based heterointerfaces support quasi-two-dimensional (2D) electron systems that are analogous to III-V semiconductor heterostructures, but also possess superconducting, magnetic, spintronic, ferroelectric and ferroelastic degrees of freedom. Despite these rich properties, the relatively low mobilities of 2D complex-oxide interfaces appear to preclude ballistic transport in 1D. Here we show that nearly ideal 1D electron waveguides exhibiting quantized ballistic transport of electrons and (non-superconducting) electron pairs can be formed at the interface between the two band insulators LaAlO₃ and SrTiO₃. These electron waveguides are created using a well-established conductive atomic-force microscope (c-AFM)

lithography technique that enables nanoscale control of the metal-insulator transition at the LaAlO₃/SrTiO₃ interface. Quantized ballistic transport within conducting nanowires at low temperature ranges from truly single-mode (1D) to three-dimensional (3D), depending on the applied magnetic field and gate voltage, revealing a manifold of electronic subbands that cleanly resolve both lateral and vertical transverse modes. These electron waveguides exhibit no valley degeneracies and can be tuned to the lowest spin-polarized conduction plateau ($G = e^2/h$), with no signatures of sub-structure or “0.7 anomalies” [146]. Quantization of the lowest e^2/h plateau indicates a ballistic mean-free path $l_{MF} \sim 20 \mu\text{m}$, with comparable values for ballistic electron pair transport. One feature that distinguishes this system from previously explored 1D channels is the existence of strong attractive electron-electron interactions which lead to electron pairing and superconductivity. We report quantized ballistic transport of electron pairs in magnetic fields as high as $B = 11 \text{ T}$. The pair transport is essentially dissipationless; however, it is not superconducting. Transport of re-entrant electron pairs is also observed at crossings between states with different transverse modes; a phase diagram for this re-entrant paired phase is calculated theoretically using a Hartree-Bogoliubov Hamiltonian. These results yield new insights into the electronic structure of the LaAlO₃/SrTiO₃ system and offer a new platform for the study of strongly interacting 1D electronic systems.

6.2 DEVICE GEOMETRY AND FABRICATION

The geometry used to investigate electron waveguide transport (Fig. 41) consists of a nanowire channel of total length L_C , surrounded by two narrow, highly transparent barriers (width $L_B \sim 5 - 20 \text{ nm}$) separated by a distance $L_S \sim 10 - 1000 \text{ nm}$. The chemical potential μ of the nanowire segment can be tuned by a side-gate voltage V_{sg} , which is positioned about 800 nm away from the nanowire. The wires are written at a tip voltage $V_{tip} = 15 \text{ V}$, except for the waveguide, which is created by a two-step voltage sequence. First, we move the AFM tip with $V_{tip} = 8 \text{ V}$ across the LaAlO₃ surface to create the main channel. Next, we repeat the same tip path with a small base voltage ($V_{tip} = 1 \text{ V}$) and apply two

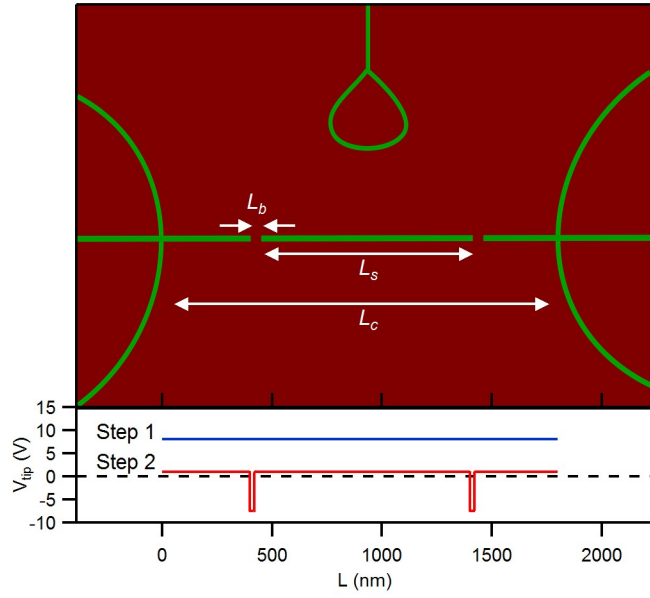


Figure 41: Waveguide writing schematic. To create the waveguide, a c-AFM tip first writes the channel using the voltage profile labeled “Step 1”, then re-writes the channel with the voltage profile labeled “Step 2” to create two weak spots in the channel.

negative voltage pulses ($V_{tip} = -7.5$ V) to create two transparent barriers, which act to slightly decouple the waveguide from the source and drain leads. This allows the chemical potential of the waveguide to be tuned efficiently with the side gate voltage V_{sg} . The barrier height is determined by the amplitude and duration of the negative pulses. Four-terminal transport measurements are carried out at or close to the base temperature of a dilution refrigerator ($T = 50$ mK) and subject to out-of-plane magnetic fields B .

Transport through a coherent quantum conductor can be described by Landauer's formula, $G = (e^2/h) \sum_i T_i(\mu)$, where each energy subband available at chemical potential μ contributes one quantum of conductance e^2/h with transmission probability $T_i(\mu)$. The transmission probability is given by $T_i(\mu) = \bar{T} F_T(\mu - E_i)$ where \bar{T} encompasses any tunneling resonances, cavity interference effects, or backscattering processes, $F_T(E)$ is a thermal broadening from the Fermi distribution function of the leads at a finite temperature, and E_i represents the energy minimum of the i th electron subband [147]. Within this framework, the conductance of a channel with all $T_i = 1$ increases in steps of e^2/h every time the chemical potential crosses a subband energy minimum. That is, transport through the channel is ballistic and dissipationless; however, the measured resistance is given by $R = h/(Ne^2)$, where N is the number of occupied subbands. The apparent contradiction between dissipationless transport within the waveguide and finite resistance was understood by Landauer, and put on a rigorous footing by Maslov and Stone, who developed a Luttinger liquid model of energy dissipation within the leads [148]. However, in experiments, even the cleanest systems do not have infinite scattering lengths; each subband can backscatter electrons, leading to a suppression which can be modeled as $\bar{T} = \exp(-L/L_i)$ [149], where L is the channel length and L_i is the mode-dependent scattering length. When $L_i \sim L$, the system is in the ballistic or quasi-ballistic regime, and when $L_i \gg L$, the system enters a quantized ballistic regime.

The expected properties of an ideal few-mode (i.e., few-subband) electron waveguide are illustrated in Fig. 42(b-g). The conductance of the waveguide depends on the number of accessible quantum channels (shown in Fig. 42(d-e) as energy-shifted parabolic bands). Fig. 42(b) and Fig. 42(d) depict a state in which a single spin-resolved subband is occupied. As the chemical potential μ is increased, more subbands in the waveguide become occupied.

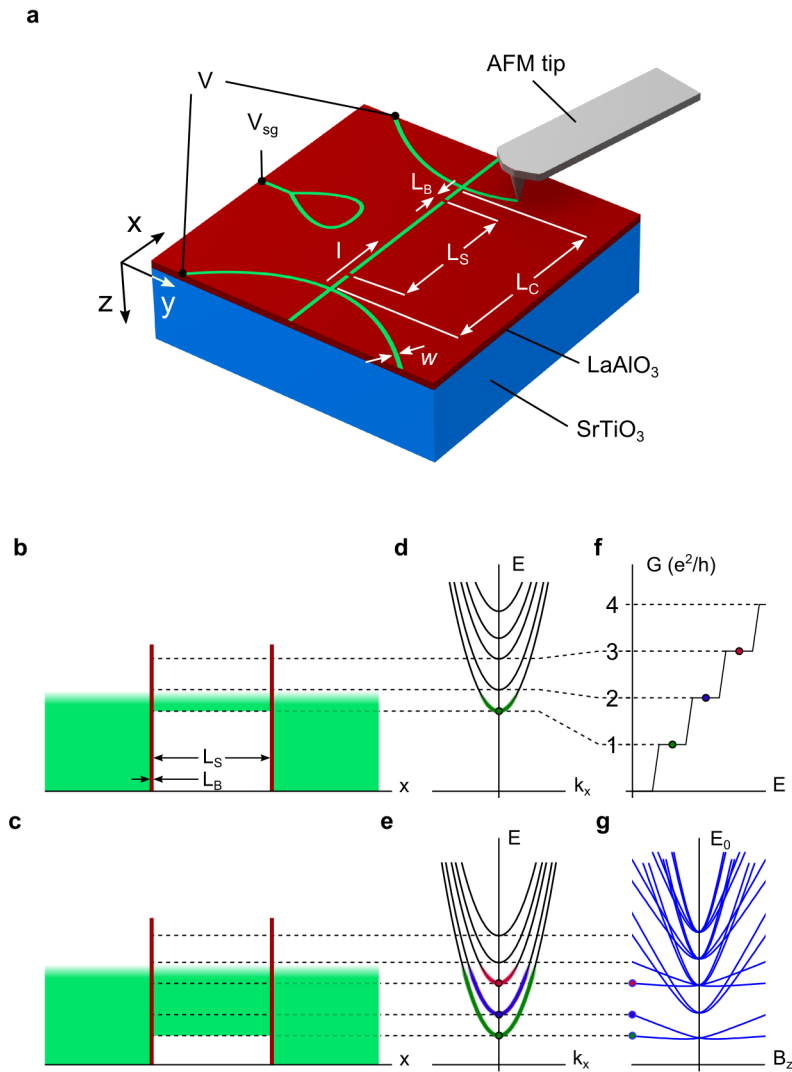


Figure 42: Expected transport characteristics of electron waveguides. **a**, Schematic of LaAlO₃/SrTiO₃ electron waveguide. **b**, **c**, Energy diagrams of the waveguide for two different values of chemical potential, which is controlled by V_{sg} . For (b), a single subband is occupied, while for (c) three subbands are occupied. **d**, **e**, depict the energy subbands corresponding to (b) and (c). Thick colored bands indicate occupied states. **f**, Zero-bias conductance quantization as a function of chemical potential. **g**, Waveguide subband structure (with both lateral and vertical confinement) as a function of magnetic field and chemical potential.

Fig. 42(c) and Fig. 42(e) depict a state in which $N = 3$ subbands contribute to transport. Each spin-resolved subband contributes e^2/h to the total conductance (Fig. 42(f)). The energy at which μ crosses a new subband (at $k_x = 0$) can generally shift in an applied magnetic field due to Zeeman and orbital effects. When lateral and vertical confinement energies are comparable, a more complex subband structure can emerge, as illustrated in Fig. 42(g).

6.3 EXPERIMENTS AND RESULTS

The experimentally-measured conductance dI/dV of LaAlO₃/SrTiO₃ waveguides is shown in Fig. 43(a-d). Here we focus on two distinct devices: device A ($L_C = 500$ nm, $L_S = 50$ nm, $L_B = 20$ nm) and device B ($L_C = 1.8$ μ m, $L_S = 1$ μ m, $L_B = 20$ nm). Fig. 43(a,c) shows the zero-bias conductance $G = dI/dV$ as a function of side-gate voltage V_{sg} (or chemical potential μ) for a sequence of magnetic fields between $B = 0$ T and 9 T. (Analysis of the non-equilibrium conductance, described in § 6.3.1, enables the lever-arm ratio $\alpha \equiv \frac{d\mu}{dV_{sg}}$ and g-factor $g \equiv \mu_B^{-1} \frac{d\mu}{dB}$ (where μ_B is the Bohr magneton) for the two devices A (B), to be extracted: $\alpha_{A(B)} = 4.5(9.9)$ μ eV/mV and $g_{A(B)} = 0.6(0.6)$.) For Device A (Fig. 43(a)), clear conductance steps of $G = 2e^2/h$ are visible for magnetic fields above ~ 1 T. These steps split into e^2/h steps, up to $N = 6$, at fields above ~ 3 T. When only a single barrier is present, no conduction quantization is observed (see discussion in § 6.4.6 and Fig. 50(b)) because the tunneling barriers are extremely narrow, in contrast to traditional semiconductor heterostructures. This conclusion is also supported by transport simulations (§ 6.4.6).

We attribute the observed conduction plateaus to Landauer quantization [47], for which the total conductance depends on the number of available quantum channels (subbands). The subband structure of these LaAlO₃/SrTiO₃ electron waveguides is clearly revealed by examining the transconductance $dG/d\mu$ as a function of μ and external magnetic field B (Fig. 43(b,d)). The transconductance shows an intricate set of bands (bright areas) which mark the boundaries where new subbands become available (as illustrated in Fig. 42(g)). These bands are separated by dark areas ($dG/d\mu \rightarrow 0$) where the conductance is highly

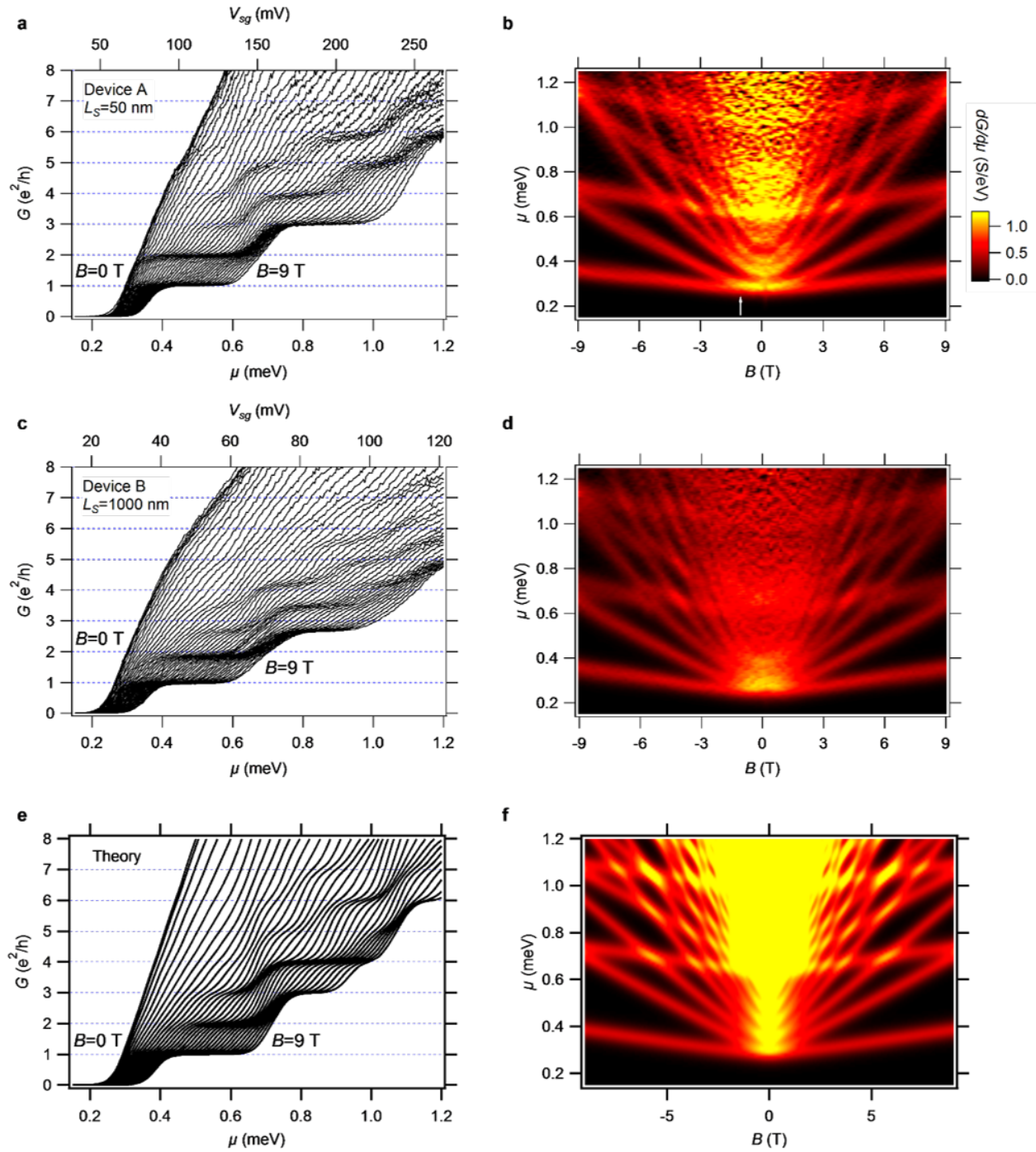


Figure 43: Transport for devices A and B at $T = 50$ mK, and comparison with theory. **a, c**, Zero-bias G of device A (a) and device B (b) as a function of μ for $B = 0 - 9$ T. **b, d**, $dG/d\mu$ shown as a function of μ and B for device A (b) and device B (d). The white arrow in (b) indicates the pairing field $B_P \approx 1$ T. **e, f**, Theoretical zero-bias G and $dG/d\mu$, modeling device A, for a non-interacting channel. Transitions have been broadened by a $65 \mu\text{eV}$ -wide Lorentzian.

quantized. At low magnetic fields (and low μ), the subbands scale roughly as B^2 and become more linear at larger magnetic fields. A pattern of subbands repeats at least twice, spaced by approximately $500 \mu\text{eV}$. The transconductance of the two devices A ($L_S = 50 \text{ nm}$) and B ($L_S = 1 \mu\text{m}$) are remarkably similar, despite the large difference in channel length and the fact that the coupling constant for the two devices differs by a factor of two.

While the lowest $N = 1$ state remains highly quantized for both devices (see Fig. 43), the plateaus do not fully reach the integer values for higher N for device B. The relationship between two length scales—the length scale of the device and the elastic scattering length (which is typically much shorter than the inelastic scattering length in quantum devices)—determines whether transport is ballistic. In electron waveguides at the $\text{LaAlO}_3/\text{SrTiO}_3$ interface, the elastic scattering length can be estimated assuming an exponential decay of the conductance $G = G_0 \exp(-L/L_0)$, where L_0 is the scattering length and L is the length of the device. The location of the minimum in the transconductance is used to find the value of the plateaus, as seen in Fig. 44. The first plateau conductances averaged over magnetic fields $5 \text{ T} < |B| < 9 \text{ T}$ for device A (B), with length $L = 0.05 \mu\text{m}$ ($L = 1 \mu\text{m}$), is $0.995e^2/h$ ($0.955e^2/h$). This gives a scattering length of $10 \mu\text{m} \pm 2.5 \mu\text{m}$ ($22 \mu\text{m} \pm 1.7 \mu\text{m}$), which is much longer than any of the waveguide devices; the electron waveguides are therefore effectively dissipationless over the relevant length scale of the device size. The conductance of these modes are not exactly e^2/h , however, in part because they are not topologically-protected edge modes, nor are they quantum Hall edge states. A similar analysis for the second conductance plateau gives scattering lengths of $3 \mu\text{m} \pm 0.5 \mu\text{m}$ and $12 \mu\text{m} \pm 0.7 \mu\text{m}$ for devices A and B, respectively.

6.3.1 Finite Bias Spectroscopy

Finite-bias spectroscopy is performed through current-voltage ($I - V$) measurements as a function of V_{sg} and B to further characterize the electron waveguides. As shown in Fig. 45(a), a large finite bias ($V_{sd} \geq V_{sd}^*$, where eV_{sd}^* is the energy between subsequent subbands) can unevenly populate subbands occupied by oppositely traveling electrons, which gives rise to the so-called half plateaus [150, 151]. The application of V_{sd} alters the chemical potentials of the

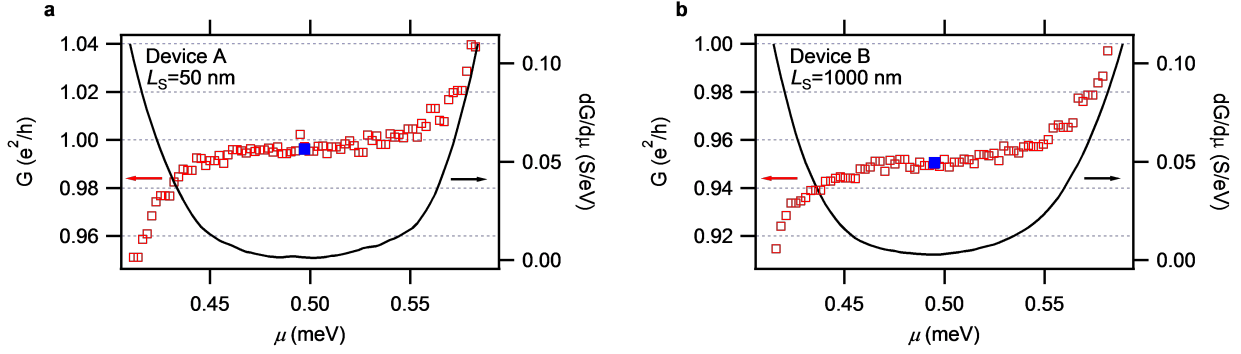


Figure 44: Quantization of the $1 e^2/h$ plateau. **a**, The first conductance plateau for device A, plotted with the transconductance on the right axis. At the middle of the transconductance dip, the conductance is $0.995e^2/h$, indicated by the blue square. **b**, The first conductance plateaus and transconductance for device B. For the $1 \mu\text{m}$ long waveguide, the conductance of the first plateau, $0.955e^2/h$, gives a scattering length of $22 \mu\text{m}$

drain lead (μ_d) and the source lead (μ_s) to $E_F \pm eV_{sd}/2$. The energy difference $\mu_d - \mu_s = eV_{sd}^*$ [as indicated by two red lines Fig. 45(a)] equals the subband spacing between the subbands $|0, 0, \downarrow\rangle$ and $|0, 0, \uparrow\rangle$. When $V_{sd} \leq V_{sd}^*$, electrons traveling in opposite directions occupy the same subband $|0, 0, \downarrow\rangle$ with conductance quantized to e^2/h . When V_{sd} reaches $|V_{sd}^*|$ ($-|V_{sd}^*|$), subband $|0, 0, \uparrow\rangle$ becomes available for electrons transmitting from drain (source) and gives rise to half plateau conductance ($1.5e^2/h$). Fig. 45(b) is the finite-bias transconductance plot of device A at $B = 7 \text{ T}$. The dark regions marked by the numbers are where conductance is quantized. The $0.5e^2/h$ and $1.5e^2/h$ plateaus can be clearly seen in the conductance plot at $V_{sd} = V_{sd}^* = 200 \mu\text{V}$ (Fig. 45(c)). The observation of these half plateaus is indicative of very clean transport through the electron waveguide devices, since back scattering is more likely to happen when unoccupied subbands become available at finite biases.

6.3.1.1 Lever Arm The finite-bias spectroscopy is used to extract the lever-arm α , which converts gate voltage to chemical potential. As illustrated in Fig. 45(b), the bright crossing ($V_{sd}^* = 200 \mu\text{V}$, $V_{sg} = 80 \text{ mV}$) marks the transition from one subband to another

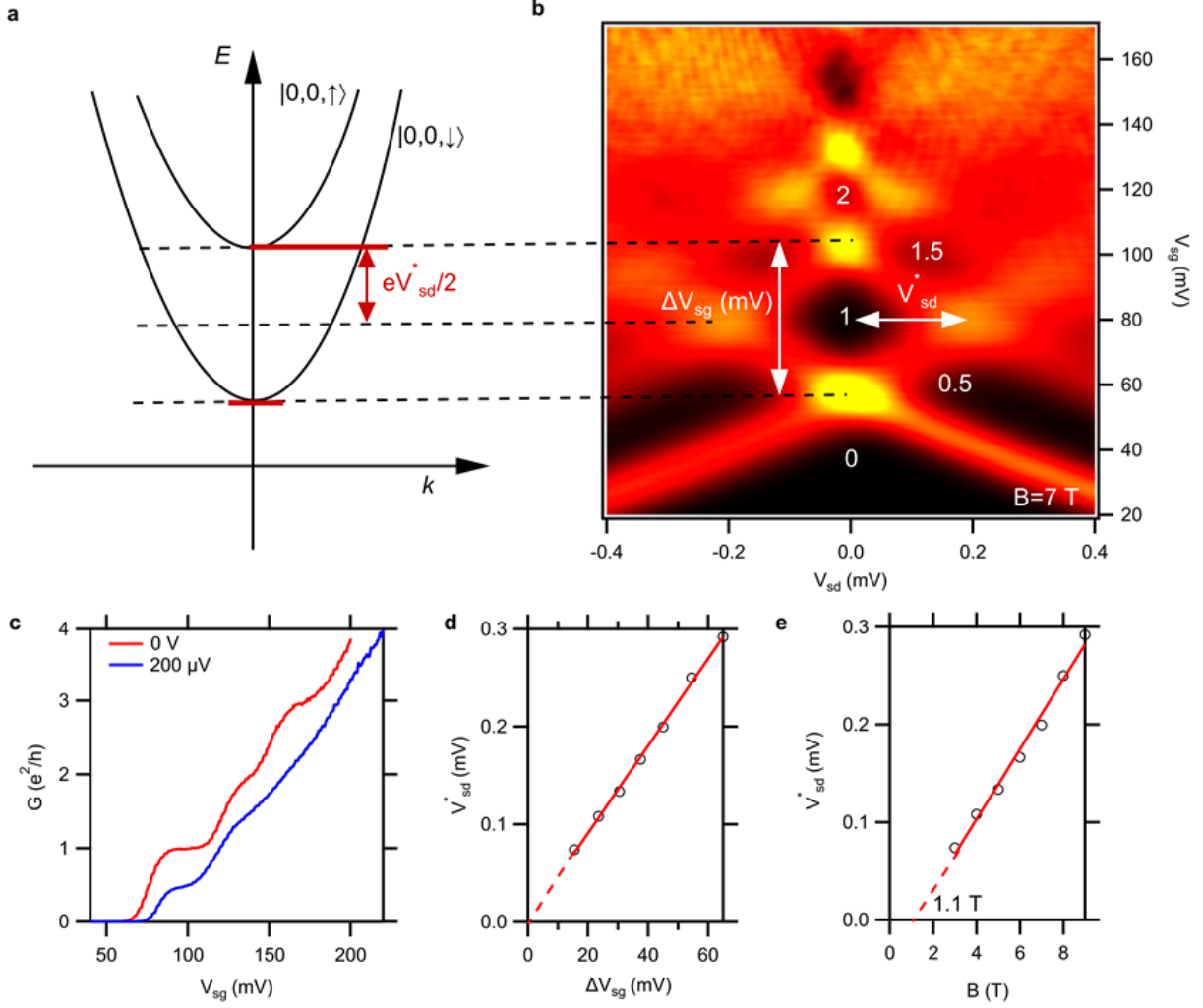


Figure 45: Finite bias analysis. **a**, Illustration of electron occupation of subbands $|0,0,\downarrow\rangle$ and $|0,0,\uparrow\rangle$ at a finite bias V_{sd} and $B = 7$ T. **(b)** Transconductance map of device A as a function of V_{sd} and V_{sg} at $B = 7$ T. Each bright band marks the transition between the conductance plateaus, labeled by quantization. **c**, G vs V_{sg} curves of zero bias ($V_{sd} = 0$ V) and finite bias ($V_{sd} = V_{sd}^* = 200 \mu\text{V}$) at $B = 7$ T. Half plateaus are clearly visible at finite bias (blue curve). **d**, V_{sd}^* dependent on ΔV_{sg} at magnetic fields from 3 T to 9 T in step of 1 T. The linear relationship and negligible intercept clearly establishes $eV_{sd}^* = \alpha\Delta V_{sg}$ with $\alpha = 4.5 \mu\text{eV}/\text{mV}$. **e**, Zeeman splitting between subbands $|0,0,\downarrow\rangle$ and $|0,0,\uparrow\rangle$ with the same field variation in (d). The g factor extracted from the slope is $g = 0.6$. Remarkably, subbands $|0,0,\downarrow\rangle$ and $|0,0,\uparrow\rangle$ only split above a critical magnetic field $B_p = 1.1$ T, which is marked by the intercept in the B axis.

due to the bias. At this condition, the energy gain induced by the bias V_{sd}^* should equal the subband spacing marked by $\alpha\Delta V_{sg}$ at zero bias, namely $eV_{sd} = \alpha\Delta V_{sg}$. Then $\alpha = eV_{sd}^*/\Delta V_{sg}$ can be precisely extracted by the slope of the $V_{sd}^* - \Delta V_{sg}$ plot at different magnetic fields (Fig. 45(d)). For device A, α_A is found to $4.5 \mu\text{eV}/\text{mV}$, and the fitted linear curve passes across zero as expected. Similarly, $\alpha_B = 9.9 \mu\text{eV}/\text{mV}$ can be extracted for device B, suggesting a stronger coupling of side gate to the waveguide, possibly due to the larger size.

6.3.1.2 g-Factor The Zeeman splitting between two spin-resolved subbands $|0, 0, \uparrow\rangle$ and $|0, 0, \downarrow\rangle$ can be used to extract the electron g factor. Fig. 45(d) shows the energy splitting (eV_{sd}^*) between these two subbands at various magnetic fields, where spin degeneracy is removed. Then the g factor is given by $g = (eV_{sd}^*)/(\mu_B B)$, where μ_B is the Bohr magneton. The extracted g factors for device A and B are (within measurement error) the same: $g_{A(B)} = 0.6$.

6.4 DISCUSSION

6.4.1 Non-Interacting Waveguide Model

Many of the features in the transconductance spectra shown in Fig. 43(a-d) are captured by a waveguide model of non-interacting electrons in a 3D waveguide. The waveguides confining potential can be regarded as translationally invariant along the propagation direction (x) and convex along the two transverse directions (lateral y and vertical z). Since the measured carrier density in conductive nanostructures created by c-AFM lithography is typically in the range of $0.5 - 1.0 \times 10^{13} \text{ cm}^{-2}$ [152], only the Ti d_{xy} band, being lower in energy than the d_{xz} and d_{yz} bands at the $\text{LaAlO}_3/\text{SrTiO}_3$ interface [32], is expected to be occupied at these carrier densities. Thus we assume that all of the conducting channels are derived from the lower d_{xy} band.

We use a potential $U_y = \frac{1}{2}m_y^*\omega_y^2 y^2$ to describe the lateral confinement, where $m_x^* = m_y^*$ is the effective mass in the $x - y$ plane and $\omega_y = \hbar/(m_y^* l_y^2)$ is the confinement frequency with l_y

being the characteristic width of the waveguide. In the vertical direction, the confinement at the interface is modeled by a half-parabolic potential, namely, $U_z = \frac{1}{2}m_z^*\omega_z^2 z^2$ for $z > 0$ and $U_z = +\infty$ for $z \leq 0$, where $\omega_z = \hbar/(m_z^*l_z^2)$ is the confinement frequency, m_z^* is the effective mass of the d_{xy} band in the z direction, and l_z is the penetration depth into the SrTiO₃. Within this single-particle picture, the full Hamiltonian can be written in the Landau gauge as

$$H = \frac{(p_x - eBy)^2}{2m_x^*} + \frac{p_y^2}{2m_y^*} + \frac{p_z^2}{2m_z^*} + \frac{m_y^*\omega_y^2}{2}y^2 + \frac{m_z^*\omega_z^2}{2}z^2 - g\frac{\mu_B}{2}B\sigma_z \quad (6.1)$$

where σ_z is the Pauli matrix. This Hamiltonian is readily solved to yield energy eigenstates $|n, m, s\rangle \otimes |k_x\rangle$ with corresponding energy

$$E_{m,n,s,k_x} = \hbar\Omega(n + 1/2) + \hbar\omega_z\left((2m + 1) + 1/2\right) - g\mu_B Bs + \frac{\hbar^2 k_x^2}{2m_x^*} \left(1 - \frac{\omega_c^2}{\Omega^2}\right) \quad (6.2)$$

where $\omega_c = eB/m_y^*$ is the cyclotron frequency, $\Omega = \sqrt{\omega_y^2 + \omega_c^2}$ is the effective frequency of the waveguide and magnetic field, n (m) enumerates the lateral (vertical) states, and $s = \pm 1/2$ is the spin quantum number. Distinct spin-resolved subbands [153] are associated with the discrete quantum numbers $|n, m, s\rangle$. Fig. 46(a) plots the eigenenergies for parameters that have been adjusted to resemble the experimentally measured transconductance (Fig. 43(d)). These values are also used to compute the expected conductance and transconductance versus chemical potential (Fig. 43(e,f)). The corresponding wavefunctions $\phi_{n,m,k_x,s}(y, z)$ (defined in Eq. 6.3) for selected states are illustrated in Fig. 46(c):

$$\begin{aligned} \phi_{n,m,k,s}(y, z) &\equiv \langle y, z, s; k | n, m, s \rangle \otimes |k_x\rangle \\ &= N_{n,m,k} e^{-\frac{m_y^*\Omega}{4\hbar} \left(y - \frac{\hbar\omega_c^2}{m_y^*\Omega} k\right)^2} H_n \left(\sqrt{\frac{m_y^2\Omega}{\hbar}} \left(y - \frac{\hbar\omega_x^2}{m_y^*\Omega} k\right) \right) e^{-\frac{m_z^*\omega_z}{4\hbar} z^2} H_{2m+1} \left(\sqrt{\frac{m_z^*\omega_z}{\hbar}} z \right) \end{aligned} \quad (6.3)$$

Here, $H_n(x)$ are the Hermite polynomials. The wavefunctions are displaced laterally by the magnetic field by an amount that depends quadratically on the kinetic energy (Fig. 46(b)). The set of parameters for device A (B), $l_y = 26$ (27) nm, $l_z = 8.1$ (7.9) nm, $m_x^* = m_y^* = 1.9$ (1.8) m_e , and $m_z^* = 6.5$ (6.4) m_e is obtained by maximizing agreement with

a tight-binding model that includes spin-orbit interactions (see below). At low magnetic fields, the energy scales quadratically with magnetic field, as it is dominated by the geometrical confinement contribution; at higher magnetic fields, the confinement from the cyclotron orbits dominates, producing a linear scaling. The crossover occurs near $\omega_B = \frac{eB}{m_y^*} \sim \omega_y$.

6.4.2 Tight-Binding Hamiltonian for Electron Waveguide

As the magnetic field couples to motion in the $x - y$ plane, the characteristic length scale and mass in the y -direction may be extracted directly from the transconductance data. To extract l_z and m_z^* from ω_z , it is necessary to use a more complete tight-binding model which includes the atomic spin-orbit coupling between the 3 Ti t_{2g} orbitals. The inclusion of this term then allows us to vary the mass m_z^* of the d_{xy} band (and the corresponding masses of the d_{yz} and d_{zx} bands) to see the reduction in the electron g factor (see later discussion in Sec. V). The resulting tight-binding Hamiltonian takes the form

$$\begin{aligned}
H = & \sum_{i,j,k} \left[\sum_{\alpha,s} \left(-t_x^\alpha e^{\frac{i\frac{e}{\hbar} B j d^2}{\phi_0}} a_{i,j,k}^{\alpha s \dagger} a_{i+1,j,k}^{\alpha s} - t_y^\alpha a_{i,j,k}^{\alpha s \dagger} a_{i,j+1,k}^{\alpha s} - t_z^\alpha a_{i,j,k}^{\alpha s \dagger} a_{i,j,k+1}^{\alpha s} \right) \right. \\
& \left. + \frac{\Delta_{aso}}{2} \sum_{s,s'} \left(-i_{ss'} a_{i,j,k}^{d_{xy} s' \dagger} a_{i,j,k}^{d_{yz} s'} + i_{ss'} a_{i,j,k}^{d_{xy} s' \dagger} a_{i,j,k}^{d_{xz} s'} + i_{ss'} a_{i,j,k}^{d_{yz} s' \dagger} a_{i,j,k}^{d_{xz} s'} \right), +h.c. \right] \\
& + \sum_{i,j,k,s,\alpha} \left[\left(\frac{m_y^{d_{xy}^*} \omega_y^2}{2} (jd)^2 + \frac{m_z^{d_{xy}^*} \omega_z^2}{2} (kd)^2 + 2t_x^\alpha + 2t_y^\alpha + 2t_z^\alpha \right) a_{i,j,k}^{\alpha s \dagger} a_{i,j,k}^{\alpha s} + \frac{g}{2} \mu_B B \sigma_z a_{i,j,k}^{\alpha s \dagger} a_{i,j,k}^{\alpha s} \right]
\end{aligned} \tag{6.4}$$

where t_i^α is the hopping in the i -direction for the band α , d is the lattice constant, ϕ_0 is the magnetic flux quantum, $\Delta_{aso} = 19.3$ meV is the atomic spin-orbit coupling [33], g is the bare-electron g factor, μ_B is the Bohr magneton, and $a_{i,j,k}^{\alpha s(\dagger)}$ destroys (creates) an electron at site i, j, k with spin s in band α . From this, the effective g factor can be extracted and compared to the experimental value to extract l_z and m_z^* from ω_z .

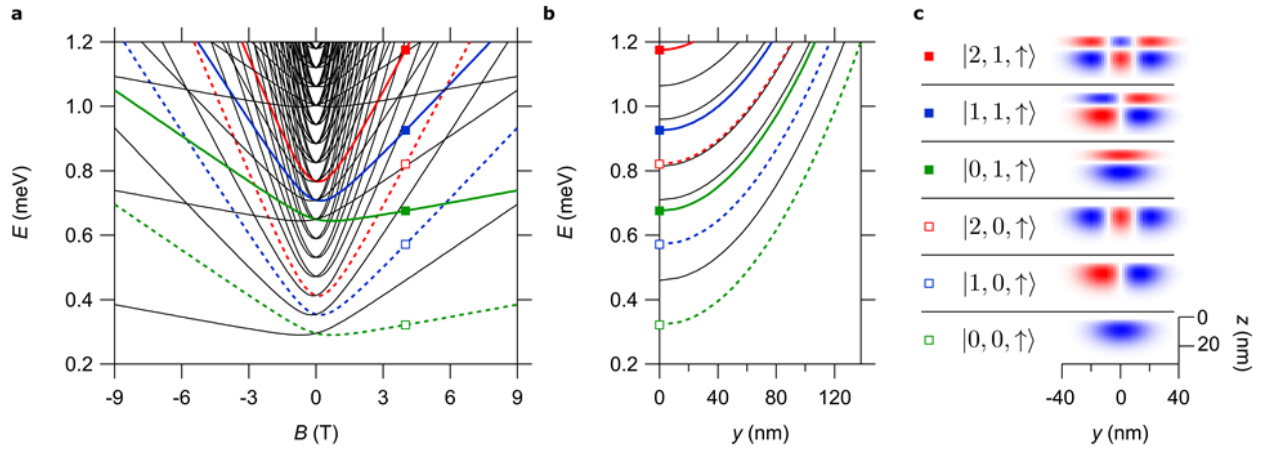


Figure 46: Non-interacting waveguide model. **a**, Eigenenergies for a quantum wire for the Hamiltonian described in Eq. 6.1 are plotted as a function of magnetic field B . Selected spin-up states are highlighted in color. **b**, Magnetically induced displacement of these states along the y direction as a function of eigenstate energy for $B = 4$ T. **c**, Six corresponding wavefunctions, labeled by $|n, m, s\rangle$, at $k_x = 0$ and $B = 4$ T. Red and blue colors indicate opposite sign of the wavefunction.

6.4.3 Electron Pairs at Low Magnetic Fields

While the single-particle model captures the overall subband structure, clear deviations in the experimental results are apparent. These electron waveguides exhibit electron pairing without superconductivity below a critical magnetic field B_p , similar in nature to reports for strongly confined quantum dot structures [8]. The extracted pairing field for the $|0, 0, s\rangle$ states is $B_p \approx 1$ T for device A and B (see Fig. 43). In other devices, electron pairing is much stronger. Device C, written on a different sample, exhibits highly quantized conduction but with a subband structure that differs qualitatively from devices A and B. There are three pairs of subbands that generate $2e^2/h$ steps (Fig. 47(a)). These pairs unbind at a critical field $B_p \approx 11$ T (Fig. 47(c), dashed lines). Superimposed over these pairs is a separate subband (with higher curvature) that contributes e^2/h to the conductance (Fig. 47(b)). At $B \approx 3$ T two paired subbands are superimposed with the unpaired subband, leading to a plateau near $5e^2/h$ (highlighted in green). Finally, re-entrant electron pairing is observed when electron subbands become degenerate; this phenomenon will be discussed in more detail in § 6.4.4.

6.4.4 Re-Entrant Pairing

Deviations from the single particle model arise from electron-electron interactions within the waveguide. The effects of these interactions become apparent in the transconductance data in the vicinity of subband crossing points (both at zero magnetic field and at finite field). Specifically, we observe extended regions of $2e^2/h$ conductance steps which we associate with a transition from a vacuum phase directly into a paired phase. That is, when a pair of subbands with opposite spin (e.g. $|1, 0, \uparrow\rangle$ and $|0, 1, \downarrow\rangle$) intersect at a finite magnetic field they are found to pair re-entrantly before separating again (Fig. 43 and Fig. 48). This observation is consistent with previously studies of one dimensional fermions with attractive interactions using both the Bethe Ansatz approach [154] (for the case of equal masses) and numerical approaches [155, 156] (for the case of unequal masses).

Here, we present a simple self-consistent Hartree-Bogoliubov model of crossing subbands that is both consistent with the more refined approaches and highlights the relevant physics

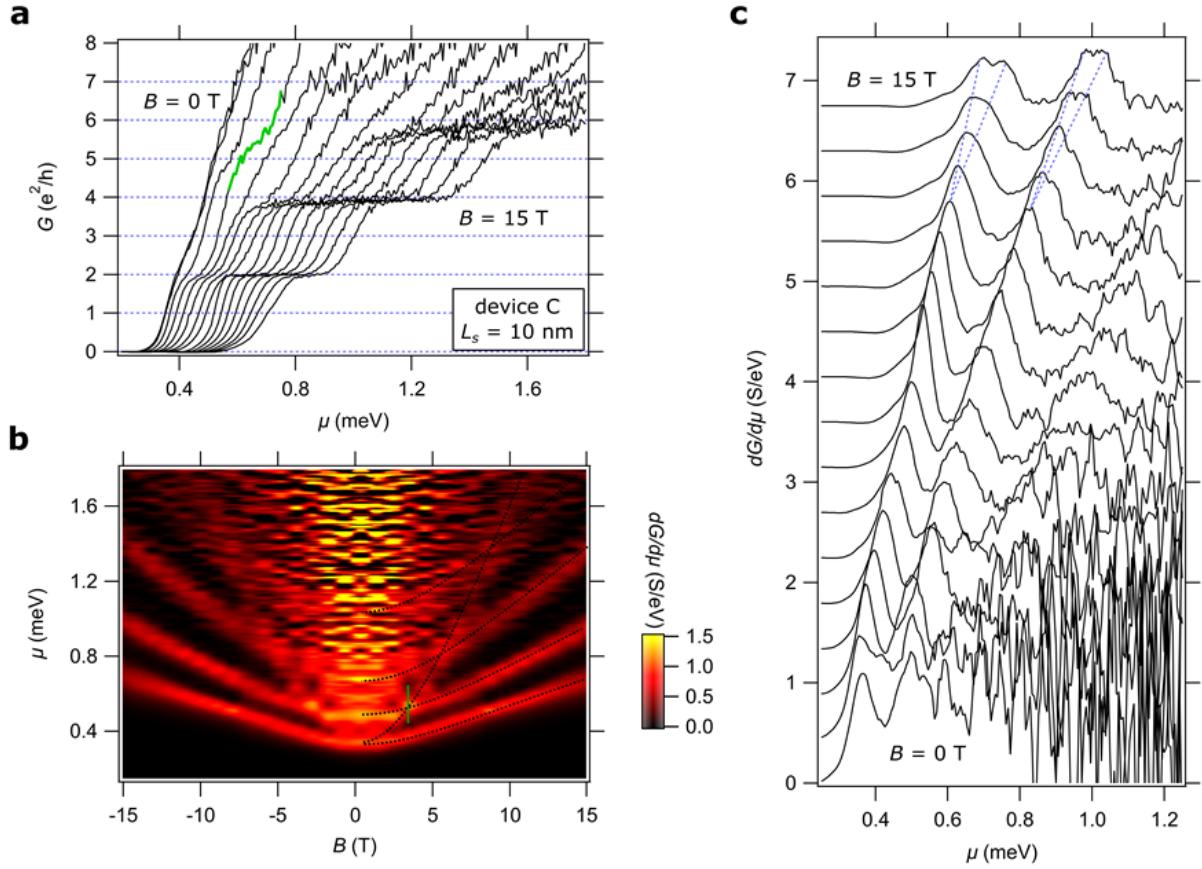


Figure 47: Strongly paired electron waveguides. **a**, Conductance of device C ($L_B = 5$ nm, $L_C = 350$ nm, $L_S = 10$ nm) versus chemical potential for magnetic fields ranging from 0 T to 15 T. This device shows strong electron pairing and associated $2e^2/h$ conductance steps. **b**, Transconductance plot shows three strongly paired states and a superimposed state with higher curvature associated with a conductance of e^2/h . The value of the latter state can be seen at $B = 3$ T in the conductance curve in panel a (highlighted in green) where it combines with the second strongly paired subband into a plateau near $5e^2/h$. **c**, Linecuts of transconductance plotted at magnetic fields from 0 T to 15 T in 1 T steps. The $2e^2/h$ peaks split above a pairing field $B_p \approx 11$ T, as indicated by the dashed lines.

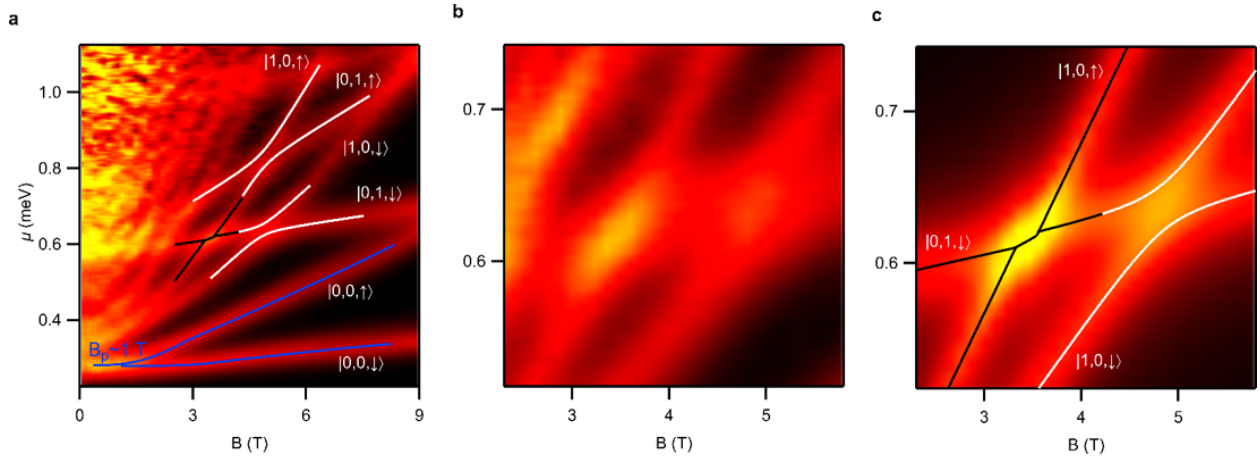


Figure 48: Electron-electron interaction in device A. **a**, Electron pairing (blue lines), avoided crossing (white lines), and re-entrant pairing (black lines) fittings of device A. **b**, Detailed view of re-entrant pairing and avoided crossing data in (a). **c**, Combined model fitting of data shown in (b). Here the black lines shows the fitting of re-entrant pairing between subband $|0, 1, \downarrow\rangle$ and $|1, 0, \uparrow\rangle$, with $\Delta_{rp} = 13 \mu\text{eV}$. The white lines are the fitting to the avoided crossing between subband $|0, 1, \downarrow\rangle$ and $|1, 0, \downarrow\rangle$, with $\Delta_{1,2} = 16 \mu\text{eV}$. (Full set of fitting parameters are listed in Tables 2 and 3).

without added complication. We start with the two-band, one-dimensional Hubbard model:

$$H = - \sum_{i,\alpha} t_\alpha (c_{\alpha,i}^\dagger c_{\alpha,i+1} + h.c.) + \sum_{i,\alpha} V_\alpha(V_{sg}, B) n_{\alpha,i} + U \sum_i n_{1,i} n_{2,i} \quad (6.5)$$

where i is the site index, α is the subband index, $V_\alpha(V_{sg}, B)$ describes the electrochemical potential as a function of the side gate voltage and magnetic field, and $U < 0$ models the electron-electron attraction. At the mean field level, this model is described by the single-particle Hamiltonian

$$\begin{pmatrix} \xi_{1,k} + \Sigma_1 & 0 & 0 & \Delta_{rp} \\ 0 & -(\xi_{1,k} + \Sigma_1) & \Delta_{rp} & 0 \\ 0 & \Delta_{rp} & \xi_{2,k} + \Sigma_2 & 0 \\ \Delta_{rp} & 0 & 0 & -(\xi_{2,k} + \Sigma_2) \end{pmatrix} \psi_{\beta,k} = E_{\beta,k} \psi_{\beta,k} \quad (6.6)$$

where we use the $\{c_{1,k}, c_{1,k}^\dagger, c_{2,-k}, c_{2,-k}^\dagger\}$ basis, $\{1,2\}$ are the subband labels, $\psi_{\beta,k}$ and $E_{\beta,k}$ are the quasi-particle wave functions and eigenenergies, $\xi_{\alpha,k}(\mu, B)$ corresponds to the non-interacting energy of an electron in the transverse subband α with momentum k along the wire, in magnetic field B , and chemical potential μ (that is tuned by V_{sg}). Σ_1, Σ_2 , and Δ_{rp} are the mean fields that must be found self-consistently. Σ_α represent the Hartree shifts due to the electrons in the opposite subband $\bar{\alpha}$:

$$\Sigma_\alpha = U_H \int \frac{dk}{2\pi} \langle c_{\bar{\alpha},k}^\dagger c_{\bar{\alpha},k} \rangle \quad (6.7)$$

and Δ_{rp} represents the re-entrant pairing field

$$\Delta_{rp} = U_B \int \frac{dk}{2\pi} \langle c_{2,-k} c_{1,k} \rangle \quad (6.8)$$

For concreteness, we have made the minimal assumption that the interactions are independent of momentum (i.e. local in real space) when writing the mean fields. We caution that a nonzero value of Δ should not be interpreted as a signature of superconductivity but only as a signature of pair formation as we are working in one dimension. Finally, when computing the matrix elements, we must keep in mind that the basis we are using is twice as big as the physical basis, and consequently, quasi-particle wave functions come in conjugate

pairs. However, only one member of the pair should be used (for example, the one that has the positive eigenvalue and thus corresponds to the quasi-particle creation operator).

We solve the Hartree-Bogoliubov model self-consistently to obtain a phase diagram near the crossing point of the $|0, 1, \downarrow\rangle$ and $|1, 0, \uparrow\rangle$ subbands (Fig. 49). The locations of the non-interacting subbands are plotted with dashed lines. By turning on the attractive inter-subband interaction, the Hartree shift tends to pull down the upper subband away from the crossing point; and pairing prevails closer to the crossing point which results in the merger of the two subbands into a single paired subband. Following the Maslov and Stone theorem, the conductance in the paired (spin-gapped) phase must be $2e^2/h$ [157]. We expect that these qualitative predictions are generic for systems with attractive inter-band interactions and not particularly sensitive to the assumptions that we have made: i.e. using the Hartree-Bogoliubov model with local interactions.

Provided the phase diagram in Fig. 49, we use a phenomenological model containing the phase boundaries to describe inter-band re-entrant pairing. The basic scenario is when two subbands $E_1 (= k_1 B + b_1)$ and $E_2 (= k_2 B + b_2)$ with opposite spins are tuned closely in energy, they combine as an electron pair, which breaks when the energies are tuned further away. These two subbands would simply cross (red dashed lines) if there were no electron-electron interaction. In the presence of the attractive pairing interaction, the higher energy subband undergoes an energy shift of $-2\delta_{1(2)}$ so that it can be written as $E'_{1(2)} = k_{1(2)}B + b_{1(2)} - 2\delta_{1(2)}$. And a middle section representing the paired phase emerges. The re-entrant pairing energy Δ_{rp} can then be extracted: $\Delta_{rp} = \delta_1 + \delta_2$. We are now able to use this model to extract these parameters from the experimental data using the fittings shown in Fig. 48(a) and Fig. 48(c). This process then gives a pairing field range $3.3 \text{ T} < B < 3.5 \text{ T}$ and a pairing energy $\Delta_{rp} = 13 \mu\text{eV}$ for subbands $|1, 0, \uparrow\rangle$ and $|0, 1, \downarrow\rangle$ in device A (see Table 2 for the full fitting parameters).

6.4.5 Avoided Crossings

Experimentally, we observe that when two subbands $|n_1, m_1, s\rangle$ and $|n_2, m_2, s\rangle$ share the same spin quantum number s and are nearly degenerate in energy ($E_{m_1, n_1, s} \approx E_{m_2, n_2, s}$), e.g.,

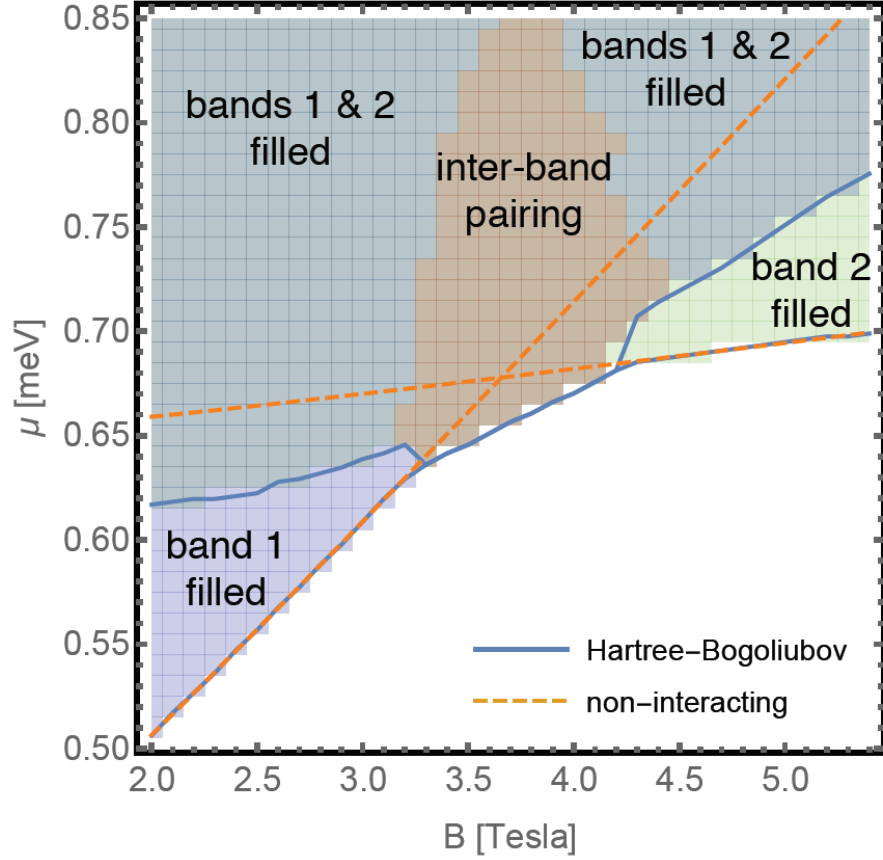


Figure 49: Phase diagram of the Hartree-Bogoliubov model in the $-B$ plane and near the crossing point of $|0, 1, \downarrow\rangle$ and $|1, 0, \uparrow\rangle$. In producing this diagram we used the band parameters for device A and set the attractive interaction constants to be $U_H = U_B = 100 \mu\text{eV}$.

Table 2: Re-entrant pairing fitting parameters for device A and B.

Device	Subbands	k ($\mu\text{eV}/\text{T}$)	b (μeV)	Δ_{rp} (μeV)
Device A	$ 1, 0, \uparrow\rangle$	133	168	13
	$ 0, 1, \downarrow\rangle$	15	566	
Device B	$ 1, 0, \uparrow\rangle$	130	120	10
	$ 0, 1, \downarrow\rangle$	14	585	

$|1, 0, \uparrow\rangle$ and $|0, 1, \uparrow\rangle$, they form an avoided crossing (Fig. 43(b,d) and Fig. 48). It is tempting to associate avoided crossings with repulsive electron-electron interactions, however the phase diagram of the repulsive version of the model (Eq. 6.5) does not admit this interpretation. However, an avoided crossing arises naturally if the transverse confinement potential is not separable [158, 159]. To model these avoided crossings, a simple two-level effective Hamiltonian of the form

$$H_{eff} = \begin{pmatrix} E_1 & \Delta_{1,2} \\ \Delta_{1,2} & E_2 \end{pmatrix} \quad (6.9)$$

is used, where $\Delta_{1,2}$ models the non-separability of the confinement potential by coupling the two states E_1 and E_2 . The chemical potentials at which the two transverse subbands become occupied follows

$$E_{AV\pm} = \frac{1}{2}(E_1 + E_2) \pm \frac{1}{2}\sqrt{(E_1 - E_2)^2 + 4\Delta_{1,2}^2} \quad (6.10)$$

To fit the experimental data, and extract the parameter $\Delta_{1,2}$, we approximate the single particle energy eigenvalue E_i with a linear magnetic field dependence $E_i = k_i B + b_i$ in the vicinity of the avoided crossing (see Fig. 48(a,c), as well as Table 3).

6.4.6 Single vs Double Barriers

In GaAs-based heterostructure devices, the number of transverse channels that are transmitted through a quantum point contact is typically controlled by a split top gate. In the case of electron waveguides at the LaAlO₃/SrTiO₃ interface, the channel width is determined by the c-AFM lithography writing parameters [71]; V_{sg} does not appreciably alter the characteristic width of the potential. Instead, V_{sg} tunes the chemical potential of the channel (with length L_s), with negligible effects on the grounded leads, as shown in Fig. 42(b-e).

To examine this scenario numerically, we look at the simplest case where the barriers do not disrupt the characteristic potentials of the quantum waveguide and only act as regions in which the chemical potential is continuously changed from that in the leads to that set by V_{sg} . For spinless particles, we may write a simple tight-binding Hamiltonian of the form

Table 3: Avoided crossing fitting parameters for device A and B.

Device	Subbands	k ($\mu\text{eV}/\text{T}$)	b (μeV)	Δ_{rp} (μeV)
Device A	$ 1, 0, \uparrow\rangle$	167	8	20
	$ 0, 1, \uparrow\rangle$	58	534	
	$ 1, 0, \downarrow\rangle$	91	195	16
	$ 0, 1, \downarrow\rangle$	15	566	
Device B	$ 1, 0, \uparrow\rangle$	168	-58	34
	$ 0, 1, \uparrow\rangle$	63	529	
	$ 1, 0, \downarrow\rangle$	95	139	40
	$ 0, 1, \downarrow\rangle$	14	585	

$$\begin{aligned}
 H = \sum_{i,j} \left[t_x^{dxy} \left(e^{\frac{i e B j d^2}{\hbar \phi_0}} a_{i,j}^\dagger a_{i+1,j} + a_{i,j}^\dagger a_{i,j+1} + h.c. \right) \right. \\
 \left. + \left(4t_x^{dxy} + \frac{m_y^* \omega_y^2}{2} (j d)^2 - V_B(i d, \mu) \right) a_{i,j}^\dagger a_{i,j} \right] \quad (6.11)
 \end{aligned}$$

where $V_B(x, \mu)$ is the chemical potential along the waveguide with μ being the chemical potential of the separated region. This function smoothly connects the chemical potential of the lead (chosen to be $4t_x^{dxy}$ so all subbands are occupied in the leads) to the chemical potential μ set by V_{sg} in the separate region over a characteristic length $L_b/2$ at the beginning and end of a region with characteristic length L_s .

Using the KWANT package [160] to calculate the transport properties of such a system, a single barrier ($L_S = 0$) device does not show quantization at any μ or magnetic field as seen in Fig. 50(a). This is what we expect from our model where a single barrier allows continuous tunneling between the leads which may be continuously tuned by changing the barrier height, as experiments show in Fig. 50(b). Finally, when two barriers are examined ($L_S > 0$), quantized conductance appears as the magnetic field is increased in Fig. 50(c), in agreement with the experimental data in Fig. 43.

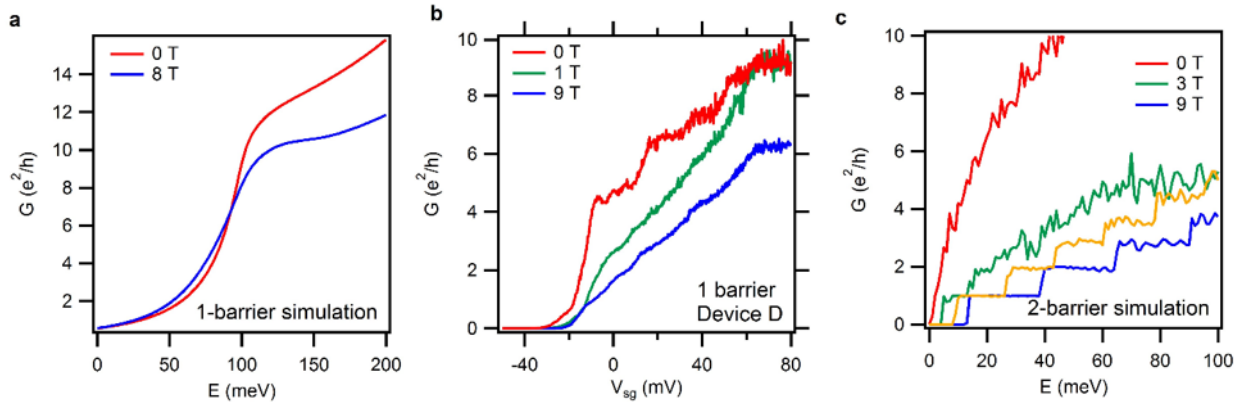


Figure 50: Single barrier vs double barriers. **a**, Single barrier simulation. Conductance quantization is smeared by tunneling directly across the barrier (from source to drain). **b**, Transport data of device D with only one barrier. No precise conductance quantization is observed at all magnetic fields, qualitatively in agreement with **a**. The high conductance at zero field is likely due to superconductivity. **c**, Double barrier simulation. Two barriers isolate the electron waveguide from the leads and allow the side gate to tune the chemical potential. Direct tunneling from source to drain is also suppressed. Clear conductance quantization is observed at high magnetic fields.

6.4.7 Comparison with Quantum Hall Effect

The observed conductance plateaus are not consistent with a quantum Hall state. The integer quantum Hall effect is defined by an insulating 2D bulk with chiral edge states that are responsible for the quantized conductance. By contrast, LaAlO₃/SrTiO₃-based electron waveguides lack the insulating bulk region that prevents backscattering. That is to say, the magnetic length ($l_B \sim 15$ nm for $B = 3$ T) and the confinement length ($l_y = 26$ (27) nm for device A (B)) are comparable and no well-defined bulk region is present.

The 3D structure of the electron waveguides is also inconsistent with quantum Hall physics. The cross-section of our waveguides is ellipsoidal with an aspect ratio of 0.5 (vertical/lateral, see Fig. 46(c)), which is well within the 3D regime. This regime is not expected to support stable quantum Hall bilayer states as multiple vertical subbands are occupied. For example, in Fig. 6.4.4(a), the $|0, 0, \uparrow\rangle$ and $|0, 1, \downarrow\rangle$ subbands would be unstable and therefore not quantized in a quantum Hall regime, according to Ref. [161]. The fact that quantized transport is observed provides further proof that this form of transport is not described by quantum Hall effects.

Finally, the lack of observable quantization at low fields is a consequence of the close spacing of lateral subband modes. The single-particle theory, illustrated in Fig. 43(e,f), shows that broadening of the subband transitions prevents the individual subbands from becoming resolvable at low magnetic fields; however, they become visible as soon as the magnetic dispersion can clearly separate them in energy. In other waveguides with larger subband spacing, conductance quantization is observable at small magnetic fields (Fig. 51).

6.5 CONCLUSION

The observation of quantized conduction in the paired regime ($G = 2e^2/h$ and $|B| < B_p$) signifies that these (non-single-particle) states propagate ballistically, forming an extended state in which electron pairs are bound together while the center-of-mass coordinate remains delocalized. Conduction quantization with steps of $2e^2/h$, rather than $(2e)^2/h$, is consistent

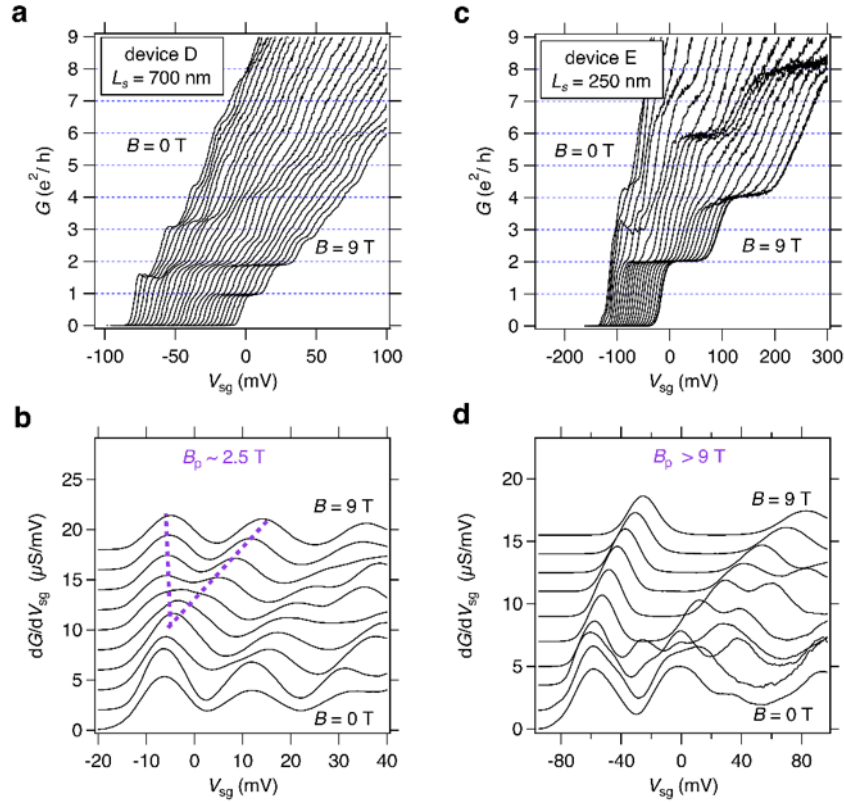


Figure 51: Critical magnetic field for splitting the lowest two spin subbands for additional devices D and E **a,c**, Zero-bias conductance G as a function of V_{sg} and B for device D ($L_B = 20$ nm, $L_C = 1500$ nm, $L_s = 700$ nm) and E ($L_B = 20$ nm, $L_C = 500$ nm, $L_s = 250$ nm) fabricated on different samples. Curves are offset for clarity **b,d**, Corresponding transconductance dG/dV_{sg} plots reveal B_p at which subbands $|0, 0, \downarrow\rangle$ and $|0, 0, \uparrow\rangle$ start to split. B_p values are high for device D (~ 2.5 T) and E (> 9 T) compared to device A and B in Fig. 43.

with the notion that dissipation takes place not within the channel itself but in the leads, and that electron pairs unbind before they dissipate energy [162, 163]. This interpretation is also consistent with the theorem of Maslov and Stone, who argued that the conductance of a Luttinger liquid is determined by the properties of the leads [148]. Specifically, the charge conductance of the channel remains $2e^2/h$ when a spin (i.e. pairing) gap is opened in the channel.

The range of pairing fields previously observed in tunneling experiments (§ 3) is consistent with the variation observed in these electron waveguides. For device A and B, $B_p \approx 1$ T is relatively low compared to $B_p \approx 11$ T in device C. Fig. 51 shows additional variation of B_p in two other devices. No specific dependence of B_p on device length can be inferred. Clearly, there are hidden variables that regulate the strength of electron pairing that have yet to be revealed experimentally.

The experiments described here show that electron waveguides provide remarkably detailed insight into the local electronic structure of these oxide interfaces. The level of reproducibility and reconfigurability illustrated by these experiments represents a significant advance in control over electronic transport in a solid-state environment. Correlated electron waveguides offer unique opportunities to investigate the rich physics that is predicted for 1D quantum systems [43]. For example, the number of quantum channels can be tuned to the lowest spin-polarized state (with $G = e^2/h$), forming an ideal spin-polarized Luttinger liquid. These 1D channels form a convenient and reproducible starting point for emulating a wider class of 1D quantum systems or for creating quantum channels that can be utilized in a quantum computing platform. While the lowest spin-polarized state is robust to disorder, the higher modes are very sensitive, which makes them potentially useful for nanoscale sensing.

7.0 FUTURE DIRECTIONS AND CONCLUSIONS

7.1 FUTURE DIRECTIONS

7.1.1 Pascal-Liquid Phase in an Electron Waveguide

Electron-electron interactions can lead to new quasiparticle states with properties that are profoundly different from individual electrons. For example, when there is even a weak effective attraction between electrons, pairing and superconductivity can take place. Ballistic electron waveguides which support multi-mode transport are a useful probe of the strong attractive interactions at the $\text{LaAlO}_3/\text{SrTiO}_3$ interface, clearly revealing the magnetic field behavior of the single- and paired-electron states as demonstrated in Ch. 6 of this thesis. Ballistic electron waveguides are also starting to reveal new families of emergent quasiparticle states where electrons bunch together in groups of increasing number (Fig. 52(c)). These composite particles with charge ne , where $n = 1, 2, 3, 4, 5, \dots$, produce quantized conductance in steps (Fig. 52(a)) that mirror the third row of Pascal's triangle- 1, 3, 6, 10... e^2h (Fig. 52(b)). The stability of this Pascal liquid phase is governed by strong electron-electron interactions that not only favor these multi-electron phases, but also appear to alter the overall band structure of the waveguide to achieve these low-energy states. The ubiquity of this phase, occurring in a dozen devices so far, also offers new insight into the variety of correlated electronic states that can exist within SrTiO_3 . The combination of control over two transverse degrees of freedom provided by the waveguides and the rich physics at the $\text{LaAlO}_3/\text{SrTiO}_3$ interface provide a unique platform for exploration of novel 1D transport and the discovery of new Pascal liquid phases.

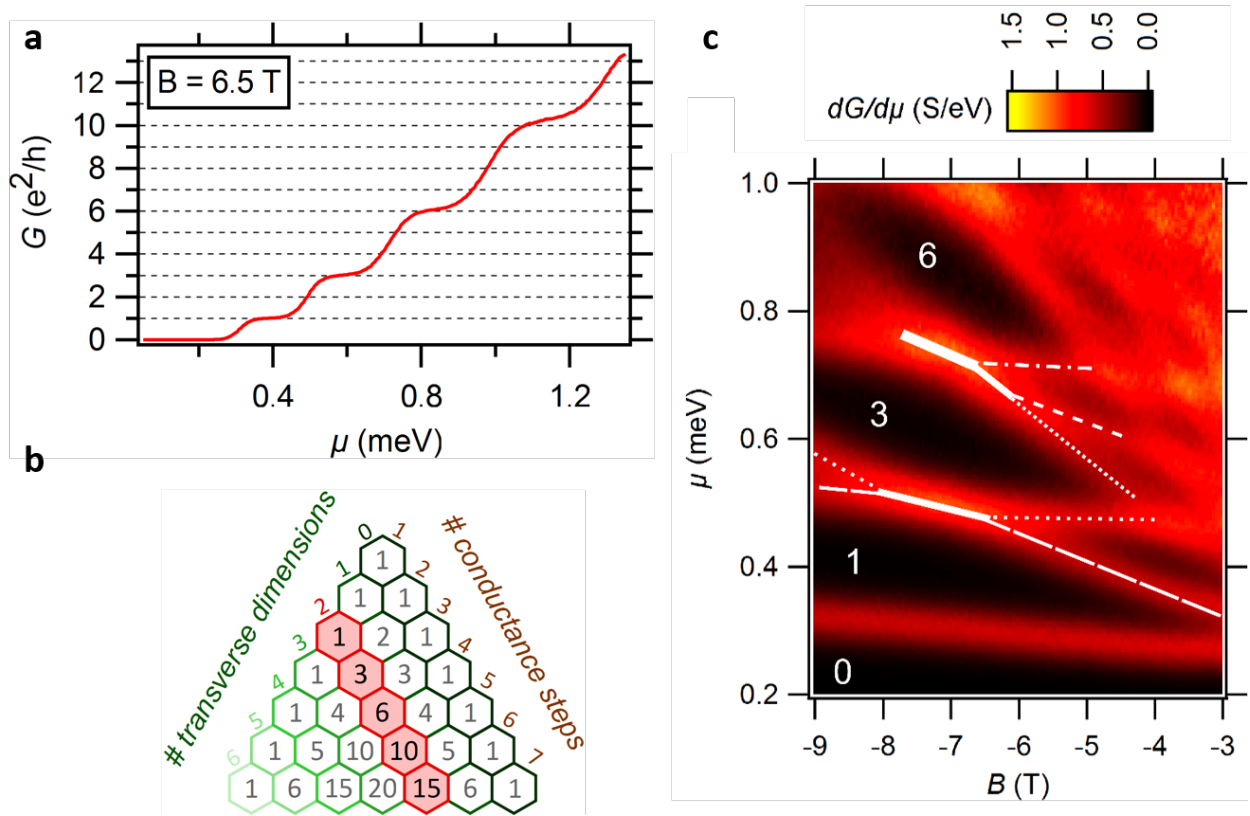


Figure 52: Pascal liquid phases in an electron waveguide. **a**, Conductance G as a function of chemical potential μ at $B = 6.5$ T showing quantized plateaus at $1, 3, 6,$ and $10 e^2/h$. **b**, Pascal's triangle, highlighting the series observed in conduction plateaus in $\text{LaAlO}_3/\text{SrTiO}_3$ waveguides. **c**, Transconductance dG/dV_μ highlighting the bunching 2 and 3 electrons into a pair and trion phase.

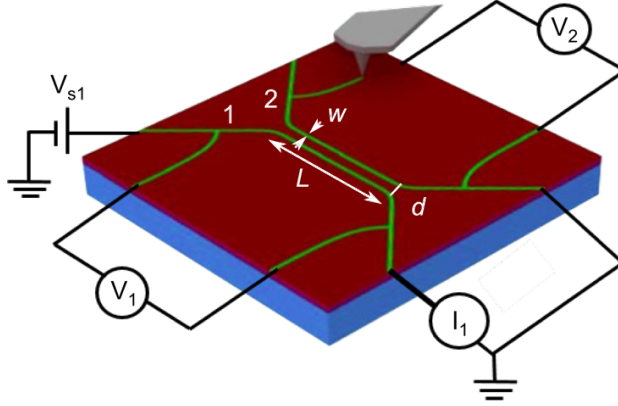


Figure 53: Frictional drag device setup.

7.1.2 Frictional Drag as a Probe of Electronic Interactions

Coulomb drag occurs between two electrically-isolated conductors, which are close enough that when current is driven through one conductor, the Coulomb interaction between electrons drives the motion of electrons in the other conductor, creating a drag voltage. In fact, any electron-electron interaction can be probed by such frictional drag measurements, not just conventional Coulombic interactions.

A device consisting of two closely-spaced parallel nanowires at the $\text{LaAlO}_3/\text{SrTiO}_3$ interface (Fig. 53) is expected to exhibit interesting behavior due to the strong attractive and gate-tunable interactions demonstrated and studied throughout this thesis. Of particular interest is the behavior as the drive and drag nanowires transition between the superconducting, paired, and single-particle regimes.

7.2 CONCLUSION

Electron-electron interactions at the $\text{LaAlO}_3/\text{SrTiO}_3$ interface have resulted in novel electronic states with surprising behaviors. Nanodevices have been key in discovering the nature of the electronic interactions and their consequences in transport. The amazing flexibility of

the c-AFM lithography technique promises a wide range of future experiments limited only by imagination: What impact might the frictional drag between two arms of an Aharanov-Bohm device have on the interference oscillations? What impact might the frictional drag between two arms of a SQUID device have on the critical current oscillations? Nanodevices will be a useful tool to probe the relationship between electron pairing and dimensionality, and understanding why c-AFM nanowires can support such clean transport compared to their 2D counterparts. Additionally, the ability to distinguish the behavior of individual electron states can be used to study and stabilize higher-order composite particles, to understand what role they might play in transport and superconductivity.

In conclusion, nanodevices at the $\text{LaAlO}_3/\text{SrTiO}_3$ interface will continue to be an important platform for exploring the mechanisms and consequences of electron-electron interactions and other emergent properties in this rich complex-oxide system.

BIBLIOGRAPHY

- [1] Schooley, J. F., Hosler, W. R. & Cohen, M. L. Superconductivity in semiconducting SrTiO₃. *Physical Review Letters* **12**, 474–475 (1964).
- [2] Caviglia, A. D. *et al.* Electric field control of the LaAlO₃/SrTiO₃ interface ground state. *Nature* **456**, 624–627 (2008).
- [3] Richter, C. *et al.* Interface superconductor with gap behaviour like a high-temperature superconductor. *Nature* **502**, 528–531 (2013).
- [4] Reyren, N. *et al.* Superconducting interfaces between insulating oxides. *Science* **317**, 1196–1199 (2007).
- [5] Ben Shalom, M., Sachs, M., Rakhmilevitch, D., Palevski, A. & Dagan, Y. Tuning spin-orbit coupling and superconductivity at the SrTiO₃/LaAlO₃ interface: a magnetotransport study. *Physical Review Letters* **104**, 126802 (2010).
- [6] Caviglia, A. D. *et al.* Tunable rashba spin-orbit interaction at oxide interfaces. *Physical Review Letters* **104**, 126803 (2010).
- [7] Brinkman, A. *et al.* Magnetic effects at the interface between non-magnetic oxides. *Nature Materials* **6**, 493–496 (2007).
- [8] Cheng, G. L. *et al.* Electron pairing without superconductivity. *Nature* **521**, 196–+ (2015).
- [9] Cheng, G. L. *et al.* Tunable electron-electron interactions in LaAlO₃/SrTiO₃ nanostructures. *Physical Review X* **6** (2016).
- [10] Tomczyk, M. *et al.* Micrometer-scale ballistic transport of electron pairs in LaAlO₃/SrTiO₃ nanowires. *Physical Review Letters* **117** (2016).
- [11] Annadi, A. *et al.* Dissipationless transport of electrons and cooper pairs in an electron waveguide. *submitted* arXiv:1611.05127 (2016).
- [12] Bardeen, J., Cooper, L. N. & Schrieffer, J. R. Theory of superconductivity. *Physical Review* **108**, 1175–1204 (1957).

- [13] Eagles, D. M. Possible pairing without superconductivity at low carrier concentrations in bulk and thin-film superconducting semiconductors. *Physical Review* **186**, 456 (1969).
- [14] Kalisky, B. *et al.* Locally enhanced conductivity due to the tetragonal domain structure in LaAlO₃/SrTiO₃ heterointerfaces. *Nature Materials* **12**, 1091–1095 (2013).
- [15] Honig, M. *et al.* Local electrostatic imaging of striped domain order in LaAlO₃/SrTiO₃. *Nature Materials* **12**, 1112–1118 (2013).
- [16] Noad, H. *et al.* Variation in superconducting transition temperature due to tetragonal domains in two-dimensionally doped SrTiO₃. *Physical Review B* **94** (2016).
- [17] Haeni, J. H. *et al.* Room-temperature ferroelectricity in strained SrTiO₃. *Nature* **430**, 758–761 (2004).
- [18] Sawaguchi, E., Kikuchi, A. & Kodera, Y. Dielectric constant of strontium titanate at low temperatures. *Journal of the Physical Society of Japan* **17**, 1666–& (1962).
- [19] Muller, K. A. & Burkard, H. SrTiO₃ - intrinsic quantum paraelectric below 4 k. *Physical Review B* **19**, 3593–3602 (1979).
- [20] Lin, X., Zhu, Z., Fauqu, B. & Behnia, K. Fermi surface of the most dilute superconductor. *Physical Review X* **3**, 021002 (2013).
- [21] Ueno, K. *et al.* Electric-field-induced superconductivity in an insulator. *Nature Materials* **7**, 855–858 (2008).
- [22] Binnig, G., Baratoff, A., Hoenig, H. E. & Bednorz, J. G. Two-band superconductivity in nb-doped SrTiO₃. *Physical Review Letters* **45**, 1352–1355 (1980).
- [23] Nozieres, P. & Schmitttrink, S. Bose condensation in an attractive fermion gas - from weak to strong coupling superconductivity. *Journal of Low Temperature Physics* **59**, 195–211 (1985).
- [24] Zwierlein, M. W., Abo-Shaer, J. R., Schirotzek, A., Schunck, C. H. & Ketterle, W. Vortices and superfluidity in a strongly interacting fermi gas. *Nature* **435**, 1047–1051 (2005).
- [25] Ohtomo, A. & Hwang, H. Y. A high-mobility electron gas at the LaAlO₃/SrTiO₃ heterointerface. *Nature* **427**, 423–426 (2004).
- [26] Thiel, S., Hammerl, G., Schmehl, A., Schneider, C. W. & Mannhart, J. Tunable quasi-two-dimensional electron gases in oxide heterostructures. *Science* **313**, 1942–1945 (2006).

- [27] Kim, Y., Lutchyn, R. M. & Nayak, C. Origin and transport signatures of spin-orbit interactions in one- and two-dimensional SrTiO₃-based heterostructures. *Physical Review B* **87**, 245121 (2013).
- [28] Joshua, A., Pecker, S., Ruhman, J., Altman, E. & Ilani, S. A universal critical density underlying the physics of electrons at the LaAlO₃/SrTiO₃ interface. *Nature Communications* **3**, 1129 (2012).
- [29] Bert, J. A. *et al.* Direct imaging of the coexistence of ferromagnetism and superconductivity at the LaAlO₃/SrTiO₃ interface. *Nature Physics* **7**, 767–771 (2011).
- [30] Herranz, G., Snchez, F., Dix, N., Scigaj, M. & Fontcuberta, J. High mobility conduction at (110) and (111) LaAlO₃/SrTiO₃ interfaces. *Scientific Reports* **2**, 758 (2012).
- [31] van Benthem, K., Elsasser, C. & French, R. H. Bulk electronic structure of SrTiO₃: Experiment and theory. *Journal of Applied Physics* **90**, 6156–6164 (2001).
- [32] Salluzzo, M. *et al.* Orbital reconstruction and the two-dimensional electron gas at the LaAlO₃/SrTiO₃ interface. *Physical Review Letters* **102**, 166804 (2009).
- [33] Zhong, Z. C., Toth, A. & Held, K. Theory of spin-orbit coupling at LaAlO₃/SrTiO₃ interfaces and SrTiO₃ surfaces. *Physical Review B* **87** (2013).
- [34] Bercioux, D. & Lucignano, P. Quantum transport in rashba spin-orbit materials: a review. *Reports on Progress in Physics* **78** (2015).
- [35] Seri, S., Schultz, M. & Klein, L. Interplay between sheet resistance increase and magnetotransport properties in LaAlO₃/SrTiO₃. *Physical Review B* **86** (2012).
- [36] Bi, F. *et al.* Room-temperature electronically-controlled ferromagnetism at the LaAlO₃/SrTiO₃ interface. *Nature Communications* **5**, 5019 (2014).
- [37] Bi, F. *et al.* LaAlO₃ thickness window for electronically controlled magnetism at LaAlO₃/SrTiO₃ heterointerfaces. *Applied Physics Letters* **107** (2015).
- [38] Lee, J. S. *et al.* Titanium dxy ferromagnetism at the LaAlO₃/SrTiO₃ interface. *Nature Materials* **12**, 703–706 (2013).
- [39] Salluzzo, M. *et al.* Origin of interface magnetism in bimno3/SrTiO₃ and LaAlO₃/SrTiO₃ heterostructures. *Physical Review Letters* **111** (2013).
- [40] Klitzing, K. v., Dorda, G. & Pepper, M. New method for high-accuracy determination of the fine-structure constant based on quantized hall resistance. *Physical Review Letters* **45**, 494–497 (1980).
- [41] Stormer, H. L., Tsui, D. C. & Gossard, A. C. The fractional quantum hall effect. *Reviews of Modern Physics* **71**, S298–S305 (1999).

- [42] Luttinger, J. M. An exactly soluble model of a many-fermion system. *Journal of Mathematical Physics* **4**, 1154–1162 (1963).
- [43] Giamarchi, T. Theoretical framework for quasi-one dimensional systems. *Chemical Reviews* **104**, 5037–5055 (2004).
- [44] Auslaender, O. M. *et al.* Spin-charge separation and localization in one dimension. *Science* **308**, 88–92 (2005).
- [45] Steinberg, H. *et al.* Charge fractionalization in quantum wires. *Nat Phys* **4**, 116–119 (2008).
- [46] Lee, P. A. & Stone, A. D. Universal conductance fluctuations in metals. *Phys Rev Lett* **55**, 1622–1625 (1985).
- [47] Landauer, R. Spatial variation of currents and fields due to localized scatterers in metallic conduction. *Ibm Journal of Research and Development* **1**, 223–231 (1957).
- [48] van Wees, B. J. *et al.* Quantized conductance of point contacts in a two-dimensional electron gas. *Physical Review Letters* **60**, 848–850 (1988).
- [49] Wharam, D. A. *et al.* One-dimensional transport and the quantisation of the ballistic resistance. *Journal of Physics C: Solid State Physics* **21**, L209 (1988).
- [50] Yacoby, A. *et al.* Nonuniversal conductance quantization in quantum wires. *Physical Review Letters* **77**, 4612–4615 (1996).
- [51] Frank, S., Poncharal, P., Wang, Z. L. & Heer, W. A. d. Carbon nanotube quantum resistors. *Science* **280**, 1744–1746 (1998).
- [52] Lin, Y.-M., Perebeinos, V., Chen, Z. & Avouris, P. Electrical observation of subband formation in graphene nanoribbons. *Physical Review B* **78**, 161409 (2008).
- [53] van Weperen, I., Plissard, S. R., Bakkers, E. P. A. M., Frolov, S. M. & Kouwenhoven, L. P. Quantized conductance in an insb nanowire. *Nano Letters* **13**, 387–391 (2013).
- [54] Timp, G. *et al.* Quantum transport in an electron-wave guide. *Physical Review Letters* **59**, 732–735 (1987).
- [55] Haldane, F. D. M. Luttinger liquid theory of one-dimensional quantum fluids .1. properties of the luttinger model and their extension to the general 1d interacting spinless fermi gas. *Journal of Physics C-Solid State Physics* **14**, 2585–2609 (1981).
- [56] Kane, C. L. & Fisher, M. P. A. Transport in a one-channel luttinger liquid. *Physical Review Letters* **68**, 1220–1223 (1992).
- [57] Giamarchi, T. & Schulz, H. J. Anderson localization and interactions in one-dimensional metals. *Physical Review B* **37**, 325–340 (1988).

- [58] Irvin, P. *et al.* Anomalous high mobility in LaAlO₃/SrTiO₃ nanowires. *Nano Letters* **13**, 364–368 (2013).
- [59] Cheng, G. *et al.* Anomalous transport in sketched nanostructures at the LaAlO₃/SrTiO₃ interface. *Physical Review X* **3**, 011021 (2013).
- [60] Ron, A. & Dagan, Y. One-dimensional quantum wire formed at the boundary between two insulating LaAlO₃/SrTiO₃ interfaces. *Physical Review Letters* **112**, 136801 (2014).
- [61] Park, J. W. *et al.* Creation of a two-dimensional electron gas at an oxide interface on silicon. *Nature Communications* **1**, 94 (2010).
- [62] Bark, C. W. *et al.* Tailoring a two-dimensional electron gas at the LaAlO₃/SrTiO₃ (001) interface by epitaxial strain. *Proceedings of the National Academy of Sciences of the United States of America* **108**, 4720–4724 (2011).
- [63] Bark, C. W. *et al.* Switchable induced polarization in LaAlO₃/SrTiO₃ heterostructures. *Nano Letters* **12**, 1765–1771 (2012).
- [64] Cen, C., Thiel, S., Mannhart, J. & Levy, J. Oxide nanoelectronics on demand. *Science* **323**, 1026–1030 (2009).
- [65] Irvin, P. *et al.* Rewritable nanoscale oxide photodetector. *Nature Photonics* **4**, 849–852 (2010).
- [66] Ma, Y. *et al.* Broadband terahertz generation and detection at 10 nm scale. *Nano Letters* **13**, 2884–2888 (2013).
- [67] Cheng, G. L. *et al.* Sketched oxide single-electron transistor. *Nature Nanotechnology* **6**, 343–347 (2011).
- [68] Binnig, G. & Rohrer, H. Scanning tunneling microscopy. *Helvetica Physica Acta* **55**, 726–735 (1982).
- [69] Giessibl, F. J. Advances in atomic force microscopy. *Reviews of Modern Physics* **75**, 949–983 (2003).
- [70] Binnig, G., Quate, C. F. & Gerber, C. Atomic force microscope. *Physical Review Letters* **56**, 930–933 (1986).
- [71] Cen, C. *et al.* Nanoscale control of an interfacial metal-insulator transition at room temperature. *Nature Materials* **7**, 298–302 (2008).
- [72] Brown, K. A. *et al.* Giant conductivity switching of LaAlO₃/SrTiO₃ heterointerfaces governed by surface protonation. *Nat Commun* **7** (2016).
- [73] Bi, F. *et al.* "water-cycle" mechanism for writing and erasing nanostructures at the LaAlO₃/SrTiO₃ interface. *Applied Physics Letters* **97**, 173110 (2010).

- [74] Dingle, R., Stormer, H. L., Gossard, A. C. & Wiegmann, W. Electron mobilities in modulation-doped semiconductor heterojunction super-lattices. *Applied Physics Letters* **33**, 665–667 (1978).
- [75] vonDelft, J., Zaikin, A. D., Golubev, D. S. & Tichy, W. Parity-affected superconductivity in ultrasmall metallic grains. *Physical Review Letters* **77**, 3189–3192 (1996).
- [76] Tinkham, M., Ralph, D. C., Black, C. T. & Hergenrother, J. M. Discrete energy levels and superconductivity in nanometer-scale al particles. *Czechoslovak Journal of Physics* **46**, 3139–3145 (1996).
- [77] Veazey, J. P. *et al.* Oxide-based platform for reconfigurable superconducting nanoelectronics. *Nanotechnology* **24**, 8 (2013).
- [78] Ralph, D. C., Black, C. T. & Tinkham, M. Spectroscopic measurements of discrete electronic states in single metal particles. *Physical Review Letters* **74**, 3241–3244 (1995).
- [79] Beenakker, C. W. J. Theory of coulomb-blockade oscillations in the conductance of a quantum dot. *Physical Review B* **44**, 1646–1656 (1991).
- [80] Hanson, R., Kouwenhoven, L. P., Petta, J. R., Tarucha, S. & Vandersypen, L. M. K. Spins in few-electron quantum dots. *Reviews of Modern Physics* **79**, 1217–1265 (2007).
- [81] Anderson, P. W. Theory of dirty superconductors. *Journal of Physics and Chemistry of Solids* **11**, 26–30 (1959).
- [82] Santander-Syro, A. F. *et al.* Two-dimensional electron gas with universal subbands at the surface of SrTiO₃. *Nature* **469**, 189–193 (2011).
- [83] Averin, D. V. & Nazarov, Y. V. Single-electron charging of a superconducting island. *Physical Review Letters* **69**, 1993–1996 (1992).
- [84] Matveev, K. A. & Larkin, A. I. Parity effect in ground state energies of ultrasmall superconducting grains. *Physical Review Letters* **78**, 3749–3752 (1997).
- [85] Anderson, P. W. The resonating valence bond state in la₂cuo₄ and superconductivity. *Science* **235**, 1196–1198 (1987).
- [86] Schlottmann, P. Exact results for highly correlated electron systems in one dimension. *International Journal of Modern Physics B* **11**, 355–667 (1997).
- [87] Lin, H. Q. Dilute gas of electron pairs in the t-j model. *Physical Review B* **44**, 4674–4676 (1991).
- [88] Hellberg, C. S. & Manousakis, E. 2-dimensional t-j model at low electron density. *Physical Review B* **52**, 4639–4642 (1995).

- [89] Cullum, J. & Willoughby, R. A. Computing eigenvalues of very large symmetric-matrices - an implementation of a lanczos-algorithm with no reorthogonalization. *Journal of Computational Physics* **44**, 329–358 (1981).
- [90] Cullum, J. & Willoughby, R. A. A survey of lanczos procedures for very large real symmetric eigenvalue problems. *Journal of Computational and Applied Mathematics* **12-3**, 37–60 (1985).
- [91] Hellberg. *Low-Temperature Thermodynamics of Quantum Systems*, 43–52 (Springer-Verlag Berlin Heidelberg, 2000).
- [92] Hellberg, C. S. Theory of the reentrant charge-order transition in the manganites. *Journal of Applied Physics* **89**, 6627–6629 (2001).
- [93] Micnas, R., Ranninger, J. & Robaszkiewicz, S. Superconductivity in narrow-band systems with local nonretarded attractive interactions. *Reviews of Modern Physics* **62**, 113–171 (1990).
- [94] Anderson, P. W. Model for electronic structure of amorphous semiconductors. *Physical Review Letters* **34**, 953–955 (1975).
- [95] Ashoori, R. C. *et al.* Single-electron capacitance spectroscopy of discrete quantum levels. *Physical Review Letters* **68**, 3088–3091 (1992).
- [96] Alt, H. C. Experimental evidence for a negative-u center in gallium-arsenide related to oxygen. *Physical Review Letters* **65**, 3421–3424 (1990).
- [97] Matsushita, Y., Bluhm, H., Geballe, T. H. & Fisher, I. R. Evidence for charge kondo effect in superconducting tl-doped pbte. *Physical Review Letters* **94**, 157002 (2005).
- [98] Dzero, M. & Schmalian, J. Superconductivity in charge kondo systems. *Physical Review Letters* **94**, 157003 (2005).
- [99] Geballe, T. H. & Kivelson, S. A. Paired insulators and high temperature superconductors. *arXiv:1406.3759* (2014).
- [100] Stashans, A., Pinto, H. & Sanchez, P. Superconductivity and jahn-teller polarons in titanates. *Journal of Low Temperature Physics* **130**, 415–423 (2003).
- [101] Gervais, F., Servoin, J. L., Baratoff, A., Bednorz, J. G. & Binnig, G. Temperature dependence of plasmons in nb-doped SrTiO₃. *Physical Review B* **47**, 8187–8194 (1993).
- [102] van Mechelen, J. L. M. *et al.* Electron-phonon interaction and charge carrier mass enhancement in SrTiO₃. *Physical Review Letters* **100** (2008).
- [103] Kolodiazhnyi, T. & Wimbush, S. C. Spin-singlet small bipolarons in nb-doped batio3. *Physical Review Letters* **96** (2006).

- [104] Costi, T. A. Kondo effect in a magnetic field and the magnetoresistivity of kondo alloys. *Physical Review Letters* **85**, 1504–1507 (2000).
- [105] Goldhaber-Gordon, D. *et al.* Kondo effect in a single-electron transistor. *Nature* **391**, 156–159 (1998).
- [106] Hofheinz, M. *et al.* Individual charge traps in silicon nanowires - measurements of location, spin and occupation number by coulomb blockade spectroscopy. *European Physical Journal B* **54**, 299–307 (2006).
- [107] Jung, S. W., Fujisawa, T., Hirayama, Y. & Jeong, Y. H. Background charge fluctuation in a gaas quantum dot device. *Applied Physics Letters* **85**, 768–770 (2004).
- [108] Bolotin, K. I., Kuemmeth, F., Pasupathy, A. N. & Ralph, D. C. Metal-nanoparticle single-electron transistors fabricated using electromigration. *Applied Physics Letters* **84**, 3154–3156 (2004).
- [109] Kim, M., Kozuka, Y., Bell, C., Hikita, Y. & Hwang, H. Y. Intrinsic spin-orbit coupling in superconducting delta-doped SrTiO₃ heterostructures. *Physical Review B* **86** (2012).
- [110] Tsui, D. C., Stormer, H. L. & Gossard, A. C. Two-dimensional magnetotransport in the extreme quantum limit. *Physical Review Letters* **48**, 1559–1562 (1982).
- [111] Laughlin, R. B. Anomalous quantum hall-effect - an incompressible quantum fluid with fractionally charged excitations. *Physical Review Letters* **50**, 1395–1398 (1983).
- [112] Jain, J. K. Composite-fermion approach for the fractional quantum hall-effect. *Physical Review Letters* **63**, 199–202 (1989).
- [113] Matveev, K. A. Conductance of a quantum wire in the wigner-crystal regime. *Physical Review Letters* **92** (2004).
- [114] Pesin, D. & Balents, L. Mott physics and band topology in materials with strong spin-orbit interaction. *Nature Physics* **6**, 376–381 (2010).
- [115] Anderson, P. W. *et al.* The physics behind high-temperature superconducting cuprates: the 'plain vanilla' version of rvb. *Journal of Physics-Condensed Matter* **16**, R755–R769 (2004).
- [116] Monthoux, P., Pines, D. & Lonzarich, G. G. Superconductivity without phonons. *Nature* **450**, 1177–1183 (2007).
- [117] Jorgensen, H. I., Novotny, T., Grove-Rasmussen, K., Flensberg, K. & Lindelof, P. E. Critical current 0-pi transition in designed josephson quantum dot junctions. *Nano Letters* **7**, 2441–2445 (2007).
- [118] Eichler, A. *et al.* Tuning the josephson current in carbon nanotubes with the kondo effect. *Physical Review B* **79** (2009).

- [119] Diener, R. B., Sensarma, R. & Randeria, M. Quantum fluctuations in the superfluid state of the bcs-bec crossover. *Physical Review A* **77** (2008).
- [120] Beenakker, C. & Van Houten, H. Resonant josephson current through a quantum dot. <http://arxiv.org/abs/condmat/0111505> (2001).
- [121] Maniv, E. *et al.* Strong correlations elucidate the electronic structure and phase diagram of LaAlO₃/SrTiO₃ interface. *Nature Communications* **6** (2015).
- [122] Pallecchi, I. *et al.* Giant oscillating thermopower at oxide interfaces. *Nature Communications* **6** (2015).
- [123] Li, L., Richter, C., Mannhart, J. & Ashoori, R. C. Coexistence of magnetic order and two-dimensional superconductivity at LaAlO₃/SrTiO₃ interfaces. *Nature Physics* **7**, 762–766 (2011).
- [124] Lee, E. J. H. *et al.* Spin-resolved andreev levels and parity crossings in hybrid superconductor-semiconductor nanostructures. *Nature Nanotechnology* **9**, 79–84 (2014).
- [125] Choi, H. Y., Bang, Y. Y. & Campbell, D. K. Andreev reflections in the pseudogap state of cuprate superconductors. *Physical Review B* **61**, 9748–9751 (2000).
- [126] Rakhmievitch, D. *et al.* Phase coherent transport in SrTiO₃/LaAlO₃ interfaces. *Physical Review B* **82**, 235119 (2010).
- [127] Schneider, C. W., Thiel, S., Hammerl, G., Richter, C. & Mannhart, J. Microlithography of electron gases formed at interfaces in oxide heterostructures. *Applied Physics Letters* **89**, 122101 (2006).
- [128] Chang, J. W. *et al.* Quantum electrical transport in mesoscopic LaAlO₃/SrTiO₃ heterostructures. *Applied Physics Express* **6** (2013).
- [129] Caviglia, A. D. *et al.* Two-dimensional quantum oscillations of the conductance at LaAlO₃/SrTiO₃ interfaces. *Physical Review Letters* **105**, 236802 (2010).
- [130] Stornaiuolo, D. *et al.* In-plane electronic confinement in superconducting LaAlO₃/SrTiO₃ nanostructures. *Applied Physics Letters* **101**, 222601 (2012).
- [131] Banerjee, N., Huijben, M., Koster, G. & Rijnders, G. Direct patterning of functional interfaces in oxide heterostructures. *Applied Physics Letters* **100** (2012).
- [132] Gallagher, P., Lee, M., Williams, J. R. & Goldhaber-Gordon, D. Gate-tunable superconducting weak link and quantum point contact spectroscopy on a strontium titanate surface. *Nature Physics* **10**, 748–752 (2014).

- [133] Kretinin, A. V., Popovitz-Biro, R., Mahalu, D. & Shtrikman, H. Multimode fabry-perot conductance oscillations in suspended stacking-faults-free inas nanowires. *Nano Letters* **10**, 3439–3445 (2010).
- [134] Liang, W. J. *et al.* Fabry-perot interference in a nanotube electron waveguide. *Nature* **411**, 665–669 (2001).
- [135] Miao, F. *et al.* Phase-coherent transport in graphene quantum billiards. *Science* **317**, 1530–1533 (2007).
- [136] Simmons, J. A., Tsui, D. C. & Weimann, G. Quantum interference effects in high-mobility mesoscopic gaas/alxgal-xas heterostructures. *Surface Science* **196**, 81–88 (1988).
- [137] Veazey, J. P. *et al.* Nonlocal current-voltage characteristics of gated superconducting sketched oxide nanostructures. *Epl* **103** (2013).
- [138] Kirczenow, G. Resonant conduction in ballistic quantum channels. *Physical Review B* **39**, 10452–10455 (1989).
- [139] Jarillo-Herrero, P., van Dam, J. A. & Kouwenhoven, L. P. Quantum supercurrent transistors in carbon nanotubes. *Nature* **439**, 953–956 (2006).
- [140] Wang, Q. *et al.* Conductance oscillations induced by longitudinal resonant states in heteroepitaxially defined ga_{0.25}in_{0.75}as/inp electron waveguides. *Applied Physics Letters* **76**, 2274–2276 (2000).
- [141] Connor, J. N. L. On analytical description of resonance tunnelling reactions. *Molecular Physics* **15**, 37–46 (1968).
- [142] Buitelaar, M. R., Bachtold, A., Nussbaumer, T., Iqbal, M. & Schonberger, C. Multiwall carbon nanotubes as quantum dots. *Physical Review Letters* **88**, 156801 (2002).
- [143] Phillips, P. & Dalidovich, D. The elusive bose metal. *Science* **302**, 243–247 (2003).
- [144] Deissler, B. *et al.* Delocalization of a disordered bosonic system by repulsive interactions. *Nature Physics* **6**, 354–358 (2010).
- [145] Tsen, A. W. *et al.* Nature of the quantum metal in a two-dimensional crystalline superconductor. *Nature Physics* **12**, 208–+ (2016).
- [146] Micolich, A. P. & Zulicke, U. Tracking the energies of one-dimensional sub-band edges in quantum point contacts using dc conductance measurements. *Journal of Physics-Condensed Matter* **23** (2011).
- [147] Datta, S. Atom to transistor: A bottom-up viewpoint. *Abstracts of Papers of the American Chemical Society* **230**, U2776–U2777 (2005).

- [148] Maslov, D. L. & Stone, M. Landauer conductance of luttinger liquids with leads. *Physical Review B* **52**, R5539–R5542 (1995).
- [149] Nikolic, K. & Mackinnon, A. Conductance and conductance fluctuations of narrow disordered quantum wires. *Physical Review B* **50**, 11008–11017 (1994).
- [150] Glazman, L. I. & Khaetskii, A. V. Nonlinear quantum conductance of a lateral micro-constraint in a heterostructure. *Europhysics Letters* **9**, 263–267 (1989).
- [151] Patel, N. K. *et al.* Ballistic transport in one-dimension - additional quantization produced by an electric-field. *Journal of Physics-Condensed Matter* **2**, 7247–7254 (1990).
- [152] Bi, F. *et al.* Electro-mechanical response of top-gated LaAlO₃/SrTiO₃. *Journal of Applied Physics* **119** (2016).
- [153] Topinka, M. A. *et al.* Imaging coherent electron flow from a quantum point contact. *Science* **289**, 2323–2326 (2000).
- [154] Guan, X. W., Batchelor, M. T. & Lee, C. Fermi gases in one dimension: From bethe ansatz to experiments. *Reviews of Modern Physics* **85**, 1633–1691 (2013).
- [155] Wang, B., Chen, H. D. & Das Sarma, S. Quantum phase diagram of fermion mixtures with population imbalance in one-dimensional optical lattices. *Physical Review A* **79** (2009).
- [156] Orso, G., Burovski, E. & Jolicoeur, T. Luttinger liquid of trimers in fermi gases with unequal masses. *Physical Review Letters* **104** (2010).
- [157] Maslov, D. L. Transport through dirty luttinger liquids connected to reservoirs. *Physical Review B* **52**, R14368–R14371 (1995).
- [158] Salis, G. *et al.* Mode spectroscopy and level coupling in ballistic electron waveguides. *Physical Review B* **60**, 7756–7759 (1999).
- [159] Fischer, S. F., Apetrii, G., Kunze, U., Schuh, D. & Abstreiter, G. Magnetotransport spectroscopy of spatially coincident coupled electron waveguides. *Physical Review B* **71** (2005).
- [160] Groth, C. W., Wimmer, M., Akhmerov, A. R. & Waintal, X. Kwant: a software package for quantum transport. *New Journal of Physics* **16** (2014).
- [161] Sawada, A. *et al.* Phase transition in the nu=2 bilayer quantum hall state. *Physical Review Letters* **80**, 4534–4537 (1998).
- [162] Beenakker, C. W. J. & Vanhouten, H. Josephson current through a superconducting quantum point contact shorter than the coherence length. *Physical Review Letters* **66**, 3056–3059 (1991).

- [163] Kanasz-Nagy, M., Glazman, L., Esslinger, T. & Demler, E. A. Anomalous conductances in an ultracold quantum wire. *Physical Review Letters* **117** (2016).